	Study of AMV speed biases in the tropics Final Report	
Reference: AMV-TN-0008-TS_Ed1_Rev3	Date : 18/06/2020	Page : <i>i/118</i>

STUDY OF AMV SPEED BIASES IN THE TROPICS

FINAL REPORT

For: EUMETSAT
 Addressee: Régis Borde
 Reference: AMV-TN-0008-TS
 Date: 18/06/2020
 Edition: 1
 Revision: 3
 Page: *i/ 118*

THALES Services SAS

290 allée du Lac
 31670 Labège
 France

Tel.: +33-562 88 86 00


Fax: +33-562 88 76 00

Web: <http://www.thalesgroup.com>




Division Secure Communications and Information Systems (SIX), 2021

Copyright 2021 - In accordance with EUMETSAT Contract No. EUM/CO/18/4600002168/RBo - Order n°4500017165

	<p align="center">Study of AMV speed biases in the tropics</p> <p align="center">Final Report</p>	
Reference: AMV-TN-0008-TS_Ed1_Rev3	Date : 18/06/2020	Page : <i>ii/118</i>


Disclaimer and Acknowledgement

The presented work includes preliminary data (not fully calibrated/validated and not yet publicly released) of the Aeolus mission that is part of the European Space Agency (ESA) Earth Explorer Programme. This includes wind products from before the public data release in May 2020 and/or aerosol and cloud products, which have not yet been publicly released. The preliminary Aeolus wind products will be reprocessed during 2020 and 2021, which will include in particular a significant L2B product wind bias reduction and improved L2A radiometric calibration. Aerosol and cloud products will become publicly available by spring 2021. The processor development, improvement and product reprocessing preparation are performed by the Aeolus DISC (Data, Innovation and Science Cluster), which involves DLR, DoRIT, ECMWF, KNMI, CNRS, S&T, ABB and Serco, in close cooperation with the Aeolus PDGS (Payload Data Ground Segment). The analysis has been performed in the frame of the Aeolus Scientific Calibration & Validation Team (ACVT).


	Study of AMV speed biases in the tropics Final Report	
Reference: AMV-TN-0008-TS_Ed1_Rev3	Date : 18/06/2020	Page : <i>iii/118</i>

Evolution sheet


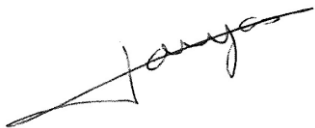
Issue	Date	Evolution	Reason for evolution
1.0	18/06/2020	Creation	
1.1	05/02/2020	<p>§1.2 Scientific achievements: Executive Summary now highlights the main findings of each task and sub-task</p> <p>§5.1 MISR stereo AMVs: Error in MISR geometric altitude to pressure conversion has been corrected</p> <p>§5.6.1 GDI from ECMWF: Error in GDI computation from ECMWF humidity and temperature fields has been corrected</p> <p>§6. Analysis of semivariograms: Analysis has been moved to Section 6.1 and is now limited to one case in Northern Africa. Plots of latitudinal wind speed profiles have been added to the analysis. Semivariograms of other cases have been removed as semivariograms are meant to help verifying if the location of jets is correct or not. This does not apply to the boiler-box region, as there are no jets prevailing.</p> <p>§7.2 Conversion from AVHRR radiances to brightness temperatures has been corrected</p> <p>§8.3 Recommendations: Recommendations for both Meteosat-10 and Metop AMV extraction schemes have been modified</p>	Modifications following EUMETSAT's comments and recommendations during the 2 nd mid-term review meeting on 5 November 2019.


	Study of AMV speed biases in the tropics Final Report	
Reference: AMV-TN-0008-TS_Ed1_Rev3	Date : 18/06/2020	Page : <i>iv/118</i>

Issue	Date	Evolution	Reason for evolution
1.2	30/04/2020	Addition of comparison study of AMVs to HLOS winds from ADM-Aeolus (Section 1.2.3, 7, 8.3)	
1.3	18/06/2020	Addition of Figure 7.10 and Figure 7.13 to Section 7.2.3	Modifications following EUMETSAT's comments and recommendations during the final meeting on 18 June 2020.

	Study of AMV speed biases in the tropics Final Report	
Reference: AMV-TN-0008-TS_Ed1_Rev3	Date : 18/06/2020	Page : v/118


Approval sheet

Function	Name	Date	Signature
Written by project team	Johannes STAUFER	18/06/2020	
Verified by Quality Manager	Chantal TOUJAS	18/06/2020	
For application by Project Manager	Laure CHAUMAT	18/06/2020	


	<p align="center">Study of AMV speed biases in the tropics</p> <p align="center">Final Report</p>	
Reference: AMV-TN-0008-TS_Ed1_Rev3	Date : 18/06/2020	Page : vi/118

Contents

1	EXECUTIVE SUMMARY	17
1.1	Objectives	17
1.2	Scientific achievements	17
1.2.1	<i>Mean statistics</i>	17
1.2.2	<i>Case studies</i>	18
1.2.3	<i>Comparison of AMVs to wind profiles from ADM-Aeolus:</i>	19
2	INTRODUCTION	20
3	DATA.....	21
3.1	AMV data	21
3.2	Reference observations.....	21
4	COMPARISON OF AMVS TO ECMWF WINDS	23
4.1	Comparison Methods.....	23
4.2	Monthly mean statistics.....	23
4.2.1	<i>AMVs from Meteosat-10 EUMETSAT (Met10EUM) IR imagery</i>	23
4.2.2	<i>AMVs from Metop IR imagery</i>	36
5	COMPARISON OF AMVS TO REFERENCE OBSERVATIONS	42
5.1	MISR stereo AMVs	42
5.2	RAOB IGRA winds	45
5.3	CALIPSO/CALIOP cloud top heights.....	46
5.4	CLOUDSAT/CPR cloud type classification	48
5.5	Outgoing Long-wave radiation (OLR)	49
5.5.1	<i>Accumulated OLR from ECMWF</i>	49
5.5.2	<i>OLR from AIRS</i>	52
5.5.3	<i>OLR from FY2E/FY2G</i>	52
5.6	Stability indices – the Galvez-Davison Index (GDI)	55
5.6.1	<i>GDI from ECMWF</i>	56
5.6.2	<i>GDI from ATOVS</i>	56
6	CASE STUDIES	61
6.1	Met10EUM AMV performance over Sahara desert	61
6.1.1	<i>Analysis of semivariograms</i>	61
6.1.2	<i>Visual comparison of wind fields</i>	69
6.2	Metop AMV performance over the Boiler-box region	77
7	COMPARISON TO WIND PROFILES FROM ADM-AEOLUS	89
7.1	Data and methods	89
7.1.1	<i>Data availability and screening</i>	89
7.1.2	<i>HLOS forward model</i>	90
7.1.3	<i>Collocation criteria</i>	90
7.2	Comparison statistics.....	91
7.2.1	<i>Mean statistics</i>	91
7.2.2	<i>Ascending vs descending orbit</i>	94

	<p align="center">Study of AMV speed biases in the tropics</p> <p align="center">Final Report</p>	
Reference: AMV-TN-0008-TS_Ed1_Rev3	Date : 18/06/2020	Page : 7/118

7.2.3	<i>Best-fit pressure statistics</i>	<i>96</i>
7.3	Case studies.....	103
7.3.1	<i>Case 1 - Winds over Arabian Peninsula in October 2019</i>	<i>103</i>
7.3.2	<i>Case 2 - Winds over Indian Ocean October-November 2019</i>	<i>110</i>
8	SUMMARY AND RECOMMENDATIONS	112
8.1	Mean statistics	112
8.2	Case studies.....	112
8.3	Comparison to ADM-Aeolus.....	113
8.4	Recommendations	113
9	REFERENCES	116
ANNEXE A : COMPARISON OF AMVS FROM METEOSAT-7, GOES-13 AND -15, FYE/G TO ECMWF FORECAST WINDS		118

	<p align="center">Study of AMV speed biases in the tropics</p> <p align="center">Final Report</p>	
Reference: AMV-TN-0008-TS_Ed1_Rev3	Date : 18/06/2020	Page : 8/118

List of Figures

Figure 4.1 : Vertical profiles of seasonal O-B speed bias for different latitude bands obtained from ECMWF winds and Met10EUM AMVs derived from IR imagery. The reddish area denotes the corresponding standard deviation of the mean wind speed differences derived for the 35°S to 35°N latitude band.....	24
Figure 4.2 : Geographic distribution of tropical Met10EUM wind speeds averaged for high levels ($p \leq 400$ hPa) and over a $2^\circ \times 2^\circ$ latitude x longitude grid. Collocation criteria as described in Sec. 3.1 are used.	25
Figure 4.3 : Geographic distribution of tropical ECMWF wind speeds averaged for high levels ($p \leq 400$ hPa) and over a $2^\circ \times 2^\circ$ latitude x longitude grid. Only ECMWF data collocated with Met10EUM AMVs are used to calculate mean wind speeds.	26
Figure 4.4 : Geographic distribution of tropical Met10EUM wind speeds against collocated ECMWF winds. O-B speed bias is averaged for high levels ($p \leq 400$ hPa) and over a $2^\circ \times 2^\circ$ latitude x longitude grid.	27
Figure 4.5 : Pressure assigned to Met10EUM AMV (p_{AMV}) vs collocated best-fit pressure ($p_{best-fit}$). Differences $p_{AMV} - p_{best-fit}$ are averaged for high-level winds ($p \leq 400$ hPa) and over a $2^\circ \times 2^\circ$ latitude x longitude grid.....	28
Figure 4.6 : Diurnal cycle of Met10EUM O-B speed bias for three zonal bands (35°S-15°S, 15°S-15°N, 15°N-35°S) and high-level winds.....	29
Figure 4.7 : As Figure 4.6, but only positive Met10EUM-ECMWF wind speed differences are used.	30
Figure 4.8 : As Figure 4.6, but only negative Met10EUM-ECMWF wind speed differences are used.....	30
Figure 4.9 : As Figure 4.4, but for mid-level winds ($400 \text{ hPa} < p \leq 700 \text{ hPa}$).....	31
Figure 4.10 : Pressure assigned to Met10EUM AMV (p_{AMV}) vs collocated best-fit pressure ($p_{best-fit}$). As Fig. 4 but differences $p_{AMV} - p_{best-fit}$ are averaged for mid-level winds ($400 \text{ hPa} < p \leq 700 \text{ hPa}$).	32
Figure 4.11 : Diurnal cycle of Met10EUM O-B speed bias for three zonal bands (35°S-15°S, 15°S-15°N, 15°N-35°S) and mid-level winds.	33
Figure 4.12 : As Figure 4.4, but for low-level winds ($p > 700 \text{ hPa}$).	34
Figure 4.13 : Pressure assigned to Met10EUM AMV (p_{AMV}) vs collocated best-fit pressure ($p_{best-fit}$). As Figure 4.5, but differences $p_{AMV} - p_{best-fit}$ are averaged for mid-level winds ($p > 700 \text{ hPa}$).	35
Figure 4.14 : Diurnal cycle of Met10EUM's O-B speed bias for three zonal bands (35°S-15°S, 15°S-15°N, 15°N-35°S) and low-level winds.	36
Figure 4.15 : As Figure 4.1 but for Dual-Metop AMVs.	37
Figure 4.16 : Geographic distribution of tropical Metop wind speed against collocated ECMWF winds. O-B speed bias is averaged for high levels ($p \leq 400$ hPa) and over a $2^\circ \times 2^\circ$ latitude x longitude grid.	38
Figure 4.17 : Geographic distribution of tropical Metop wind speeds averaged for high levels ($p \leq 400$ hPa) and over a $2^\circ \times 2^\circ$ latitude x longitude grid. Collocation criteria as described in Sec. 4.1 are used.	38


	Study of AMV speed biases in the tropics Final Report	
Reference: AMV-TN-0008-TS_Ed1_Rev3	Date : 18/06/2020	Page : 9/118

Figure 4.18 : Pressure assigned to Metop AMV (p_{AMV}) vs collocated best-fit pressure ($p_{best-fit}$). Differences $p_{AMV} - p_{best-fit}$ are averaged for high levels ($p \leq 400$ hPa) and over a $2^\circ \times 2^\circ$ lat x lon grid. 39

Figure 4.19 : Geographic distribution of Metop wind speed against collocated ECMWF winds. O-B bias is averaged for mid-levels ($400 \text{ hPa} < p \leq 700 \text{ hPa}$) and over a $2^\circ \times 2^\circ$ latitude x longitude grid. 39

Figure 4.20 : Geographic distribution of tropical Metop wind speeds averaged for mid levels ($400 \text{ hPa} < p \leq 700 \text{ hPa}$) and over a $2^\circ \times 2^\circ$ latitude x longitude grid. Collocation criteria as described in Sec. 4.1 are used..... 40

Figure 4.21 : Pressure assigned to Metop AMV (p_{AMV}) vs collocated best-fit pressure ($p_{best-fit}$). Differences $p_{AMV} - p_{best-fit}$ are averaged for mid-levels ($400 \text{ hPa} < p \leq 700 \text{ hPa}$) and over a $2^\circ \times 2^\circ$ latitude x longitude grid. 40

Figure 4.22 : Geographic distribution of tropical Metop wind speed against collocated ECMWF winds. O-B bias is averaged for low levels ($p > 700 \text{ hPa}$) and over a $2^\circ \times 2^\circ$ latitude x longitude grid. 41

Figure 5.1 : Monthly profiles of mean differences between Met10EUM AMV and MISR wind speeds (red line) and corresponding standard deviation (light red shades). 43

Figure 5.2 : Monthly profiles of mean differences between Metop AMV and MISR wind speeds (red line) and corresponding standard deviation (light red shades). 44

Figure 5.3 : Geographic distribution of tropical Metop wind speeds against MISR winds averaged for high levels ($p \leq 400 \text{ hPa}$) and over a $5^\circ \times 5^\circ$ latitude x longitude grid. Collocation criteria as described in Sec. 5.1 are used. 45

Figure 5.4 : Profile of mean Metop-RAOB wind speed differences (blue) and corresponding standard deviation (blue shaded area). RAOB were collocated with Metop using criteria introduced in Sec. 3. 46

Figure 5.5 : Comparison of CALIPSO cloud top height with available Met10EUM AMVs. (Black) Box-and-whisker plots of AMV-CALIPSO pressure ($p_{AMV} - p_{CALIPSO}$) difference are shown for different AMV pressure levels, whereby each box contains data in a pressure range of 50 hPa. Each box extends from the lower to upper quartile values of the pressure differences, with a red line at the median. Corresponding O-B speed bias is shown in blue, while corresponding ECMWF speeds are shown in red. Numbers in the left part of each figure denote the number of collocations used to calculate pressure differences. No CALIPSO data were available for February 2016. 47

Figure 5.6 : Correlation of CLOUDSAT cloud types with observed O-B speed bias of Met10EUM AMVs against ECMWF winds for (a) high-level clouds, (b) mid-level and (c) low-level clouds. Horizontal blue lines denote mean wind speed differences Met10EUM AMV - ECMWF, while vertical blue lines denote the corresponding standard deviation. CLOUDSAT groups clouds into cirrus (1), altostratus (2), altocumulus (3), stratus (4), stratocumulus (5), cumulus (6, including cumulus congestus), nimbostratus (7) and deep convection (8). Depicted are also geographical distribution of CLOUDSAT and Met10EUM AMV collocations for (d) high-level clouds, (e) mid-level and (f) low-level clouds. Results for 8 months averages are presented (January to August). 49

Figure 5.7 : Comparison of ECMWF OLR (step range = 1, see text) with Met10EUM AMVs. Box-and-whisker plots of OLR are shown for different AMV pressure levels. Each box extends from the lower to upper quartile values of the pressure differences, with a line at the median. Corresponding O-B speed bias is shown in blue, while ECMWF speeds are shown in red. 51

Figure 5.8 : As Figure 5.7, but for Metop AMVs. 51


	Study of AMV speed biases in the tropics Final Report	
Reference: AMV-TN-0008-TS_Ed1_Rev3	Date : 18/06/2020	Page : 10/118

Figure 5.9 : Comparison of AIRS OLR with Met10EUM AMVs. Black horizontal lines denote the mean OLR plus corresponding standard deviations. Corresponding O-B speed bias (Met10EUM-ECMWF) is shown in blue, while collocated ECMWF wind speed is shown in red. 53

Figure 5.10 : As Figure 5.9, but for AIRS OLR and Metop AMV. 54

Figure 5.11 : As Fig. 30 but for collocated OLR and AMV from FY2G and FY2E, respectively. (Left) Mean and standard deviation of matched FY2G OLR vs FY2G AMV-ECMWF in December 2016. (Right) Mean and standard deviation of matched FY2E OLR vs FY2E AMV-ECMWF in June 2016. 55

Figure 5.12 : Correspondence between GDI values and expected type of convection. Figure adapted from <http://www.wpc.ncep.noaa.gov/international/gdi/> 56

Figure 5.13 : Comparison of ECMWF GDI with Met10EUM AMVs. Box-and-whisker plots of GDI are shown for different AMV pressure levels. Each box extends from the lower (25%) to upper quartile (75%) values of the pressure differences, with a line at the median. Corresponding O-B speed bias is shown in blue, while ECMWF speeds are shown in red. The grey vertical stripes denote the border of the different convective regimes according to Figure 5.12. 57

Figure 5.14 : As Figure 5.13, but for Metop AMVs. 59

Figure 5.15 : Comparison of ATOVS GDI with Met10EUM AMVs. Black horizontal lines denote the mean GDI values plus corresponding standard deviations. Corresponding O-B speed bias (Met10EUM-ECMWF) is shown in blue, while ECMWF speed is shown in red. The grey vertical stripes denote the border of the different convective regimes according to Figure 5.12. 59

Figure 5.16 : As Figure 5.15, but for Metop AMVs. 60

Figure 6.1 : 7-day jet situation (22.3 – 28.3.2016) over Northern Africa as seen by Met10EUM and ECMWF. (Left) Mean wind speed observed by Met10EUM at high-, mid- and low-level. (Centre) Mean wind speed observed by ECMWF at high-, mid- and low-level. (Right) Corresponding wind speed differences between Met10EUM and ECMWF. 62

Figure 6.2 : Observed and model winds over the Sahara desert at the 200 hPa, averaged from 22.3 to 28.3.2016. Depicted are ECMWF winds (red) and AMV from Met10EUM (blue) over $\pm 1.5^\circ$ longitude bands (transects). 63

Figure 6.3: Semivariograms along North-South transects of observed (AMV) and model (ECMWF) winds over the Sahara desert at the 200 hPa, averaged from 22.3 to 28.3.2016. 64

Figure 6.4 : Observed and model winds over the Sahara desert at the 300 hPa, averaged from 22.3 to 28.3.2016. Depicted are ECMWF winds (red) and AMV from Met10EUM (blue) over $\pm 1.5^\circ$ longitude bands (transects). 65

Figure 6.5: Semivariograms along North-South transects of observed (AMV) and model (ECMWF) winds over the Sahara desert at the 300 hPa, averaged from 22.3 to 28.3.2016. 66

Figure 6.6 : Observed and model winds over the Sahara desert at the 400 hPa, averaged from 22.3 to 28.3.2016. Depicted are ECMWF winds (red) and AMV from Met10EUM (blue) over $\pm 1.5^\circ$ longitude bands (transects). 67

Figure 6.7 : Semivariograms along North-South transects of observed (AMV) and model (ECMWF) winds over the Sahara desert at the 400 hPa, averaged from 22.3 to 28.3.2016. 68


	Study of AMV speed biases in the tropics Final Report	
Reference: AMV-TN-0008-TS_Ed1_Rev3	Date : 18/06/2020	Page : 11/118

Figure 6.8 : CLOUDSAT overpass on 3 March 2016 at 14:41 UTC. Wind barbs denote the Met10EUM found within ± 30 min of the CLOUDSAT overpass. Green wind bars are within $\pm 0.4^\circ$ latitude and $\pm 0.4^\circ$ longitude of the CLOUDSAT overpass. 69

Figure 6.9 : Observed and model winds for a CLOUDSAT overpass over the Sahara desert on 3 March, 14:41 UTC. (Blue) ECMWF wind fields. (Red arrows) AMV obtained within $\pm 0.4^\circ$ latitude and $\pm 0.4^\circ$ longitude and ± 30 min of the CLOUDSAT overpass. (Black dots) Cloud top height computed from CPR data. (Green crosses) Height of a second cloud layer computed from CPR data. Numbers in the square bracket denote latitude and longitude information of the transect. Each ECMWF pressure level is surrounded by two grey lines, indicating the upper and lower limit of the $\Delta p \leq 25$ hPa collocation criterion used to derive mean statistics presented in Section 4.2. 70

Figure 6.10 : Model wind vs Met10EUM AMVs during a CLOUDSAT overpass over the Sahara desert on 3 March, 14:41 UTC. (Upper panel): Wind speed differences between AMV and model winds interpolated to the AMV altitude. The blue plus sign indicates that the observed difference is larger than 9.5 ms^{-1} . (Lower panel): Corresponding wind speed of AMV and model. 71

Figure 6.11 : CLOUDSAT overpass on 25 March 2016 at 14:04 UTC. Wind barbs denote the Met10EUM found within ± 30 min of the CLOUDSAT overpass. Green wind bars are within $\pm 0.4^\circ$ latitude and $\pm 0.4^\circ$ longitude of the CLOUDSAT overpass. 72

Figure 6.12 : Observed and model winds for a CLOUDSAT overpass over the Sahara desert on 25 March, 14:04 UTC. (Blue) ECMWF wind fields. (Red arrows) AMV obtained within $\pm 0.4^\circ$ latitude and $\pm 0.4^\circ$ longitude and ± 30 min of the CLOUDSAT overpass. (Black dots) Cloud top height computed from CPR data. (Green crosses) Height of a second cloud layer computed from CPR data. 72

Figure 6.13 : Model wind vs Met10EUM AMVs during a CLOUDSAT overpass over the Sahara desert on 25 March, 14:04 UTC. (Upper panel): Wind speed differences between AMV and model winds interpolated to the AMV altitude. (Lower panel): Corresponding wind speed of AMV and model. 73

Figure 6.14 : Observed and model winds for a CLOUDSAT overpass over the Sahara desert on 3 March, 14:41 UTC. (Blue) ECMWF wind fields. (Red arrows) AMV obtained within $\pm 0.4^\circ$ latitude and $\pm 0.4^\circ$ longitude and ± 30 min of the CLOUDSAT overpass. (Grey and light blue symbols) Cloud type classification at top of cloud as given by CLOUDSAT. Numbers in the square bracket denote latitude and longitude information of the transect. Each ECMWF pressure level is surrounded by two grey lines, indicating the upper and lower limit of a $\Delta p \leq 25$ hPa collocation criterion used to derive mean statistics presented in Section 4.2. 74

Figure 6.15 : Similar to Figure 6.14, but for a CLOUDSAT overpass over the Sahara desert on 25 March, 14:04 UTC. 75

Figure 6.16 : Comparison of CALIPSO cloud top height with Met10EUM AMV for two weeks in March 2016 over Saharan desert [$18^\circ\text{N} < \text{latitude} < 32^\circ\text{N}$; -15°E , longitude $< 10^\circ\text{E}$]. (Black) Mean difference (Δp) between AMV pressure (p_{AMV}) and CALIPSO cloud top pressure (p_{CALIPSO}) and corresponding standard deviation. Corresponding O-B speed bias is shown in blue, while corresponding speed of model winds ECMWF and satellite winds are shown as solid red line and dashed red line, respectively. The method outlaid in Sec. 5.4 is used to collocate CALIPSO and AMVs and derive pressure differences over this region of interest. 76

Figure 6.17 : Outgoing Longwave Radiation (OLR) in Wm^{-2} , computed from ECMWF fields over the Boiler-Box region on 8 August 2016, 13:00 UTC. 77


	Study of AMV speed biases in the tropics Final Report	
Reference: AMV-TN-0008-TS_Ed1_Rev3	Date : 18/06/2020	Page : 12/118

Figure 6.18 : North-south transect of Metop AMVs (red) and model winds (blue) for a Metop overpass at about 142°E on 8 March, 21:09 local time. Collocated RAOB wind data at 142°E, 15°N are plotted in green. The black solid line denotes the thermal tropopause calculated from high resolution ECMWF temperature fields (137 level resolution). 78

Figure 6.19 : North-south transect of Metop AMVs (red) and model winds (blue) for a Metop overpass at about 139°E on 8 March, 21:09 local time. 79

Figure 6.20 : North-south transect of Metop AMVs (red) and model winds (blue) for a Metop overpass at about 138.5°E on 8 March, 21:09 local time. 80

Figure 6.21 : North-south transect of Metop AMVs (red) and model winds (blue) for a Metop overpass at about 142°E on 8 March, 21:09 local time. Similar to Figure 6.18, but model winds are plotted against the best-fit pressure, which are assigned to AMVs (see text). 81

Figure 6.22 : North-south transect of Metop AMVs (red) and model winds (blue) for a Metop overpass at about 136°E on 12 March, 11:10 local time. 82

Figure 6.23 : North-south transect of Metop AMVs (red) and model winds (blue) for a Metop overpass at about 136.5°E on 12 March, 11:10 local time. 83

Figure 6.24 : AVHRR IR counts for the Metop image pairs, used in the algorithm to extract the AMVs displayed in Figure 6.22 and Figure 6.23 (morning overpass). 84

Figure 6.25 : Brightness temperature (TB) fields derived from AVHRR IR counts. TB is plotted for the Metop image pairs, used in the algorithm to extract the AMVs displayed in Figure 6.22 and Figure 6.23 (morning overpass). 85

Figure 6.26 : AVHRR IR counts for the Metop image pairs, used in the algorithm to extract the AMVs displayed in Figure 6.18 to Figure 6.20 (evening overpass). 86

Figure 6.27 : Brightness temperature (TB) fields derived from AVHRR IR counts. TB is plotted for the Metop image pairs, used in the algorithm to extract the AMVs displayed in Figure 6.18 to Figure 6.20 (evening overpass). 87

Figure 6.28 : Zoom to the brightness temperature field displayed in Figure 6.25. Note the different scale for the brightness temperature compared to Figure 6.25 and Figure 6.27. Dual-Metop AMVs, derived from this image pair, are shown as black arrows. 88

Figure 7.1 : Cumulative frequency of horizontal integration length for Mie and Rayleigh channel in October 2019 in the tropics (35°S < latitude < 35°N). 90

Figure 7.2 : Wind situation along two ADM-Aeolus orbits over Arabia. (a) ADM-Aeolus passes (ascending orbit) over Arabia on 24 October 2019 at 14:59 UTC. (b) ADM-Aeolus passes (ascending orbit) over Arabia on 23 October 2019 at 14:46 UTC. (Upper panel, left) Red point indicate ADM-Aeolus data from Mie channel, while blue points indicate data from Rayleigh channel. Collocated AMVs from Meteosat-8 are displayed as yellow (WV channel), green (IR) and grey (VIS) arrows. (Upper panel, right). ECMWF wind speeds along ADM-Aeolus orbit. (Lower panel, left). HLOS wind speed from collocated ADM-Aeolus (Mie channel), ECMWF and Meteosat-8 (IR channel) as function of pressure. (Lower panel, right). HLOS wind speed from collocated ADM-Aeolus (Rayleigh channel), ECMWF and Meteosat-8 (WV channel) as function of pressure. 91


	<p style="text-align: center;">Study of AMV speed biases in the tropics</p> <p style="text-align: center;">Final Report</p>	
Reference: AMV-TN-0008-TS_Ed1_Rev3	Date : 18/06/2020	Page : 13/118

Figure 7.3 : Scatterplots of HLOS winds from Mie-channel ADM-Aeolus data ($HLOS_{ADM}$) against HLOS winds derived from (a) Meteosat-8 and (b) Meteosat-11 IR AMVs. 92

Figure 7.4 : Scatterplots of HLOS winds from Rayleigh-channel ADM-Aeolus data ($HLOS_{ADM}$) against HLOS winds derived from (a) Meteosat-8 and (b) Meteosat-11 WV AMVs. 93

Figure 7.5 : Scatterplots of HLOS winds from Mie-channel ADM-Aeolus data ($HLOS_{ADM}$) against HLOS winds derived from (a) Meteosat-8 and (b) Meteosat-11 VIS AMVs. 94

Figure 7.6 : Scatterplots of HLOS winds from Mie-channel ADM-Aeolus data ($HLOS_{ADM}$) against HLOS winds derived from (a, b) Meteosat-8 and (c, d) Meteosat-11 IR AMVs. (Left column) Results for ascending orbit. (Right column) Results for descending orbit. 95

Figure 7.7 : Scatterplots of HLOS winds from Rayleigh-channel ADM-Aeolus data ($HLOS_{ADM}$) against HLOS winds derived from (a, b) Meteosat-8 and (c, d) Meteosat-11 WV AMVs. (Left column) Results for ascending orbit. (Right column) Results for descending orbit. 96

Figure 7.8 : Rayleigh/clear ADM-Aeolus pressure against Meteosat-8 WV AMV pressure (Upper panel). Meteosat-8 pressure against ADM-Aeolus for (a) ascending and (b) descending orbit. R denotes Pearson's correlation coefficient, μ the mean differences between ADM-Aeolus and Meteosat-8 and σ the standard deviation of the pressure differences. N denotes the sample size used to calculate σ , μ and R . (Lower panel) Mean pressure differences and corresponding standard deviation of 100 hPa thick layers. 98

Figure 7.9 : As Figure 7.8 but pressures assigned to Meteosat-11 WV AMVs are compared to ADM-Aeolus Rayleigh/clear HLOS winds. 99

Figure 7.10 : Relative sample size of Rayleigh/clear ADM-Aeolus - Meteosat-11 IR AMV best-fit pressure collocations as function of allowed pressure difference $|\Delta p|$. Each AMV was searched for a collocated wind profile of ADM-Aeolus and the element of this wind profile that minimizes the HLOS difference to the AMV within an allowed pressure difference Δp is added to the sample. The obtained size of this sample is then related to the size of the sample where no Δp criterion is imposed. 100

Figure 7.11 : Mie/cloudy ADM-Aeolus pressure against Meteosat-8 IR AMV pressure (Upper panel). Meteosat-8 pressure against ADM-Aeolus for (a) ascending and (b) descending orbit. R denotes Pearson's correlation coefficient, μ the mean differences between ADM-Aeolus and Meteosat-8 and σ the standard deviation of the pressure differences. N denotes the sample size used to calculate σ , μ and R . (Lower panel) Mean pressure differences and corresponding standard deviation of 100 hPa thick layers. 101

Figure 7.12 : As Figure 7.11 but pressures assigned to Meteosat-11 IR AMVs are compared to ADM-Aeolus Mie/cloudy HLOS winds. 102

Figure 7.13 : As Figure 7.10 but the relative sample size of Mie ADM-Aeolus – Meteosat-11 IR AMV collocations is plotted against $|\Delta p|$ 103

Figure 7.14 : High-, mid-, and low-level winds from ECMWF, averaged over the period 22 October 2019 to 29 October 2019. The red box indicates the region for which AMVs and ADM-Aeolus HLOS winds are compared. 104

Figure 7.15 : Scatterplots of HLOS winds from ADM-Aeolus data ($HLOS_{ADM}$) against HLOS winds derived from (a, b) IR AMVs and (c, d) WV AMVs over the Arabian peninsula in October 2019. (Left column) Results for Meteosat-8. (Right column) Results for Meteosat-11. 105


	Study of AMV speed biases in the tropics Final Report	
Reference: AMV-TN-0008-TS_Ed1_Rev3	Date : 18/06/2020	Page : 14/118

Figure 7.16 : Scatterplots of HLOS winds from ADM-Aeolus data ($HLOS_{ADM}$) against HLOS winds derived from ECMWF over the Arabian Peninsula in October 2019. (a) Results for Mie/cloudy HLOS winds. (b) Results for Rayleigh/clear HLOS winds. 106

Figure 7.17 : Mie/cloudy ADM-Aeolus pressure against Meteosat-8 and Meteosat-11 IR AMV pressure. (Left column) Scatter plots of ADM-Aeolus pressure against (a) Meteosat-8 and (b) Meteosat-11 pressure over the Arabian Peninsula in October 2019. (Right column) Mean pressure differences and corresponding standard deviation of 100 hPa thick layers for (c) Meteosat-8 and (d) Meteosat-11..... 107

Figure 7.18 : HLOS winds from Mie/cloudy ADM-Aeolus against HLOS winds derived from (a) Meteosat-8 and (b) Meteosat-11 IR AMV over the Arabian Peninsula in October 2019. AMVs were searched for a collocated wind profile of ADM-Aeolus and the element of this wind profile that minimizes the HLOS difference to the AMV within an allowed pressure difference Δp is plotted against the HLOS AMV. R denotes Pearson's correlation coefficient, μ the mean wind speed difference between ADM-Aeolus and AMV, σ the corresponding standard deviations. N denotes the sample used to compute the speed differences, while the number in bracket sets N in relation to the sample size where no Δp criterion is imposed ("all collocations"). 108

Figure 7.19 : As Figure 7.17 but Rayleigh/clear HLOS winds from ADM-Aeolus are compared against Meteosat-8 and Meteosat-11 WV winds. 109

Figure 7.20 : Scatterplots of HLOS winds from Mie-channel ADM-Aeolus data ($HLOS_{ADM}$) against HLOS winds derived from (a) Meteosat-8 IR AMVs and (b) ECMWF winds over the Indian Ocean..... 110

Figure 7.21 : Scatterplots of HLOS winds from Rayleigh-channel ADM-Aeolus ($HLOS_{ADM}$) against HLOS winds derived from (a, b) Meteosat-8 WV AMVs and (c, d) ECMWF winds over the Indian Ocean. (Upper panel) Results for October 2019. (Lower panel) Results for November 2019. 111

Figure 8.1 : Geographic distribution of tropical MET7 wind speeds against collocated ECMWF winds. O-B speed bias is averaged for high levels ($p \leq 400$ hPa) and over a $2^\circ \times 2^\circ$ latitude x longitude grid. MET7 AMVs are extracted by CIMSS from Meteosat-7 IR imagery. 114


List of Tables

Table 3.1 : Overview of AMV data sets used in this study 21

Table 3.2: Overview of reference data sets used in this study. T denotes temperature, q specific humidity and OLR outgoing longwave radiation. 22


Table 5.1 : Overview RAOB data availability in tropics (latitudes $\leq \pm 35^\circ$) for 2016. Number of radiosondes are grouped into Western Pacific ($90^\circ E < \text{longitude} \leq 150^\circ E$), Indian Ocean ($45^\circ E < \text{longitude} \leq 90^\circ E$) and Africa ($-50^\circ E < \text{longitude} \leq 45^\circ E$). 45

Table 7.1 : Quality criteria applied to HLOS winds from ADM-Aeolus. 89


	<p align="center">Study of AMV speed biases in the tropics</p> <p align="center">Final Report</p>	
Reference: AMV-TN-0008-TS_Ed1_Rev3	Date : 18/06/2020	Page : 15/118

Abbreviations

ADM-AEOLUS	Atmospheric Dynamics Mission - Aeolus
AIRS	Atmospheric Infrared Sounder
ALADIN	Atmospheric LAsER Doppler INstrument
AMSU	Copernicus Atmosphere Monitoring Service
AMV	Atmospheric Motion Vector
ATOVS	Advanced microwave sounding unit
AVHRR	Advanced very-high-resolution radiometer
AWX	Advanced Weather-satellite eXchange format
CALIOP	Cloud-Aerosol Lidar with Orthogonal Polarization
CALIPSO	Cloud-Aerosol Lidar and Infrared Pathfinder Satellite Observations satellite
CIMSS	Cooperative Institute for Meteorological Satellite Studies
CPR	Cloud Profiling Radar
CTH	Cloud Top Height
EUMETSAT	European Organisation for the Exploitation of Meteorological Satellites
EOP	EUMETSAT's Earth Observation Portal
FCI	Flexible Combined Imager
GOES	Geostationary Operational Environmental Satellite
GDI	Galvez-Davison Index
GRIB	GRIdded Binary data format
HDF-EOS	Hierarchical Data Format – Earth Observing System
HIRS	High-resolution Infrared Radiation Sounder
HLOS	Horizontal Line-of-sight
IFS	Integrated Forecast System

	<p align="center">Study of AMV speed biases in the tropics</p> <p align="center">Final Report</p>	
Reference: AMV-TN-0008-TS_Ed1_Rev3	Date : 18/06/2020	Page : 16/118

IGRA	Integrated Global Radiosonde Archive
IR	Infrared
LEO	Low Earth Orbit
MHS	Microwave Humidity Sounder
MISR	Multi-angle Imaging Spectro-Radiometer,
MTG	Meteosat Third Generation
NASA	National Aeronautics and Space Administration
NOAA	National Oceanic and Atmospheric Administration
NSMC	Chinese National Satellite Meteorological Centre
NWP	Numerical Weather Prediction
NWP SAF	Numerical Weather Prediction Satellite Application Facility
O-B	Observation-Background. <i>Here: wind speed differences between satellite wind (AMV) and model wind (ECMWF)</i>
OLR	Outgoing Longwave Radiation
QI	Quality index/indicator
RAOB	RAdiosonde OBservation
SEVIRI	Spinning Enhanced Visible and InfraRed Imager
TB	Brightness temperature
TOA	Top-of-atmosphere
TTR	Top thermal radiation
WV	Water vapour

	<p align="center">Study of AMV speed biases in the tropics</p> <p align="center">Final Report</p>	
Reference: AMV-TN-0008-TS_Ed1_Rev3	Date : 18/06/2020	Page : 17/118

1 EXECUTIVE SUMMARY

1.1 OBJECTIVES

Atmospheric motion vectors derived from geostationary and polar-orbiting satellites by tracking clouds or water vapour features in consecutive satellite images in visible, infrared and water vapour bands constitute an upper tropospheric wind data type that has good areal and temporal coverage, particularly over the southern oceans and at high latitudes. Their assimilation into Numerical Weather Prediction improves the model forecast. Due to their importance for NWP models, careful monitoring and understanding of AMV error characteristics is required. Recent studies (e.g. Horvath et al., 2017; Warnick, 2016) revealed the existence of a positive Observation minus Background (O-B) speed bias in the tropical region of the upper troposphere for most satellite-channel combinations from both geostationary and polar-orbiting satellites, which cannot be explained by erroneous AMV height assignments alone. The goal of the presented study is to investigate if other factors such as the specificities of tropical cloud dynamics (deep convection, horizontal and vertical wind shear, diurnal cycle of humidity, semi-transparent clouds ...) may also affect adversely AMV extraction.


1.2 SCIENTIFIC ACHIEVEMENTS

1.2.1 Mean statistics

The first part of this study contains a comprehensive statistics of AMV performance from different data set providers and satellites (EUMETSAT, CIMSS, NMSC, Meteosat-7 and -10, Metop-A/B, GOES-13 and -15, FY2G/E) against gridded ECMWF forecast winds and against reference observations for the tropical region (between -30°N and 30°N). We used hourly forecast data (from two runs, 00 and 12 UTC) at a horizontal resolution of 0.5° x 0.5° at 19 discrete pressure levels. We mostly focused on AMVs derived by EUMETSAT from IR imagery from Meteosat-10 and Metop satellites.

AMV performance against ECMWF forecast winds: To collocate model winds to AMV datasets, a vertical separation between ECMWF and AMV of less than 25 hPa ($p \leq \pm 25\text{hPa}$), a temporal separation of less than 30 min and a wind direction difference of less than 60° were used. For AMVs derived by EUMETSAT from IR imagery from Meteosat-10 (Met10EUM) and Metop satellites, we found a different pattern of the O-B speed bias at mid- (700 hPa $> p > 400$ hPa) to high levels ($p \leq 400$ hPa). For Meteosat-10, the obtained speed bias was typically smaller than 2 ms⁻¹, while differences larger than 3 ms⁻¹ were commonly found over desertic areas, particularly if large wind speeds occur (subtropical jets). Dual-Metop AMVs report 3-5 ms⁻¹ faster winds than ECMWF for the low wind speed regions around the equator and 3-5 ms⁻¹ slower winds than ECMWF for regions north of 15°N and south of 15°S, with some dependency of the bias on altitude.

AMV performance against MISR stereo-winds: To match MISR stereo winds with AMVs a horizontal collocation criterion has to be additionally introduced and winds separated by less than 150 km were used for comparison. For low-level to mid-level winds, Met10EUM obtains < 1 ms⁻¹ slower winds than MISR. A higher bias was obtained for high-level winds up to 200 hPa, mainly in the range of 1 ms⁻¹ (Met10EUM slower than MISR). In contrast to Met10EUM, Metop winds are, however, faster than MISR winds at these altitudes. Between 200 and 400 hPa, Metop winds are 0.5-2 ms⁻¹ faster than MISR winds. Above this altitude ($p < 200$ hPa), wind speeds differences are typically larger.

	<p align="center">Study of AMV speed biases in the tropics</p> <p align="center">Final Report</p>	
Reference: AMV-TN-0008-TS_Ed1_Rev3	Date : 18/06/2020	Page : 18/118

AMV performance against RAOB radiosondes: As for comparison to MISR winds, comparison of AMVs to RAOB winds requires a horizontal collocation criterion (150 km). RAOB data are distributed very uneven in time and space and only matches with Metop AMVs were found. Between surface and 600 hPa RAOB winds are 2 ms⁻¹ faster than Metop, while above 600 hPa ($p < 600$ hPa) Metop winds are faster than RAOB, up to 5 ms⁻¹.

Impact of diurnal cycle of convection: Comparison of observed O-B speed biases to the diurnal cycle of convection or to quantities describing strength and type of convection such OLR, CLOUDSAT cloud type classification or stability indices revealed no clear dependency of the monthly O-B speed bias to these parameters.

CALIPSO/CALIOP cloud top height: Due to their different orbits, CALIPSO/CALIOP could not be compared to Metop AMVs. For Meteosat-10, we found that difference between collocated AMV pressure and CALIPSO cloud top height is > 0 hPa throughout the atmospheric, which in turn means that AMVs tend to have assigned too low altitudes. On average, pressure differences are largest at 300 and 400 hPa. The latter altitude is also the altitude of largest O-B speed bias of up to 2 ms⁻¹. As AMVs around 400 hPa have assigned too low altitudes, parts of the O-B speed bias obtained at these altitudes may can be attributed to an average 30-hPa incorrect height assignment in conjunction with high wind speeds above 400 hPa ($p < 400$ hPa).


1.2.2 Case studies

In the second part of this study, two cases of AMV performance were studied in detail. The first one studies the Met10EUM IR AMV mid- and high-level speed bias over Saharan desert in March 2016 during westerly jet, while the second investigates the Dual-Metop IR AMV mid- and high-level speed bias over the Boiler-Box region in August 2016.

Met10EUM IR AMV mid- and high-level speed bias over Saharan desert in March 2016. Semivariograms and latitudinal wind speed profiles were used to analyse the spatial structure of AMV (Met10EUM IR imagery) and ECMWF wind fields at high levels, in particularly to verify the jet position in the ECMWF wind field over a 7-day jet westerly jet situation (22.3 – 28.3.2016) over Northern Africa. ECMWF and AMV agree reasonably well at 200 hPa. At the 300-hPa level, results may be interpreted that the jets observed by AMVs reach higher speed levels than ECMWF and may peak at slightly different locations. For the 400-hPa level, results suggest that differences in the altitude of the jet lead to too fast AMVs.

By comparing visually AMVs to model winds along approximately $\pm 0.25^\circ\text{E}$ broad north-south transects, it was found that Met10EUM and model winds agree well over the Western Saharan desert at levels above 250 hPa ($p \leq 250$ hPa). Between 350-500 hPa, altitudes assigned too low lead in conjunction with vertical wind shear and generally fast winds to AMVs being frequently 4-6 ms⁻¹ faster than ECMWF. Comparison to CPR/CLOUDSAT and CALIOP/CALIPSO cloud top heights/pressures confirm these findings. Our results further indicate no dependency of fast wind speed biases on cloud type. In addition, while certain fast wind speed biases coincide with the presence of multilayer clouds, a clear dependency of the fast wind speed biases could not be deduced as in most cases the presence of multilayer clouds did not adversely affect the agreement between model winds and AMV. It would be interesting to see if the use of OCA cloud top heights instead of the current operational CLA-CTH (cloud type and cloud-top height) product can improve the quality of AMV data under such conditions (desert, fast wind speeds and high wind shear).


Dual-Metop IR AMV performance over boiler box. Contrarily to the first case study, height assignment errors unlikely explain why Dual-Metop AMVs are faster than model winds over the Boiler-Box region. Rather the AMV extraction schemes suffer from low correlation between pixels of target box in image 1

	<p align="center">Study of AMV speed biases in the tropics</p> <p align="center">Final Report</p>	
Reference: AMV-TN-0008-TS_Ed1_Rev3	Date : 18/06/2020	Page : 19/118

and those in image 2. The AMV extraction scheme looks for the best pixel-accurate target match that maximizes the two-dimensional cross-correlation coefficient. It, however, does not take into account the fact that the spatial correlation can actually be relatively low. In this sense, it is recommended to derive correlation surfaces of two AVHRR images and flag relevant AMV data if the correlation in the relevant area is low. That is, AMV data should be kept but a variable makes the end users aware that the winds are computed using pixels of low correlation.

1.2.3 Comparison of AMVs to wind profiles from ADM-Aeolus:

AMVs derived from Meteosat-8 and Meteosat-11 imagery were compared to wind profiles measured by the ALADIN instrument aboard ADM-Aeolus (version L2B v3.20) during October to November 2019. Using collocation criteria of $\Delta x < 100$ km, $\Delta t < 30$ min and $\Delta p < 15$ hPa, mean HLOS speed differences between these AMVs and ADM-Aeolus of 0.2 ± 3.4 ms⁻¹ were typically obtained, depending on altitude, region and on channel. Comparison of altitudes assigned to AMV IR winds (relaxation of the 15-hPa criterion), did not fully confirm previous findings of having too low altitudes assigned to AMVs over desertic areas.

	<p align="center">Study of AMV speed biases in the tropics</p> <p align="center">Final Report</p>	
Reference: AMV-TN-0008-TS_Ed1_Rev3	Date : 18/06/2020	Page : 20/118

2 INTRODUCTION

Atmospheric motion vectors (AMV) are derived from geostationary and polar-orbiting satellites by tracking clouds or water vapour features in consecutive satellite images in visible, infrared and water vapour (WV) bands. Their generation assumes that the tracked features act as passive tracers of the atmospheric flow and displace quasi-horizontally. AMVs are currently treated as single level winds and representative pressures—typically an estimate of the cloud top height or the cloud base—and a quality indicator (QI) are assigned during their generation. Although AMVs do not provide wind profile information, AMVs are continuously assimilated in various Numerical Weather Prediction (NWP) models (Bormann et al. (2012), Forsythe et al. (2014), Salonen et al. (2015), and references therein). Since they constitute an upper tropospheric wind data type that has good areal and temporal coverage, particularly over the southern oceans and at high latitudes, the model forecast score is improved.

Due to the importance of AMV products for NWP models, careful monitoring and understanding of AMV error characteristics is of crucial importance. Recent studies (e.g. Horvath et al., 2017; Warnick, 2016) revealed the existence of a positive Observation minus Background (O-B) speed bias in the tropical region of the upper troposphere for most satellite-channel combinations from both geostationary and polar-orbiting satellites. Thus, AMV products are faster than corresponding model wind fields. This speed bias was found largest at mid-level (400-700 hPa)

Erroneous altitudes assigned to AMVs often explain observed O-B speed biases. However, also other factors such as the specificities of tropical cloud dynamics (deep convection, gravity waves, wind shear, diurnal cycle of humidity, semi-transparent clouds ...) may adversely affect AMV extraction from satellite imagery. To understand and explain scientifically how the dynamics and physics underlying the tropical atmosphere affect AMVs extracted from satellite imagery constitute the primary goal of this study entitled **“Study of AMV speed biases in the tropics - EUMETSAT Contract No. EUM/CO/18/4600002168/RBo - Order n°4500017165”**. In the first part of this study, a comprehensive statistics of observed wind speed differences (O-B speed bias) between global AMVs and forecast model winds is established and reference data such as CALIPSO/CALIOP cloud top heights or Outgoing Longwave Radiation data from AIRS will be used to ensure a more balanced comparison result. In the second part, selected cases will be studied in more detail to find potential scientific explanations for the observed wind speed biases.

Results are mainly presented for AMVs derived by EUMETSAT from Meteosat-10 IR imagery (Borde et al., 2014) and Metop IR imagery (Borde et al., 2015; Hauteceur and Borde, 2017) as these data are temporally highly resolved and quality indicators are provided. Results for the other AMV datasets and channel/satellite combinations are presented in less detail in a separate document (AMV-TN-0006-TS_Ed1_Rev0_Final_draft_APPENDIX.pdf). We mostly focus on mid- to high-level clouds in this study, as speed biases appear more pronounced than at low-levels. Certain results, however, are also presented for low-level clouds.

3 DATA

3.1 AMV DATA

Given the decision taken during the Kickoff meeting held on November 8, 2016, AMV data were collected for 2016. The choice of this year was justified by analysing most recent AMV extraction schemes and by the availability CLOUDSAT data. Table 3.1 provides an overview of AMV data sets used in this study. Global Metop dual-mode AMVs, Meteosat-10 AMVs (Met10EUM) as well as Expanded Low-resolution Cloud Motion Winds from Meteosat-7 (Met7EUM, 57°E) were downloaded from the EUMETSAT Observation Portal (EOP; <https://eoportal.eumetsat.int/userMgmt/login.faces>).


Table 3.1 : Overview of AMV data sets used in this study

Data set provider	AMV data set	Label	Data format
EUMETSAT	Metop	Metop	EPS Native
EUMETSAT	Meteosat-10	Met10EUM	bufr
EUMETSAT	Meteosat-7	Met7EUM	bufr
CIMSS	GOES-13	GOES13	ascii
CIMSS	GOES-15	GOES15	ascii
CIMSS	Meteosat-7	MET7	ascii
CIMSS	Meteosat-10	MET10	ascii
NSMC	FY2E	FY2E	awx
NSMC	FY2G	FY2G	awx

Data sets from the geostationary satellites GOES-13, GOES-15, Meteosat-7 and Meteosat-10 were obtained from the wind archives of the University of Wisconsin-Madison Cooperative Institute for Meteorological Satellite Studies (CIMSS). These data are typically available on a 3-hourly basis. Finally, AMVs derived from the Chinese satellites FY2E and FY2G were obtained from the Chinese National Satellite Meteorological Center (NSMC). These data are stored in binary format awx (Advanced Weather-satellite eXchange format) and are available on a 3-hourly basis. AMVs from NSMC do not provide quality indicators.

3.2 REFERENCE OBSERVATIONS

In Sec. 4, these AMVs are compared to gridded wind fields from ECMWF's Integrated Forecast System (Table 3.2). We used hourly forecast data (from two runs, 00 and 12 UTC) at a horizontal resolution of 0.5° x 0.5° at 19 discrete pressure level (20, 30, 50, 70, 100 to 300 by 50, 400 to 800 by 100, 850, 900, 925, 950, 1000 hPa). AMVs were also compared to winds from radiosonde observations and to MISR stereo AMVs. The former data set was downloaded from an IGRA ftp server (<ftp://ftp.ncdc.noaa.gov/pub/data/igra/data/data-y2d/>). The number of available radiosondes in the tropics varies strongly among the different years and regions. MISR AMVs were downloaded from NASA (https://eosweb.larc.nasa.gov/project/misr/mi3mcmvn_table) as monthly-aggregated Cloud Motion Vector Product. We used the most recent version F02 0002.

	<p align="center">Study of AMV speed biases in the tropics</p> <p align="center">Final Report</p>	
Reference: AMV-TN-0008-TS_Ed1_Rev3	Date : 18/06/2020	Page : 22/118

Temperature and specific humidity profiles required for GDI computation were obtained from ATOVS, ECMWF's IFS and AIRS. ATOVS data were downloaded from EUMETSAT's EOP. ATOVS is composed of the Advanced Microwave Sounding Unit A (AMSU-A), the Microwave Humidity Sounder (MHS) and the High Resolution Infrared Radiation Sounder (HIRS/4) aboard Metop. T and q profiles from AIRS (and AMSU) aboard AQUA are obtained from https://disc.gsfc.nasa.gov/datasets/AIRX2RET_V006/summary?keywords=airs%20version%206. At the time of downloading, AIRS/AMSU data were available until September 2016. Temperature and humidity are also regularly reported by radiosondes. However, in 2016, no humidity data were reported from tropical radiosondes. Thus, no GDI could be computed from radiosondes.


Table 3.2: Overview of reference data sets used in this study. T denotes temperature, q specific humidity and OLR outgoing longwave radiation.

Type	Data set provider	Data set	Data format
Reference wind	ECMWF	IFS	grib
Reference wind	IGRA	Radiosondes	ascii
Reference wind	NASA	MISR	netcdf
T, q profiles	EUMETSAT	ATOVS	bufr
T, q profiles	IGRA	Radiosondes	ascii
T, q profiles	ECMWF	IFS	ascii
T, q profiles	NASA	AIRS	HDF-EOS
Cloud top pressure	NASA	CALIPSO	HDF-EOS
OLR	NASA	AIRS	HDF-EOS
OLR	ECMWF	IFS	grib
OLR	NSMC	FY2E	awx
OLR	NSMC	FY2G	awx
Cloud layer heights	NASA	CLOUDSAT	HDF-EOS
Cloud type classification	NASA	CLOUDSAT	HDF-EOS
IR radiance	EUMETSAT	AVHRR	netcdf

CALIPSO cloud top pressure were available and downloaded from NASA's EARTH DATA site. CLOUDSAT data are available until August 2016 and were downloaded from <http://www.cloudsat.cira.colostate.edu/order-data>.

OLR data were used from AIRS, ECMWF's IFS, FY2E and FY2G. OLR data from AIRS were included in the same data products as the T and q profiles. However, they were only available until September 24, 2016. OLR from FY2E and FY2G were obtained from NSMC in awx format. As for AMV, NSMC does not provide quality indicators for the OLR products. The net long-wave radiation (TTR) at TOA (top-of-atmosphere) was downloaded from ECMWF. TTR is equal to the negative of the outgoing long-wave radiation (i.e. $OLR = -TTR$; see Hogan, 2014).

In Section 6.2, IR radiance from AVHRR aboard Metop-A and Metop-B will be used. These data were downloaded from EUMETSAT's EOP site and extracted from the "AVHRR GDS Level 1B – Metop" dataset.

	<p align="center">Study of AMV speed biases in the tropics</p> <p align="center">Final Report</p>	
Reference: AMV-TN-0008-TS_Ed1_Rev3	Date : 18/06/2020	Page : 23/118

4 COMPARISON OF AMVS TO ECMWF WINDS

4.1 COMPARISON METHODS

Comparison of AMVs to gridded wind fields from ECMWF requires establishing appropriate vertical and temporal collocation or match criteria. Horvath et al. (2017) is followed to establish appropriate match criteria, i.e., a vertical separation between ECMWF and AMV of less than 25 hPa ($p \leq \pm 25 \text{ hPa}$), a temporal separation of less than 30 min and a wind direction difference of less than 60° is required for comparison. It is possible that more than one AMV are assigned to the same ECMWF grid cell. If this is the case, the median of the concerned AMVs is calculated and compared to ECMWF winds. For a proper comparison to the results of Horvath et al. (2017), the obtained O-B speed biases are not normalised.

With the exception of FY2G and FY2E winds, quality indicators (QI) are reported. In these cases, we considered only AMVs where the QI exceeds a value of 60 (polar satellites, i.e., Metop AMVs) and 80 (geostationary satellites), respectively. Monthly mean statistics are presented as O-B speed bias (AMV-ECMWF) and typically separately for high-level winds ($p \leq 400 \text{ hPa}$), mid-level winds ($400 \text{ hPa} < p \leq 700 \text{ hPa}$) and low-level winds ($p > 700 \text{ hPa}$). To investigate height-assignment differences, the $p \leq \pm 25 \text{ hPa}$ criterion is relaxed and AMV pressures are compared to so-called best-fit pressures. The best-pressure fit is defined as the height at which the vector difference between the observed and the model background wind is smallest. To calculate the best-fit pressure we follow Salonen et al. (2015), who suggest a two-step procedure to obtain best-fit pressure. The first step consists in finding the model level that minimizes the vector difference between AMV and model wind. The second step consists in calculating the "true minimum" by using a parabolic fit to the vector difference for this model level and the two neighbouring levels. Criteria used by Salonen et al. (2015) to eliminate cases for which the best-fit pressure is not well constrained are also applied (Eq. (1) and (2) in Salonen et al., 2015). That is, cases in which there is no good agreement between the AMV wind observation and the model wind at any level are excluded. Secondly, the vector difference must be greater than the minimum difference + 2 ms^{-1} outside a band that encompasses the best-fit pressure $\pm 100 \text{ hPa}$.

4.2 MONTHLY MEAN STATISTICS

4.2.1 AMVs from Meteosat-10 EUMETSAT (Met10EUM) IR imagery

Vertical profiles of wind speed differences: Vertical profiles of the O-B speed bias for different latitude bands are given in Figure 4.1 for different seasons. Below 600 hPa ($p > 600 \text{ hPa}$), mean differences are close to 0 ms^{-1} . Between 300 and 600 hPa, Met10EUM on average observes 0.5 to 3 ms^{-1} faster winds than ECMWF. Above this layer, mean differences change sign as ECMWF reports up to 2 ms^{-1} faster winds, while above 200 hPa ($p < 200 \text{ hPa}$) mean wind speed differences tend become positive again (AMV faster than ECMWF). Note, highest variability of the mean differences is found around 400 hPa.

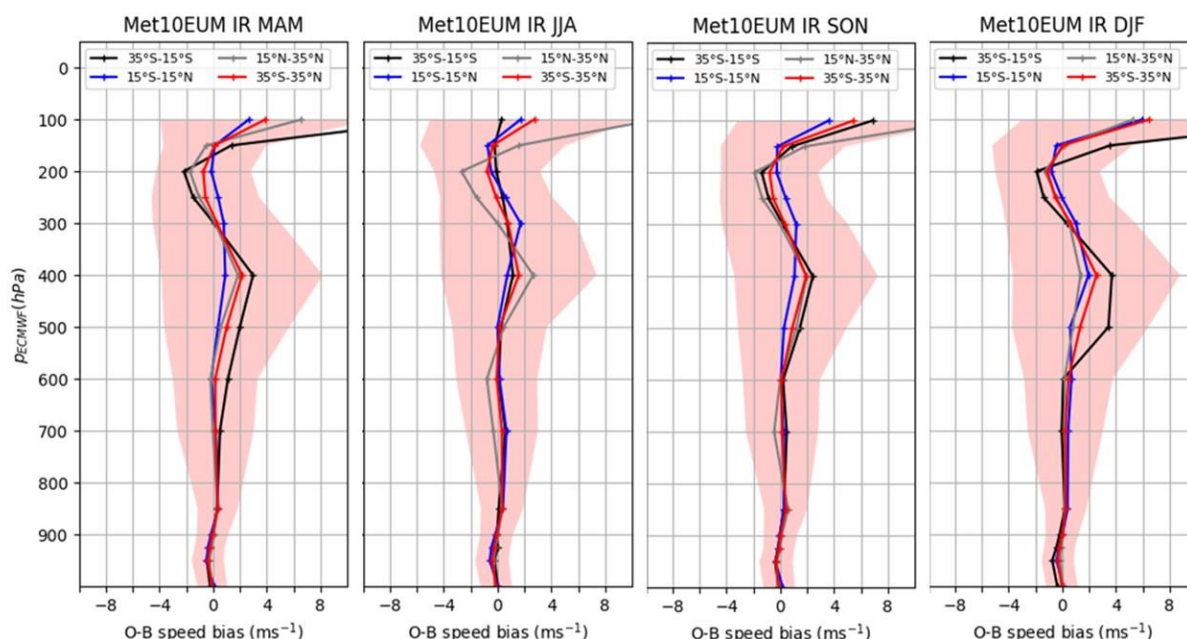


Figure 4.1 : Vertical profiles of seasonal O-B speed bias for different latitude bands obtained from ECMWF winds and Met10EUM AMVs derived from IR imagery. The reddish area denotes the corresponding standard deviation of the mean wind speed differences derived for the 35°S to 35°N latitude band.

High-level winds: Monthly spatial distributions of wind speed derived by Met10EUM IR imagery and by ECMWF is given in Figure 4.2 and Figure 4.3 for high-level winds ($p \leq 400$ hPa), respectively, while the spatial distribution of corresponding wind speed differences (Met10EUM - ECMWF) is given in Figure 4.4. Mean speed discrepancies are around 1 ms^{-1} . Areas of wind speed differences of greater than 3 ms^{-1} commonly coincide with the location the subtropical jet that migrates with the changing position of the thermal equator (e.g. high wind speeds over the Sahara desert in December to March, high wind speeds in Southern Africa from July to August). Negative mean wind differences larger than 5 ms^{-1} are often found over oceans, e.g. over the Gulf of Guinea in January or south of Madagascar in June).

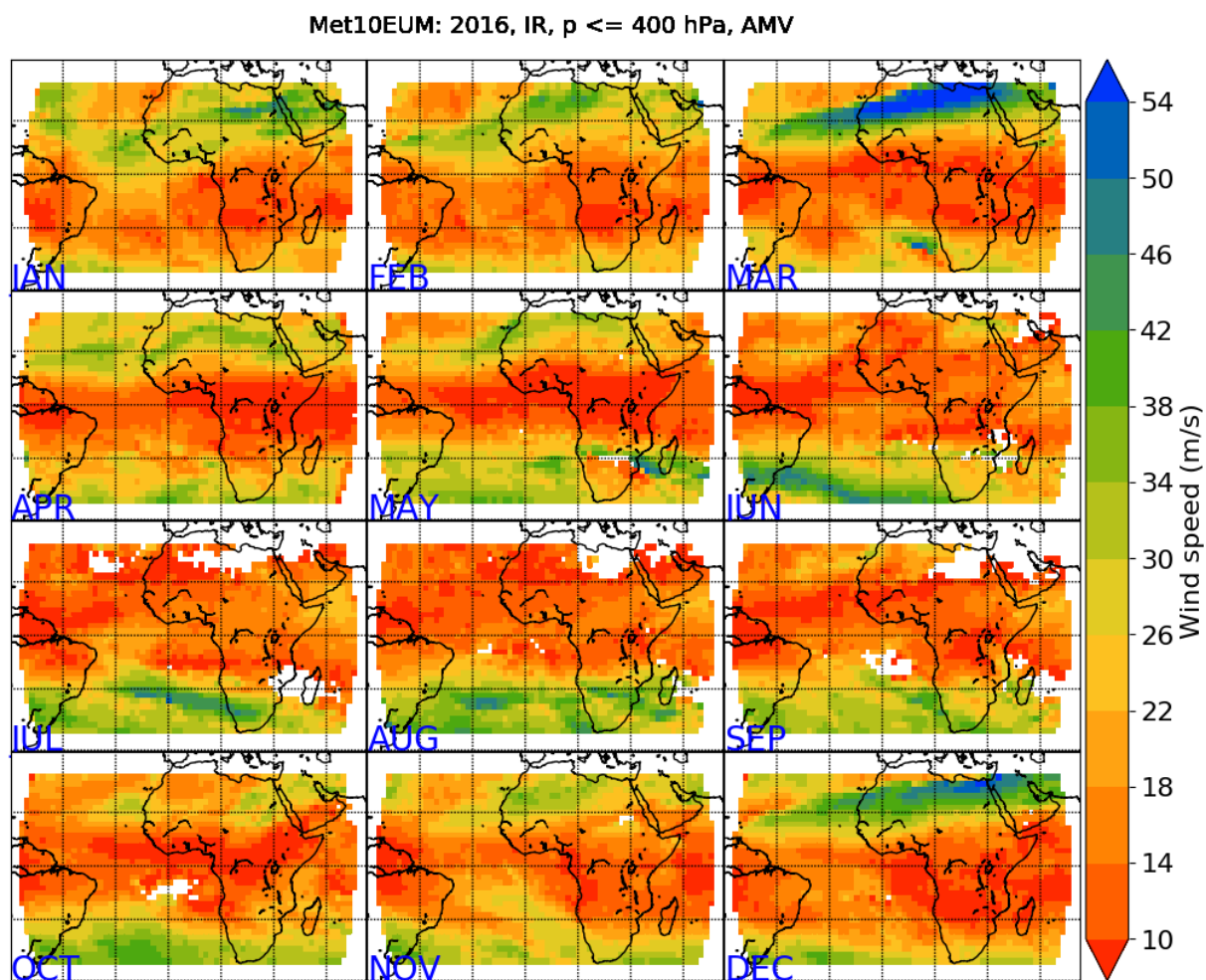


Figure 4.2 : Geographic distribution of tropical Met10EUM wind speeds averaged for high levels ($p \leq 400$ hPa) and over a $2^\circ \times 2^\circ$ latitude x longitude grid. Collocation criteria as described in Sec. 3.1 are used.

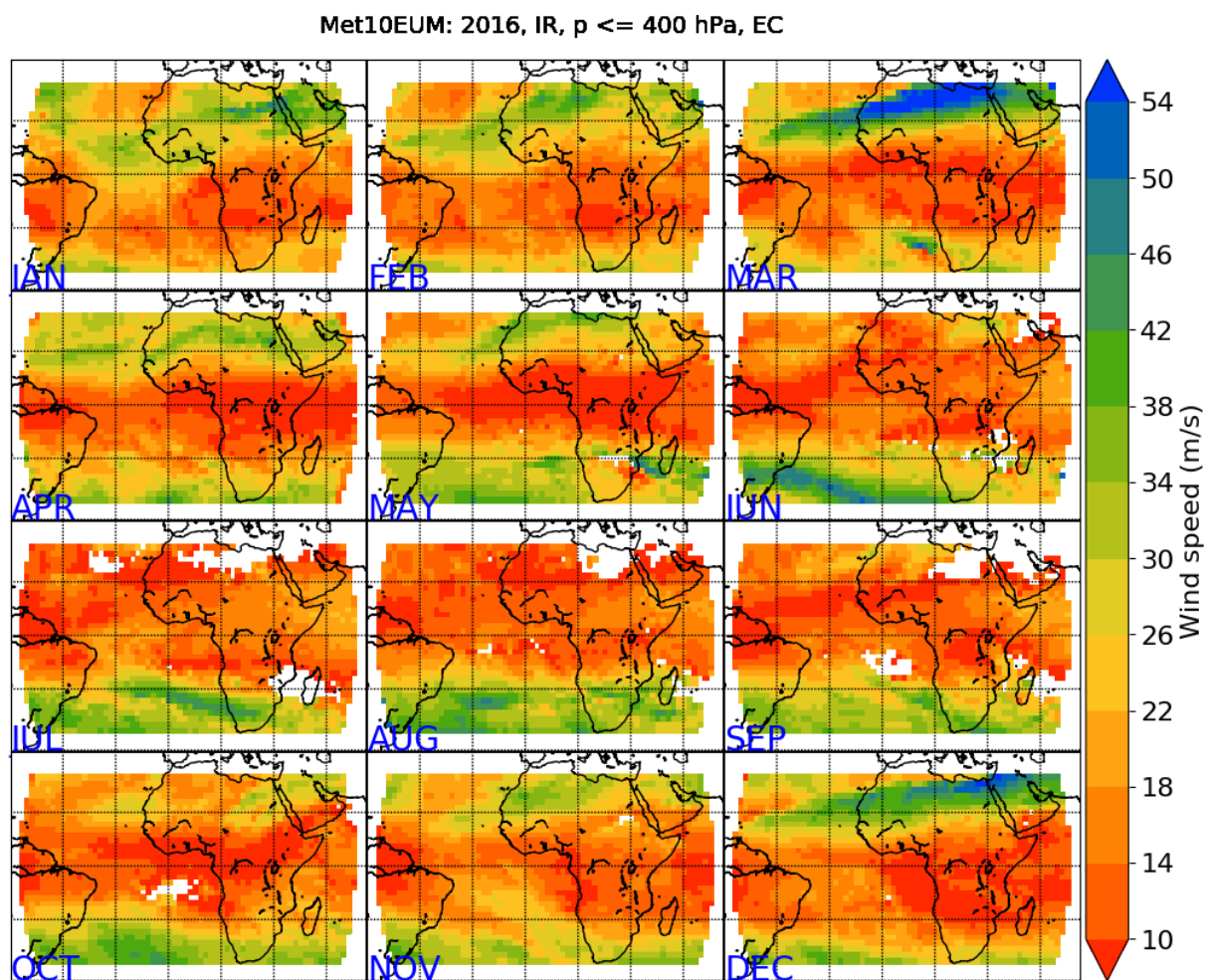



Figure 4.3 : Geographic distribution of tropical ECMWF wind speeds averaged for high levels ($p \leq 400$ hPa) and over a $2^\circ \times 2^\circ$ latitude x longitude grid. Only ECMWF data collocated with Met10EUM AMVs are used to calculate mean wind speeds.

	<p align="center">Study of AMV speed biases in the tropics</p> <p align="center">Final Report</p>	
Reference: AMV-TN-0008-TS_Ed1_Rev3	Date : 18/06/2020	Page : 27/118

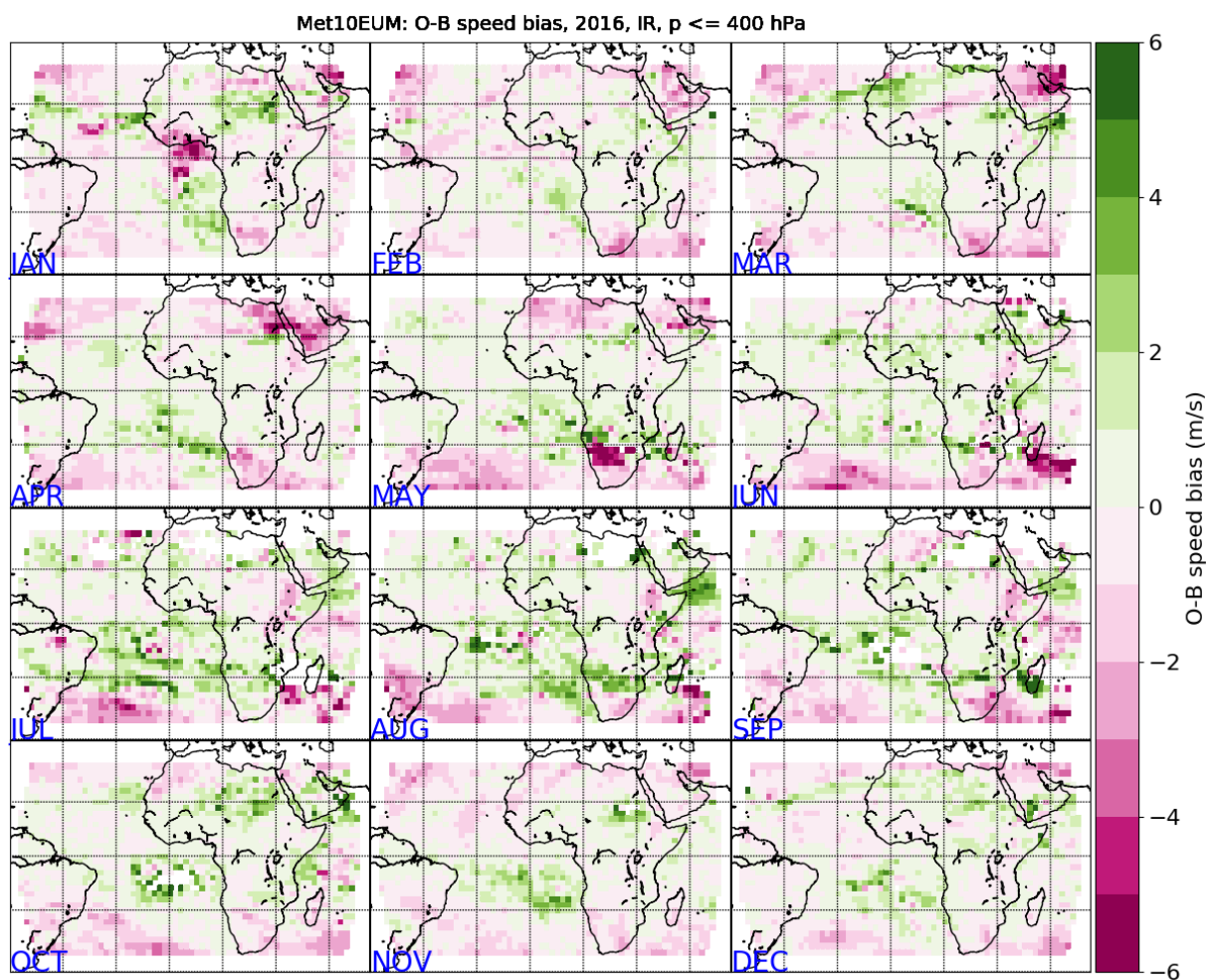


Figure 4.4 : Geographic distribution of tropical Met10EUM wind speeds against collocated ECMWF winds. O-B speed bias is averaged for high levels ($p \leq 400$ hPa) and over a $2^\circ \times 2^\circ$ latitude x longitude grid.

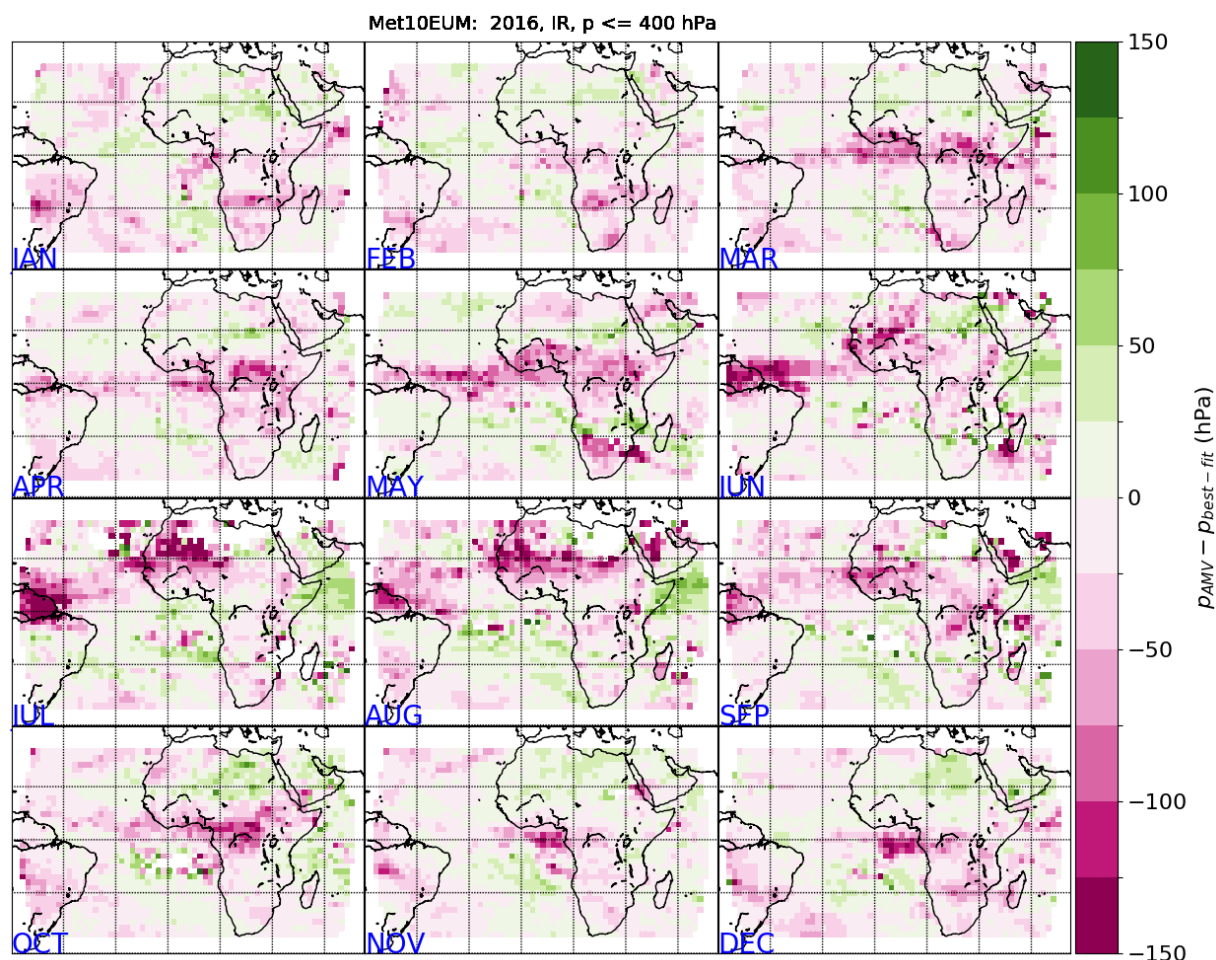


Figure 4.5 : Pressure assigned to Met10EUM AMV (p_{AMV}) vs collocated best-fit pressure ($p_{best-fit}$). Differences $p_{AMV} - p_{best-fit}$ are averaged for high-level winds ($p \leq 400$ hPa) and over a $2^\circ \times 2^\circ$ latitude x longitude grid.

Figure 4.5 reveals that areas of large speed biases do not coincide with those areas exhibiting large differences between pressures assigned to Met10EUM AMVs (p_{AMV}) and best-fit pressures ($p_{best-fit}$). Typically, $p_{AMV} - p_{best-fit}$ is less or equal 25 hPa. By contrast, for high-level winds, largest differences between AMV pressure and best-fit pressure are commonly found around the equator, where wind speed is $< 20 \text{ ms}^{-1}$ and the O-B speed bias is less pronounced ($< 2 \text{ ms}^{-1}$).

Observed speed biases may be linked to the growth and decay of convective cells. In the tropics, differences in the diurnal cycle of convection are apparent between oceans and land. While oceanic deep convection tends to reach its maximum in the early morning, convection over land reaches its maximum in the evening as a result of solar heating (Yang and Slingo, 2000). In a first step, we check if observed O-B speed biases are correlated with the diurnal cycle of convection. To this end, O-B speed biases for three different zonal bands are calculated and plotted against local daytime. Figure 4.6 shows mean wind speed differences between Met10EUM and ECMWF as function of local daytime for high-level winds. The absolute value of O-B speed bias is typically $< 0.5 - 1 \text{ ms}^{-1}$. A clear dependency between bias and diurnal cycle of convection is not visible. Differences in O-B speed biases between different hours is typically $< 0.5 \text{ ms}^{-1}$. Only in July and August, differences of up to 1.5 ms^{-1} are obtained

for the 35°S-15°S zonal band. Note the typical standard deviation of the mean speed differences exceeds the range of the ordinate in the plots (not shown in plots).

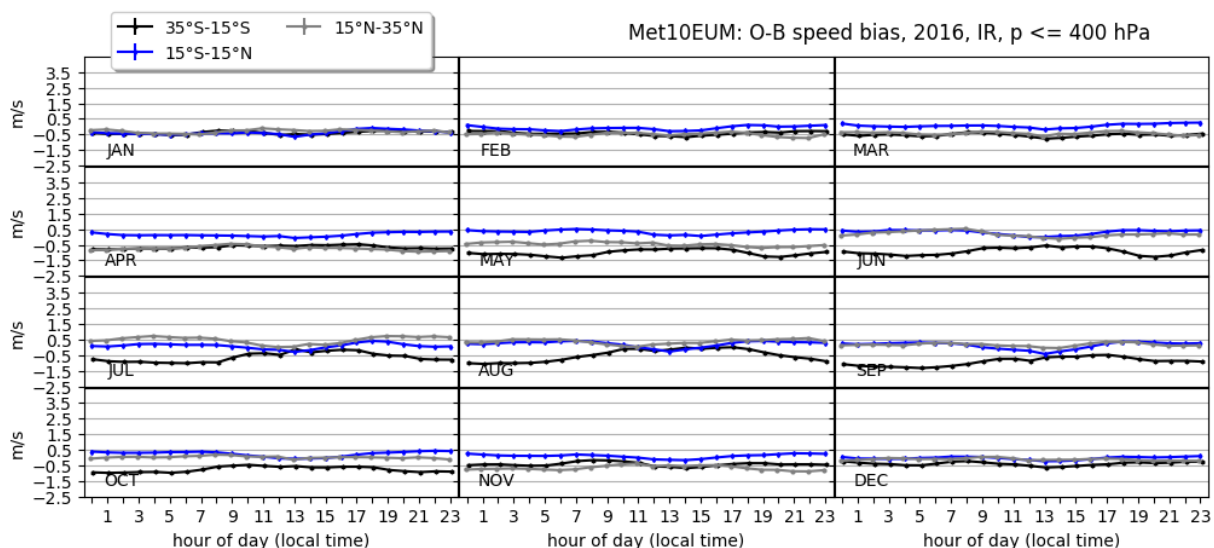



Figure 4.6 : Diurnal cycle of Met10EUM O-B speed bias for three zonal bands (35°S-15°S, 15°S-15°N, 15°N-35°S) and high-level winds.

Figure 4.6 shows that both positive and negative mean wind speed differences are present within one zonal band. By computing the O-B speed bias over such a zonal band, positive and negative biases may balance out, obscuring any diurnal variations of the speed bias. In Figure 4.7 and Figure 4.8, the diurnal cycle of the wind speed bias is plotted for positive differences and negative wind speed differences only, respectively. However, in both case no clear dependency of the speed bias with daytime is apparent. Speed biases vary only slightly with daytime; maximally by 1 ms⁻¹.

	<p align="center">Study of AMV speed biases in the tropics</p> <p align="center">Final Report</p>	
Reference: AMV-TN-0008-TS_Ed1_Rev3	Date : 18/06/2020	Page : 30/118

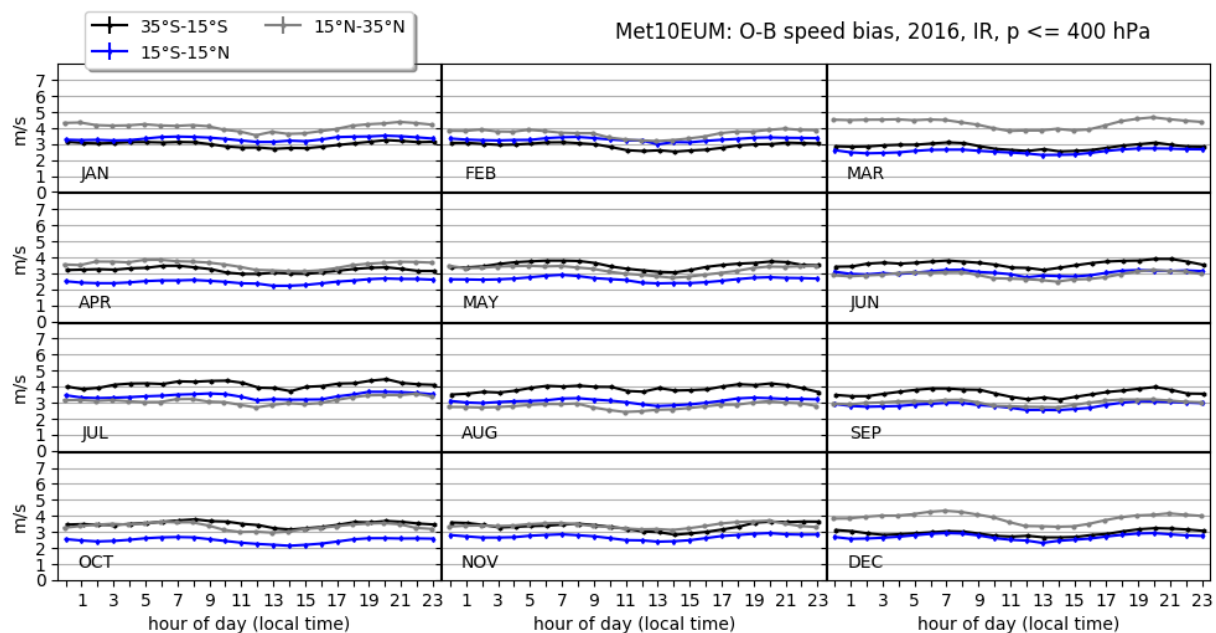


Figure 4.7 : As Figure 4.6, but only positive Met10EUM-ECMWF wind speed differences are used.

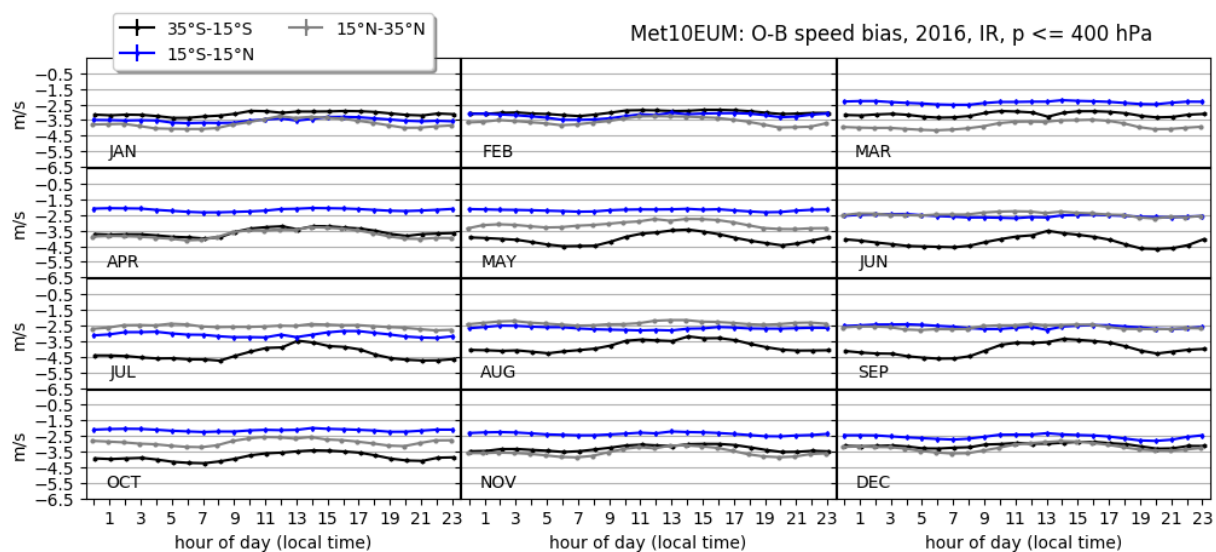


Figure 4.8 : As Figure 4.6, but only negative Met10EUM-ECMWF wind speed differences are used.

Mid-level winds: Figure 4.9 shows the spatial distribution of monthly mean differences between AMV Met10EUM and ECWTF for mid-level winds. Similar to high-level winds, differences $> 6 \text{ ms}^{-1}$ are found over the Sahara desert in the northern hemisphere winter. Conversely, largest wind speed differences during southern hemisphere winter are obtained over the Atlantic Ocean, between Brazil and Namibia/South Africa.

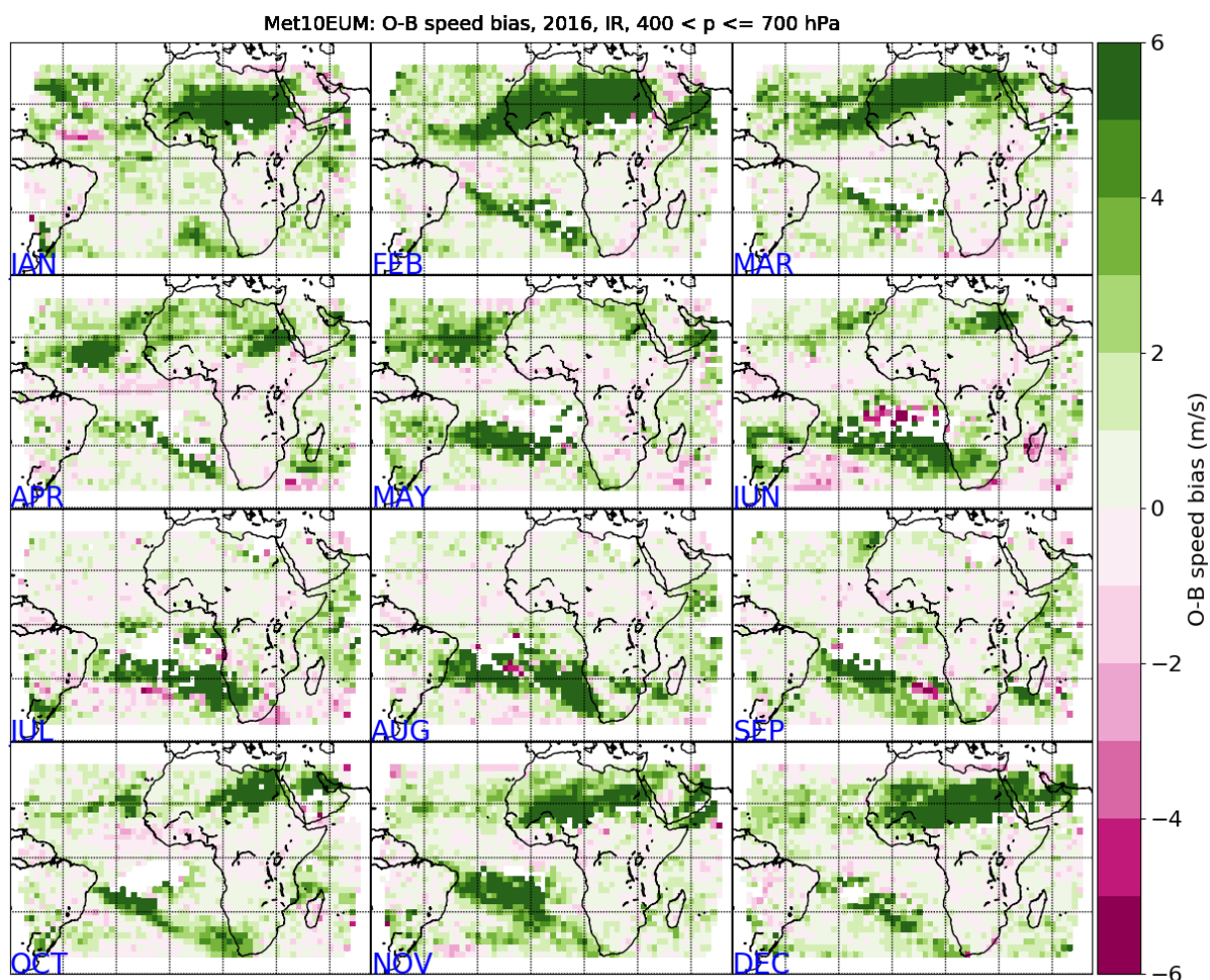


Figure 4.9 : As Figure 4.4, but for mid-level winds (400 hPa < p ≤ 700 hPa).

Figure 4.10 shows that mean differences between pressures assigned to AMV and the best-fit pressure are > 100 hPa over regions of exhibiting high wind speed discrepancies. Thus, AMVs are assigned to too low in the atmosphere and in conjunction with vertical wind shear lead to observed positive O-B speed bias greater than 6 ms⁻¹ at these locations.

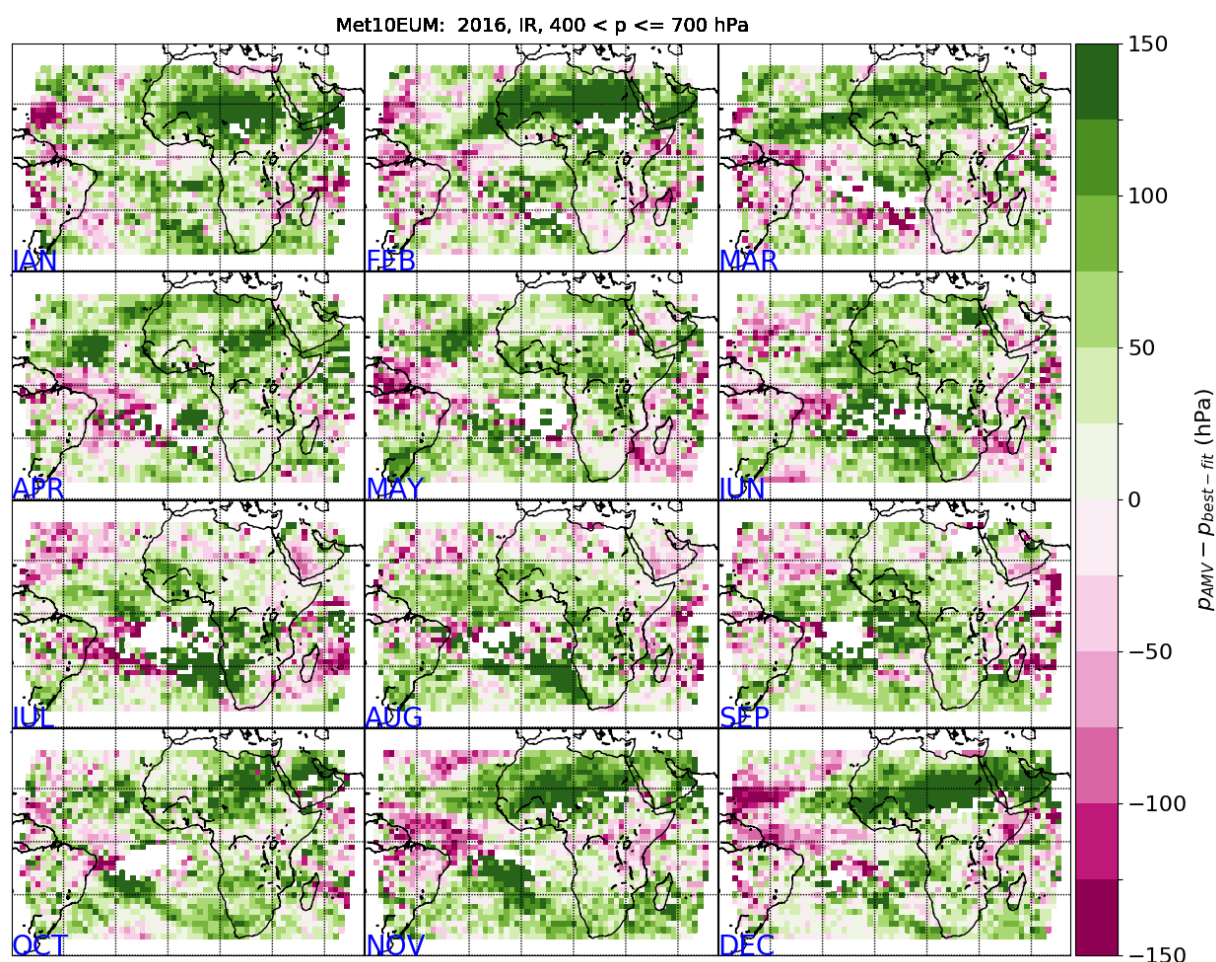


Figure 4.10 : Pressure assigned to Met10EUM AMV (p_{AMV}) vs collocated best-fit pressure ($p_{best-fit}$). As Fig. 4 but differences $p_{AMV} - p_{best-fit}$ are averaged for mid-level winds ($400 \text{ hPa} < p \leq 700 \text{ hPa}$).

Mean wind speed differences between Met10EUM and ECMWF as function of local daytime for mid-level winds are displayed in Figure 4.11. Similar to high-level winds, no clear dependency of the bias on local daytime is apparent for any zonal band. Diurnal variations in speed bias are $< 1 \text{ ms}^{-1}$.

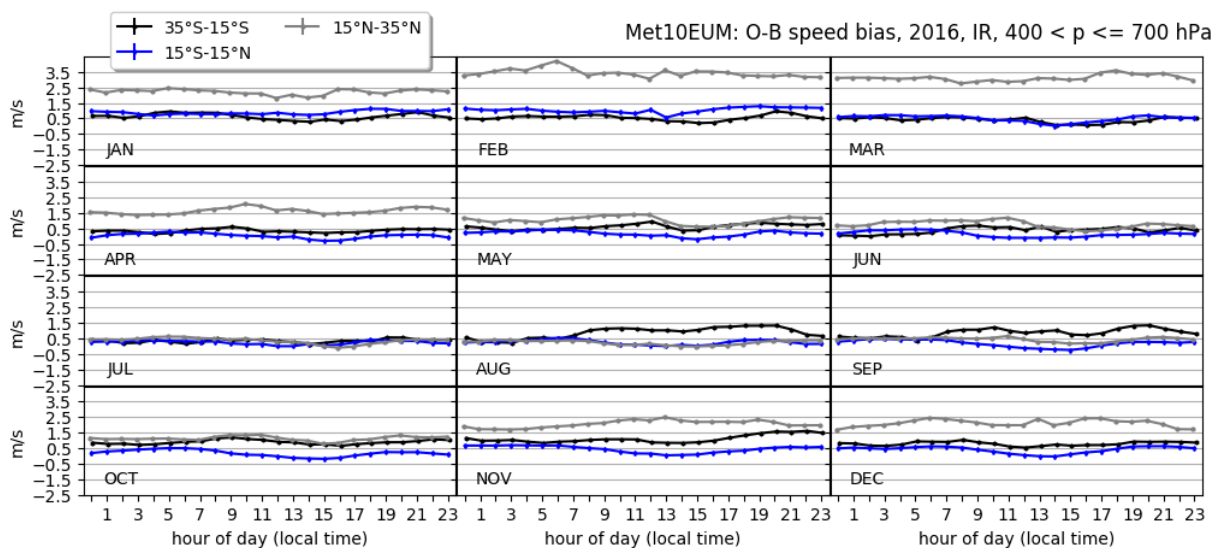


Figure 4.11 : Diurnal cycle of Met10EUM O-B speed bias for three zonal bands (35°S-15°S, 15°S-15°N, 15°N-35°S) and mid-level winds.

Low-level winds: The spatial distribution of monthly mean wind speed differences between low-level AMV Met10EUM and ECWMF is given in Figure 4.12. Wind speed differences are mostly $\leq 1 \text{ ms}^{-1}$, except for some arid locations in Northern Africa, where larger positive speed biases were found. Comparison to best-fit pressure reveals that AMVs are mostly assigned too low in the atmosphere (Figure 4.13). As the impact of the height assignment errors appears small, we can conclude that wind speed and vertical wind shear were small at these altitudes.

Similar to high- and mid-level winds, the correlation between speed bias and diurnal cycle of convection was analysed (Fig. 13). As for high- and mid-level winds, variations of the speed bias during the day is small for the different zonal bands.

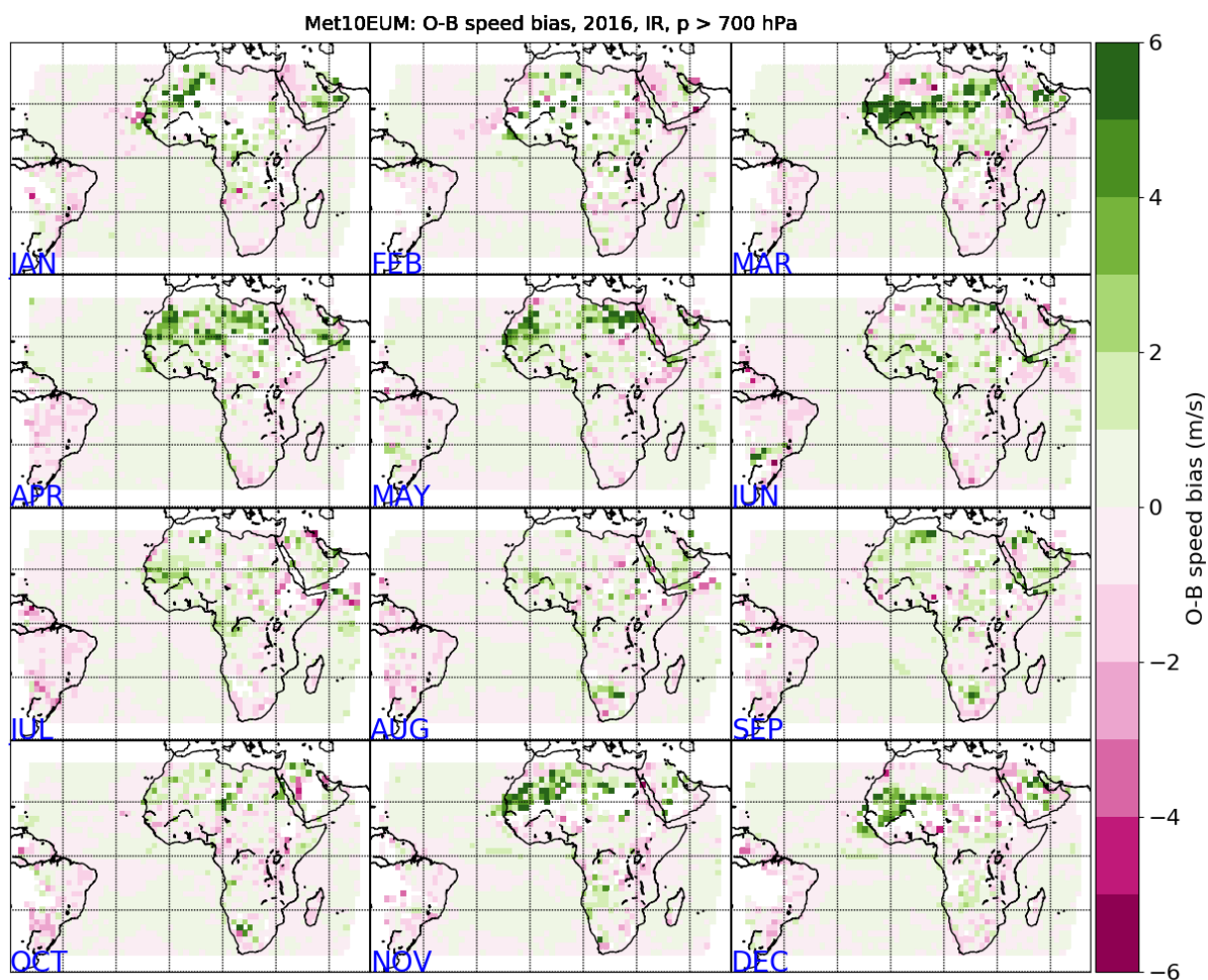


Figure 4.12 : As Figure 4.4, but for low-level winds ($p > 700$ hPa).

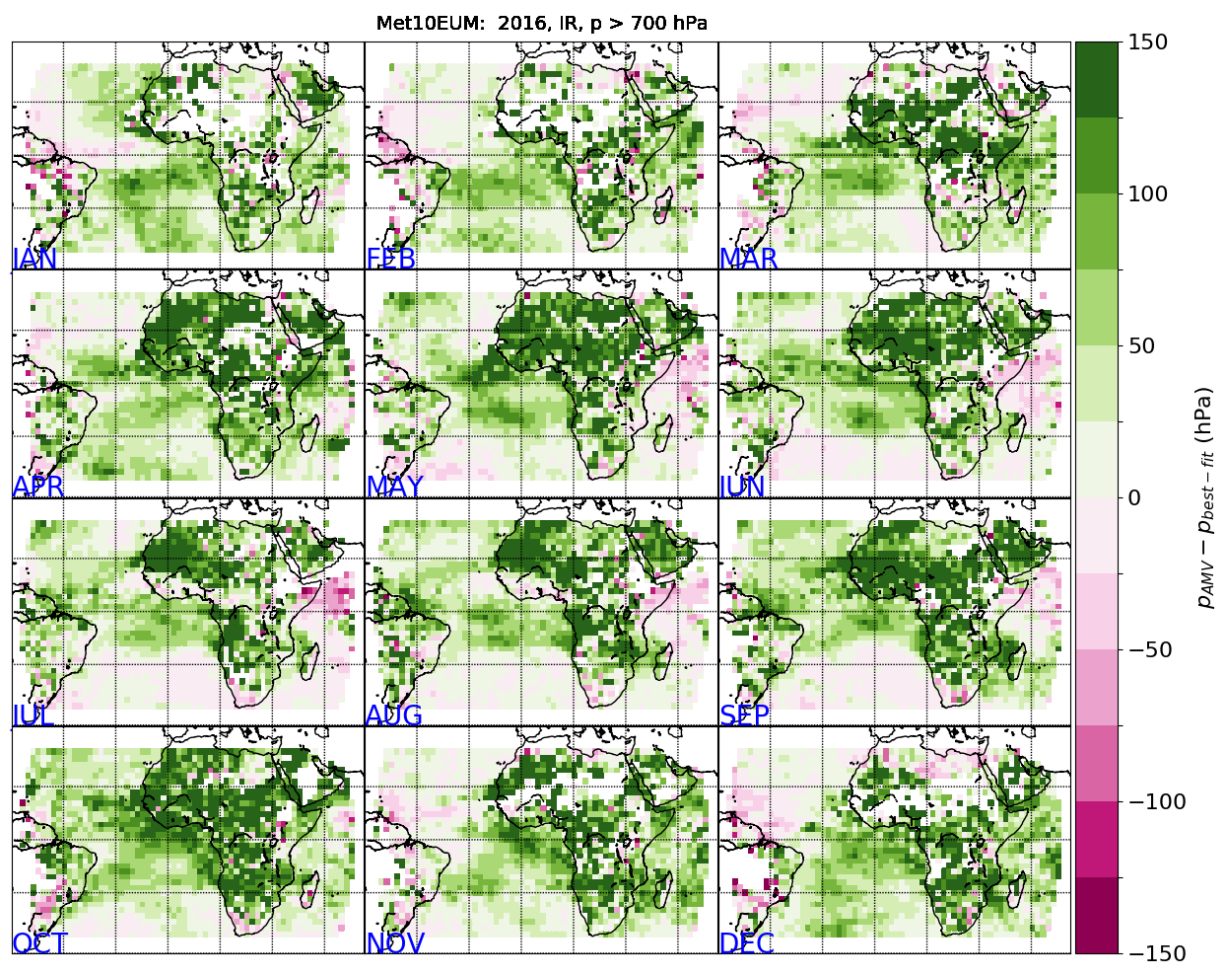


Figure 4.13 : Pressure assigned to Met10EUM AMV (p_{AMV}) vs collocated best-fit pressure ($p_{best-fit}$). As Figure 4.5, but differences $p_{AMV} - p_{best-fit}$ are averaged for mid-level winds ($p > 700$ hPa).

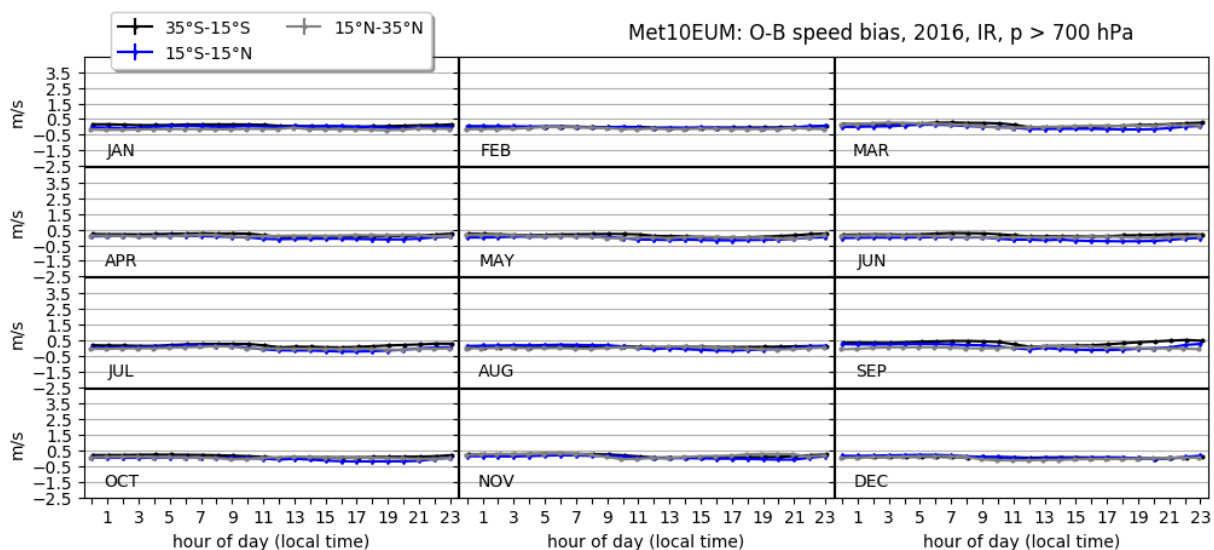


Figure 4.14 : Diurnal cycle of Met10EUM's O-B speed bias for three zonal bands (35°S-15°S, 15°S-15°N, 15°N-35°S) and low-level winds.

4.2.2 AMVs from Metop IR imagery

Vertical profiles of wind speed differences: Vertical profiles of the O-B speed bias for different latitude bands are given in Figure 4.15 for different seasons. For low-level clouds found up to 800 hPa ($p > 800$ hPa), differences in wind speed are close to 0 ms^{-1} , similar to the value reported by the Met10EUM vs ECMWF comparison at these levels (see Section 4.2.1). However, above 800 hPa, depending on latitudes, the O-B speed biases increase with altitude, whereby the sign of the bias depends on zonal band and season.

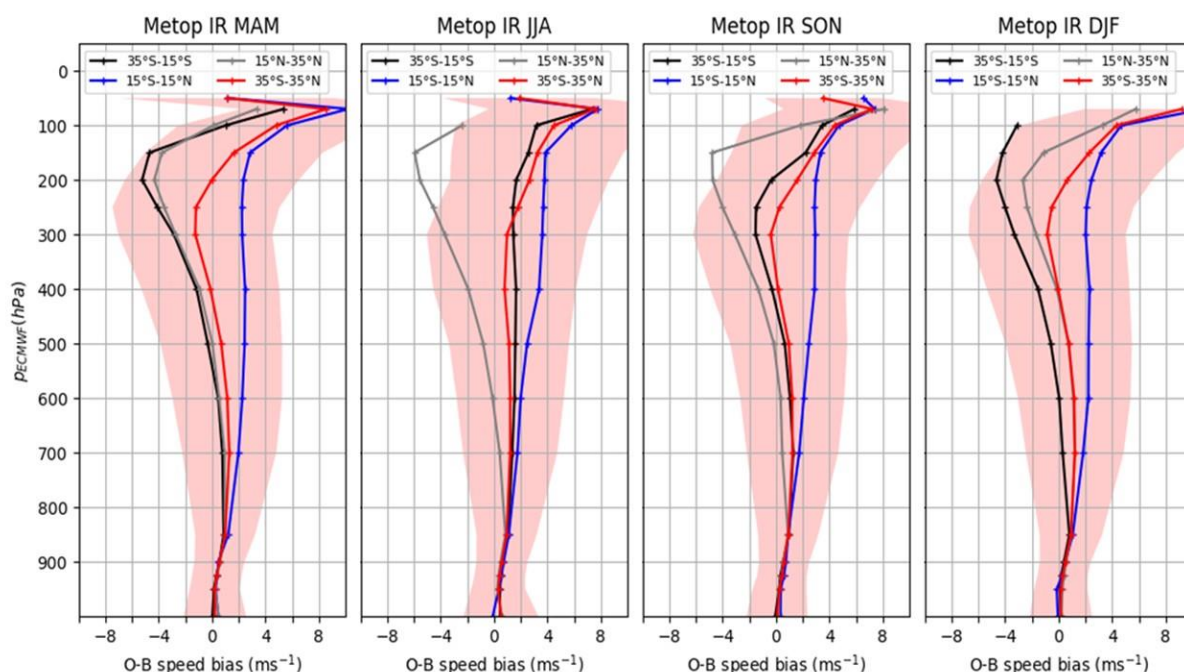



Figure 4.15 : As Figure 4.1 but for Dual-Metop AMVs.

High-level winds: The geographic distribution of Metop AMV wind speed against collocated ECMWF wind speeds is given in Figure 4.16. Metop mostly reports higher wind speeds than ECMWF in the equator regions, where the average wind speed is typically below $< 20 \text{ ms}^{-1}$ (Figure 4.17). This positive O-B speed bias turns negative towards mid-latitudes, where wind speeds are higher.

The $p \leq \pm 25 \text{ hPa}$ vertical collocation criteria is relaxed to investigate height-assignment differences between ECMWF and Metop. Comparison of the spatial distribution of the speed bias (Fig. 14) to the spatial distribution of the best-fit pressure statistics (Figure 4.18) shows that over equatorial regions of South- and Central America and over Pacific regions, $p_{\text{best-fit}}$ is mostly larger than p_{AMV} . Too high altitudes assigned to AMVs would lead to negative O-B speed biases, which, however, was not observed. For AMVs derived over the northern Indian Ocean in May to September, p_{AMV} are larger than $p_{\text{best-fit}}$, which may explain parts of the observed positive speed bias over these regions. For regions polewards of the equator, differences $p_{\text{AMV}} - p_{\text{best-fit}}$ are typically smaller than 50 hPa and tend to be negative, indicating that AMVs are assigned too high altitudes.

	<p align="center">Study of AMV speed biases in the tropics</p> <p align="center">Final Report</p>	
Reference: AMV-TN-0008-TS_Ed1_Rev3	Date : 18/06/2020	Page : 38/118

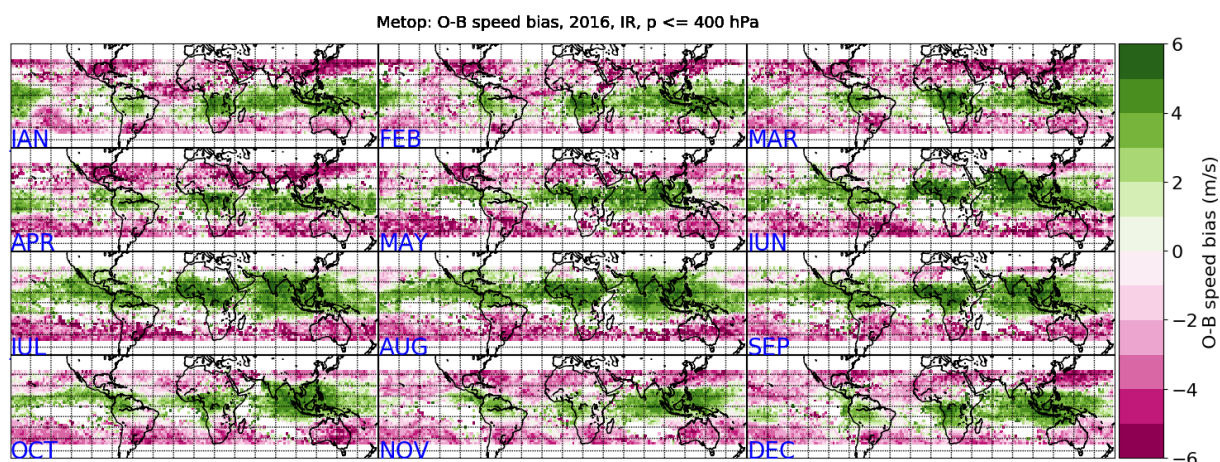


Figure 4.16 : Geographic distribution of tropical Metop wind speed against collocated ECMWF winds. O-B speed bias is averaged for high levels ($p \leq 400$ hPa) and over a $2^\circ \times 2^\circ$ latitude x longitude grid.

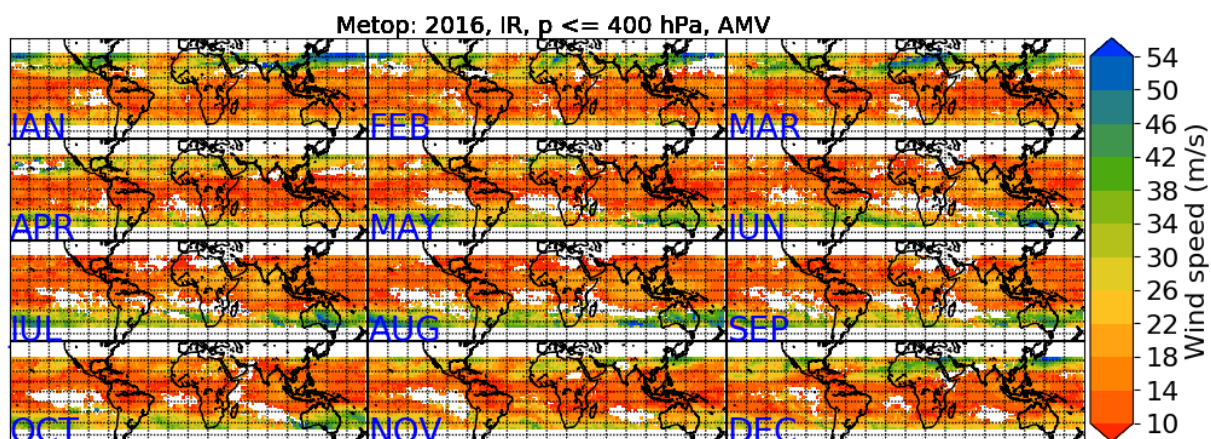



Figure 4.17 : Geographic distribution of tropical Metop wind speeds averaged for high levels ($p \leq 400$ hPa) and over a $2^\circ \times 2^\circ$ latitude x longitude grid. Collocation criteria as described in Sec. 4.1 are used.

	<p align="center">Study of AMV speed biases in the tropics</p> <p align="center">Final Report</p>	
Reference: AMV-TN-0008-TS_Ed1_Rev3	Date : 18/06/2020	Page : 39/118

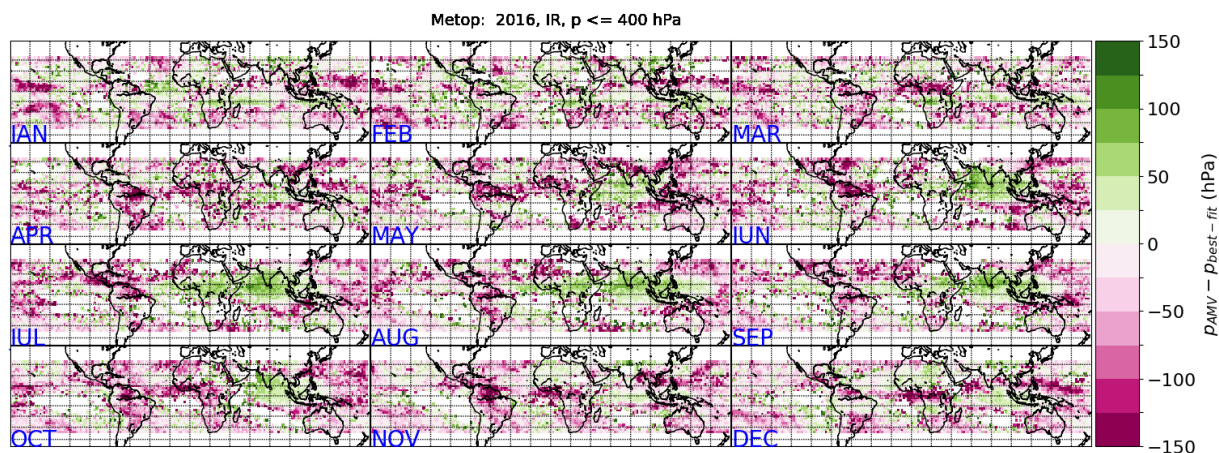


Figure 4.18 : Pressure assigned to Metop AMV (p_{AMV}) vs collocated best-fit pressure ($p_{best-fit}$). Differences $p_{AMV} - p_{best-fit}$ are averaged for high levels ($p \leq 400$ hPa) and over a $2^\circ \times 2^\circ$ lat x lon grid.

Mid-level winds: Geographic distribution of the mean wind speed differences Metop-ECWMF are shown in Figure 4.19. Their spatial structure resembles that of high-level winds, that is, Metop report larger wind speeds than ECWMF for equatorial regions and tends to reports smaller wind speeds than ECWMF for latitudes that connect northern and southern to the equatorial region. The amplitude of reported mean differences is smaller than that reported for high-level winds, likely due to much smaller wind speeds at these altitudes (Figure 4.20). Comparison of AMV pressure to best-fit pressure is given in Figure 4.21. $p_{AMV} - p_{best-fit}$ is largest around the equator, with p_{AMV} being regularly 150 hPa larger than $p_{best-fit}$. Negative values of $p_{AMV} - p_{best-fit}$ are mostly found over the Pacific.

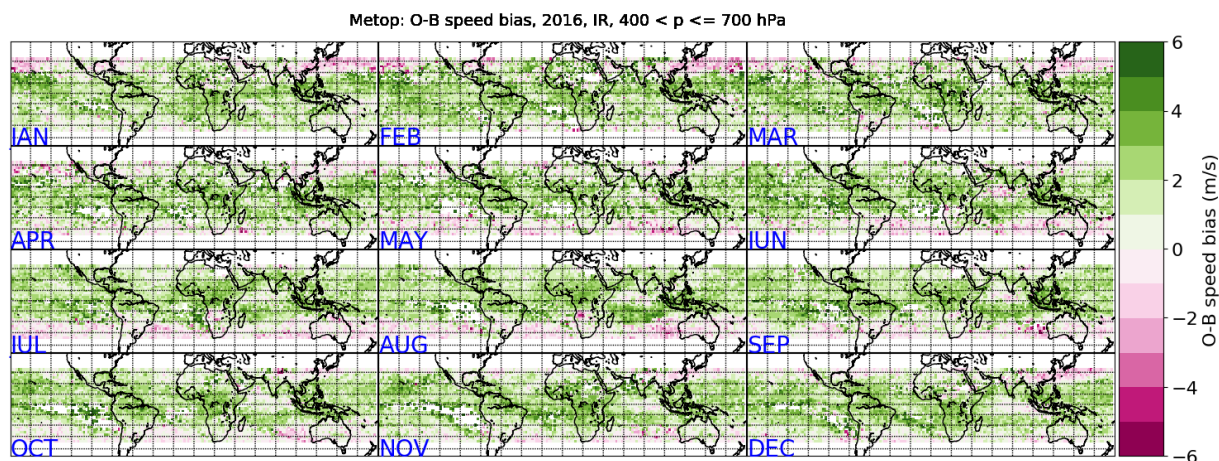


Figure 4.19 : Geographic distribution of Metop wind speed against collocated ECMWF winds. O-B bias is averaged for mid-levels ($400 \text{ hPa} < p \leq 700 \text{ hPa}$) and over a $2^\circ \times 2^\circ$ latitude x longitude grid.

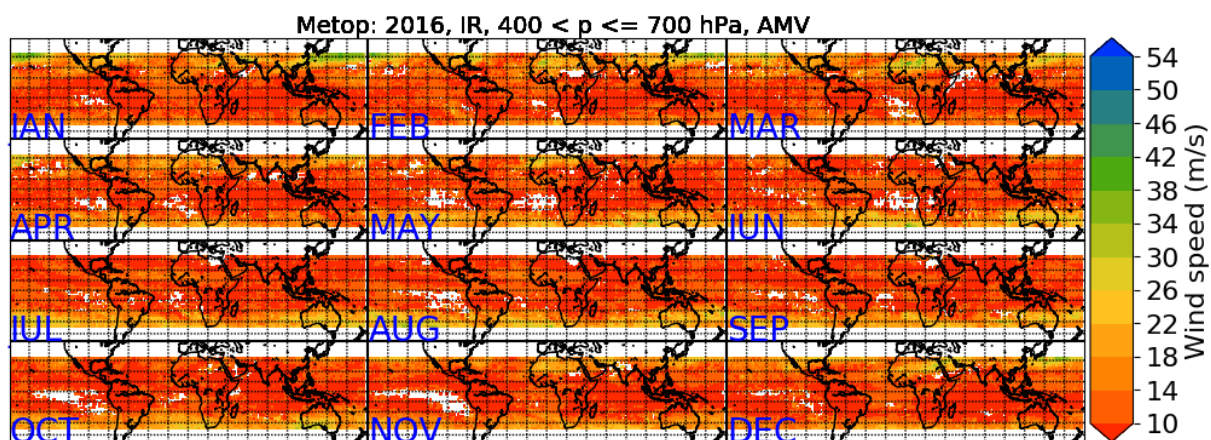


Figure 4.20 : Geographic distribution of tropical Metop wind speeds averaged for mid levels ($400 \text{ hPa} < p \leq 700 \text{ hPa}$) and over a $2^\circ \times 2^\circ$ latitude x longitude grid. Collocation criteria as described in Sec. 4.1 are used.

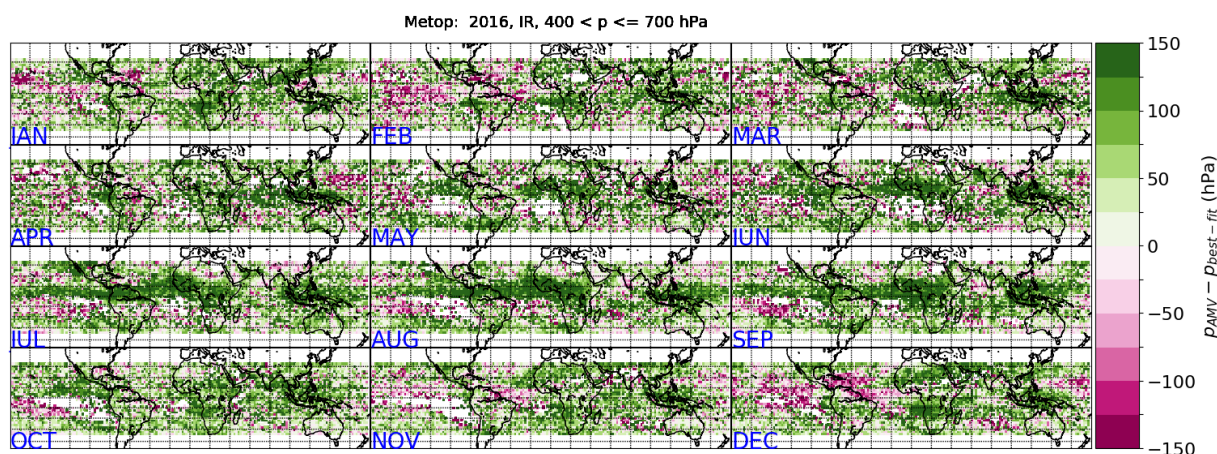



Figure 4.21 : Pressure assigned to Metop AMV (p_{AMV}) vs collocated best-fit pressure ($p_{\text{best-fit}}$). Differences $p_{\text{AMV}} - p_{\text{best-fit}}$ are averaged for mid-levels ($400 \text{ hPa} < p \leq 700 \text{ hPa}$) and over a $2^\circ \times 2^\circ$ latitude x longitude grid.

Low-level winds: The O-B speed bias is mostly $< 1 \text{ ms}^{-1}$ for low-level winds. Over the African continent, regions of large O-B speed bias, up to -4 ms^{-1} were obtained, e.g., from Senegal to Central Africa in Northern Hemisphere Winter (DJF), or over Southern Africa in August and September (Figure 4.22).

	<p align="center">Study of AMV speed biases in the tropics</p> <p align="center">Final Report</p>	
Reference: AMV-TN-0008-TS_Ed1_Rev3	Date : 18/06/2020	Page : 41/118

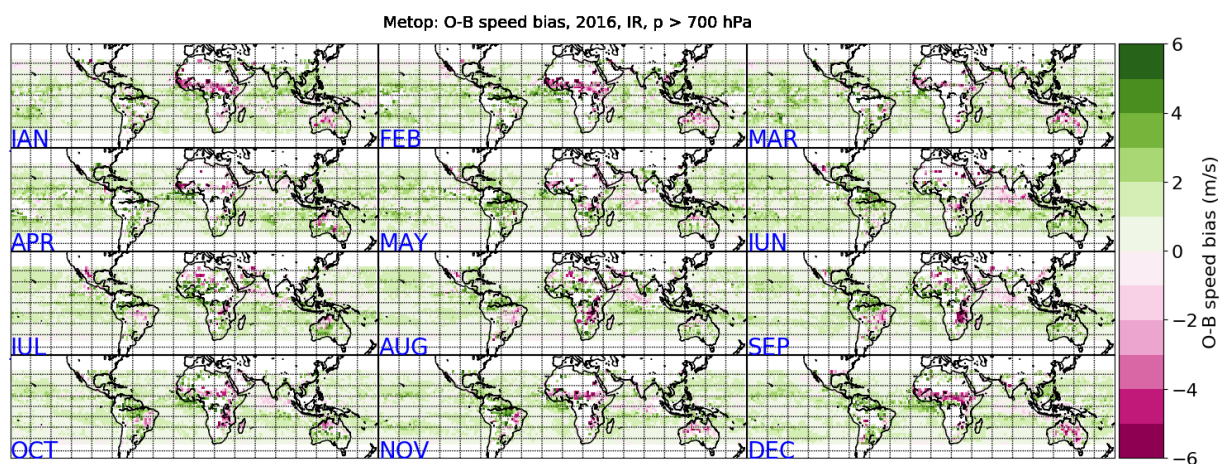



Figure 4.22 : Geographic distribution of tropical Metop wind speed against collocated ECMWF winds. O-B bias is averaged for low levels ($p > 700$ hPa) and over a $2^\circ \times 2^\circ$ latitude x longitude grid.

	<p align="center">Study of AMV speed biases in the tropics</p> <p align="center">Final Report</p>	
Reference: AMV-TN-0008-TS_Ed1_Rev3	Date : 18/06/2020	Page : 42/118

5 COMPARISON OF AMVS TO REFERENCE OBSERVATIONS


5.1 MISR STEREO AMVS

For comparison of Met10EUM and Metop AMVs to MISR stereo AMVs, the same collocation criteria as for the comparison to ECMWF winds are used. However, a horizontal collocation criteria needs to be introduced, i.e. MISR AMVs are compared to AMVs if data are within a horizontal distance of 150 km. If several AMV data meet the collocation criteria, the median is calculated and compared to the corresponding MISR wind. MISR AMV retrieval is independent of a priori atmospheric and humidity forecasts and retrieves cloud height and motion simultaneously (Horvath and Davies, 2001). MISR provides wind speed and direction at geometric heights, which are converted to pressure levels using geopotential heights of the spatially and temporally closest ECMWF grid cell. Note the same ECMWF dataset is used for altitude to pressure conversion as for wind comparison of Sec. 4.

Profiles of the mean differences between Met10EUM AMV and MISR wind speeds are given in Figure 5.1 for each month in 2016. For low-level to mid-level winds, MISR winds tends to be less than 1 ms^{-1} faster than Met10EUM AMVs. A higher bias was obtained for high-level winds up to 200 hPa, mainly in the range of 1 ms^{-1} . Larger mean differences are obtained for July to September at these altitudes. It is important to note here, that we have compared winds from IR imagery (Met10EUM) to winds derived from VIS imagery (MISR) in order to compare results from Met10EUM to that of Metop. Consequently, parts of the discrepancies may be explained by the fact that both sensors do not see the same cloud, which is particularly true for semi-transparent clouds.

Monthly mean profiles for Metop AMVs vs MISR wind speeds are given in Figure 5.2. MISR and Metop AMVS typically agree within 0.5 ms^{-1} at low- to mid-levels ($p \geq 400 \text{ hPa}$). In contrast to Met10EUM, Metop winds are, however, faster than MISR winds at these altitudes. Between 200 and 400 hPa, Metop winds are $0.5\text{-}2 \text{ ms}^{-1}$ faster than MISR winds. Above this altitude ($p < 200 \text{ hPa}$), wind speeds differences are typically larger. As for Met10EUM, obtained wind speed differences may be partly explained by different channels used by Metop and MISR.

The geographic distribution of the mean Metop-MISR wind speed differences for high-level winds is given in Figure 5.3. Positive Metop-MISR wind speed differences larger than 2 ms^{-1} are frequently found over South-Eastern Asia and thus in a region where large mean Metop-ECMWF mean wind speed difference are found. Over southern oceans, Metop-MISR wind speed differences tend to be negative.

	<p align="center">Study of AMV speed biases in the tropics</p> <p align="center">Final Report</p>	
Reference: AMV-TN-0008-TS_Ed1_Rev3	Date : 18/06/2020	Page : 43/118

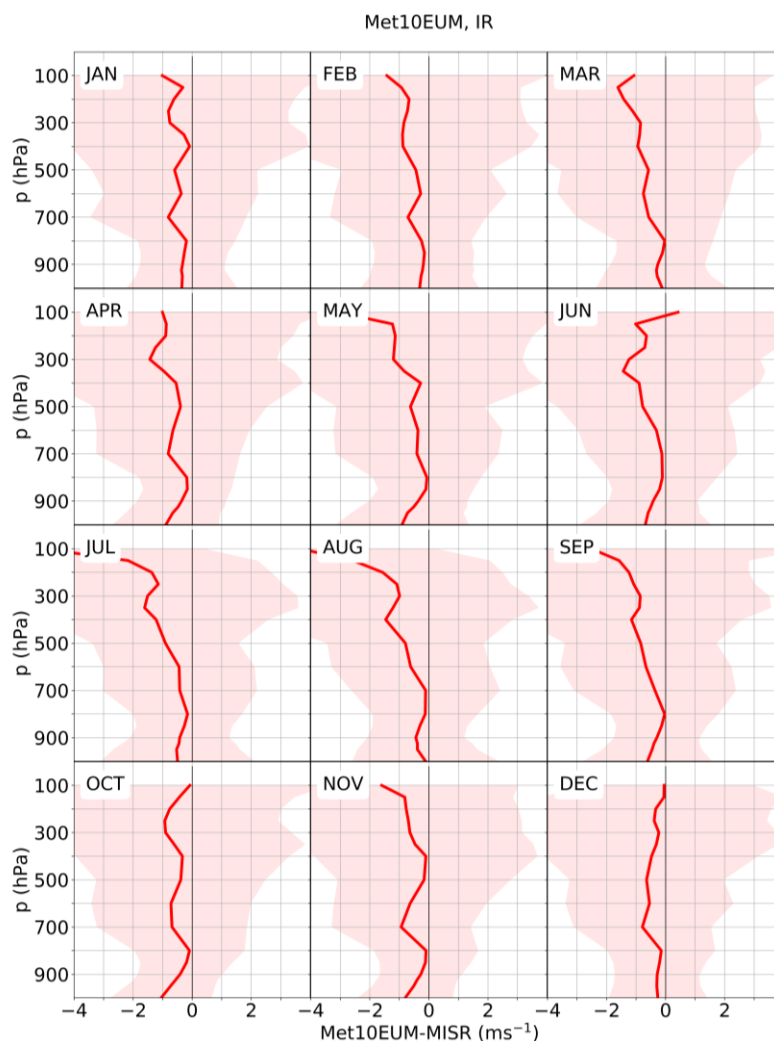



Figure 5.1 : Monthly profiles of mean differences between Met10EUM AMV and MISR wind speeds (red line) and corresponding standard deviation (light red shades).

	<p align="center">Study of AMV speed biases in the tropics</p> <p align="center">Final Report</p>	
Reference: AMV-TN-0008-TS_Ed1_Rev3	Date : 18/06/2020	Page : 44/118

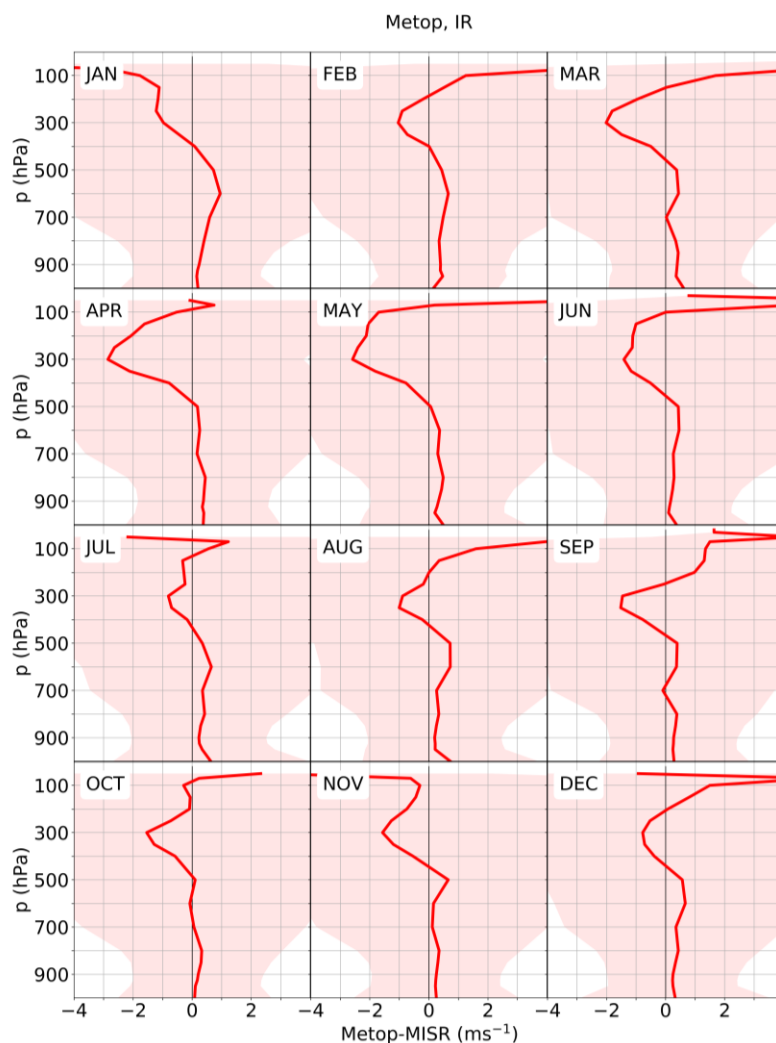


Figure 5.2 : Monthly profiles of mean differences between Metop AMV and MISR wind speeds (red line) and corresponding standard deviation (light red shades).

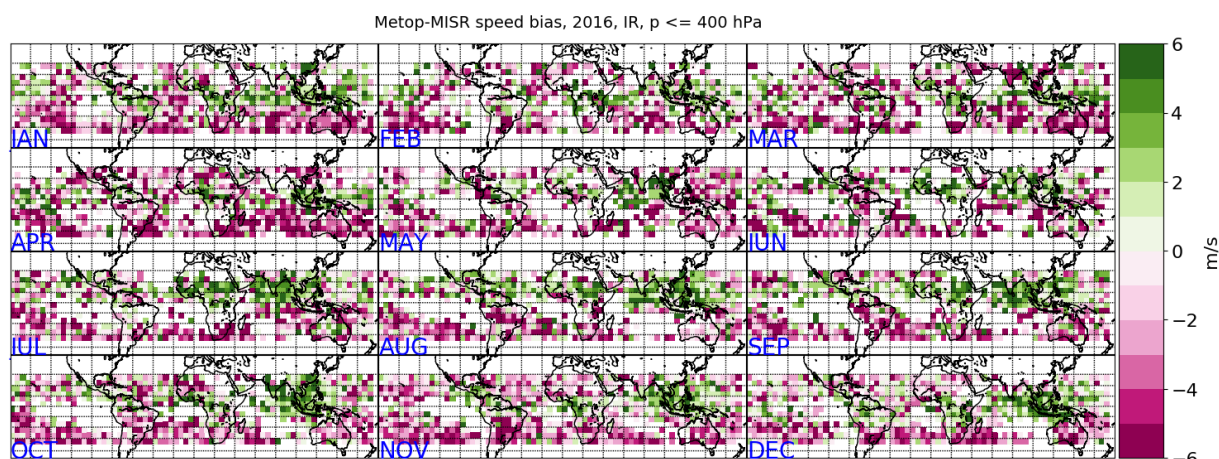


Figure 5.3 : Geographic distribution of tropical Metop wind speeds against MISR winds averaged for high levels ($p \leq 400$ hPa) and over a $5^\circ \times 5^\circ$ latitude x longitude grid. Collocation criteria as described in Sec. 5.1 are used.


5.2 RAOB IGRA WINDS

There are 2050 radiosondes observations (RAOB) available from IGRA in 2016 for latitudes $\leq \pm 35^\circ$. Table 5.1 provides an overview of RAOB data availability for different tropical regions. Most of the RAOB were from ships located in Western Pacific, while no RAOB data were available over the Indian ocean. The collocation criteria introduced in in Sec. 5.1 were used to collocate RAOB with Met10EUM and Metop AMV, respectively. However, only matches with Metop were possible. Metop-RAOB matches were distributed irregularly over time. We only got matches in January, February, March, August and December, whereby only 1 match was available in January and only 7 matches in March. Due to this inhomogeneity, we did not attempt at grouping Metop-RAOB wind speed differences into months or different zonal bands.

Table 5.1 : Overview RAOB data availability in tropics (latitudes $\leq \pm 35^\circ$) for 2016. Number of radiosondes are grouped into Western Pacific ($90^\circ\text{E} < \text{longitude} \leq 150^\circ\text{E}$), Indian Ocean ($45^\circ\text{E} < \text{longitude} \leq 90^\circ\text{E}$) and Africa ($-50^\circ\text{E} < \text{longitude} \leq 45^\circ\text{E}$).

Western Pacific	Indian Ocean	Africa	Other	Total
865	0	588	597	2050

Figure 5.4 shows mean wind speed differences between Metop and RAOB as function of atmospheric pressure. In the lowermost troposphere ($p \geq 900$ hPa) RAOB winds are 2 ms^{-1} faster than Metop. Above this altitude to about 600 hPa, Metop winds are faster than RAOB, up to 5 ms^{-1} . At 550 hPa, the differences change again sign, with RAOB reporting faster winds than Metop. This spread between Metop-RAOB mean wind speed differences then typically increases with increasing altitude. Note, a similar change of mean Metop-RAOB wind speed differences with altitude was also found by Horvath et al. (2017; their Fig. 5b), although they report smaller differences of $< 2 \text{ ms}^{-1}$.

	<p align="center">Study of AMV speed biases in the tropics</p> <p align="center">Final Report</p>	
Reference: AMV-TN-0008-TS_Ed1_Rev3	Date : 18/06/2020	Page : 46/118

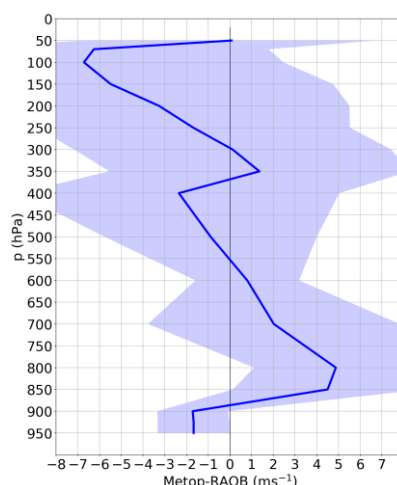



Figure 5.4 : Profile of mean Metop-RAOB wind speed differences (blue) and corresponding standard deviation (blue shaded area). RAOB were collocated with Metop using criteria introduced in Sec. 3.

5.3 CALIPSO/CALIOP CLOUD TOP HEIGHTS

Lidar cloud-top height observations provided by CALIOP (Cloud-Aerosol Lidar with Orthogonal Polarization) instrument aboard the polar-orbiting CALIPSO (Cloud-Aerosol Lidar and Infrared Pathfinder Satellite Observations) satellite are used to check the heights assigned to Met10EUM AMVs and investigate possible correlations between O-B speed bias and CALIPSO-AMV height differences. Initially, it was planned to compare CALIPSO cloud top heights also to Metop. However, no data met the collocation requirements described below. Additionally, no CALIPSO data were available for February 2016.

The applied collocation requirements have originally been developed by Folger and Weissmann (2014) and Weissmann et al. (2013) and were only slightly modified for this task. Firstly, CALIPSO data are collocated with nearby AMVs if they are within a horizontal distance of 75 km and within 45 minutes of the location and time of each AMV. Secondly, the median value of all available (at least 20) individual CALIPSO cloud-top observations meeting the collocation criteria is taken and considered as representative cloud top. In addition, the root-mean-square differences between single lidar cloud observations and their median value must not exceed 100 hPa. We discarded all multilayer cloud observations and ensured that the detected lidar signal definitely represents a cloud. For the latter, this can be ensured by forcing the CALIPSO QI to exceed a value of 90. Finally, the AMVs must be within 165 hPa of the CALIPSO cloud top height.

Figure 5.5 reports the comparison of CALIPSO cloud top heights (p_{CALIPSO}) with Met10EUM AMV pressures (p_{AMV}). Only data are used where AMVs are collocated with ECMWF wind fields. Most collocations are found for 300, 400, 800 and 900 hPa levels. Overall, Δp , the median difference between collocated p_{AMV} and p_{CALIPSO} , is > 0 hPa throughout the atmospheric profile (except for 700 hPa, where Δp is typically < 0), which in turn means that AMVs tend to have assigned too low altitudes. Highest median pressure difference of 25 - 50 hPa are typically obtained between 300 and 400 hPa altitude and at 600 hPa altitude. At the 400 hPa layer, this peak in Δp often coincides with largest O-B speed bias of up to 2 ms^{-1} (e.g. January, March, October, November). For these periods, highest wind speed is typically found around 300 hPa. As AMVs around 400 hPa have assigned too low altitudes, parts of the O-B speed bias obtained at these altitudes may can be attributed to an average 30 hPa incorrect height

	<h2 style="text-align: center;">Study of AMV speed biases in the tropics</h2> <h3 style="text-align: center;">Final Report</h3>	
Reference: AMV-TN-0008-TS_Ed1_Rev3	Date : 18/06/2020	Page : 47/118

assignment in conjunction with high wind speeds above 400 hPa. Interestingly, despite positive median values of p, O-B speed biases above 400 hPa (p<400 hPa) tend to be negative, i.e. ECMWF winds are faster than Met10EUM AMVs for the presented data.

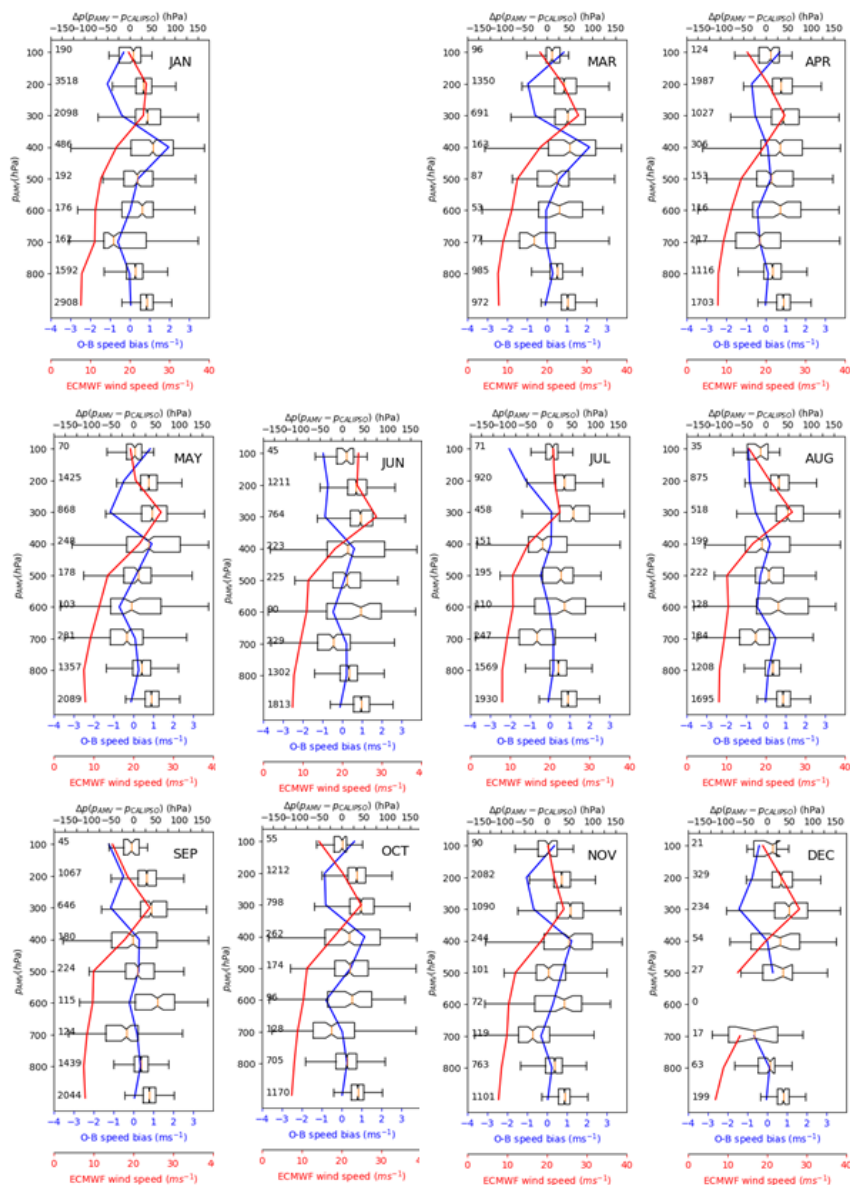



Figure 5.5 : Comparison of CALIPSO cloud top height with available Met10EUM AMVs. (Black) Box-and-whisker plots of AMV-CALIPSO pressure ($p_{AMV}-p_{CALIPSO}$) difference are shown for different AMV pressure levels, whereby each box contains data in a pressure range of 50 hPa. Each box extends from the lower to upper quartile values of the pressure differences, with a red line at the median. Corresponding O-B speed bias is shown in blue, while corresponding ECMWF speeds are shown in red. Numbers in the left part of each figure denote the number of collocations used to calculate pressure differences. No CALIPSO data were available for February 2016.

	<p align="center">Study of AMV speed biases in the tropics</p> <p align="center">Final Report</p>	
Reference: AMV-TN-0008-TS_Ed1_Rev3	Date : 18/06/2020	Page : 48/118

5.4 CLOUDSAT/CPR CLOUD TYPE CLASSIFICATION

Cloud type classification obtained by the vertically profiling Cloud Profiling Radar (CPR) aboard the CLOUDSAT satellite are used to investigate any correlation between cloud type and observed O-B speed bias. More precisely, the 2B-CLDCLASS product is used. It classifies clouds into either stratus (St), stratus (Sc), cumulus (Cu, including cumulus congestus), nimbostratus (Ns), altocumulus (Ac), altostratus (As), deep convective (cumulonimbus), or high (cirrus and cirrostratus) clouds. This classification based on different rules for hydrometeor vertical and horizontal scales, the maximum equivalent reflectivity measured by the CPR, indications of precipitation, and ancillary data including ECMWF predicted temperature profiles and surface topography height (see Sassen and Wang, 2008).

Based on the collocation database established in Sec. 4, we collocated any Met10EUM AMV with CLOUDSAT if horizontal, vertical and temporal distance are less than 150 km, less than 25 hPa and less than 30 minutes, respectively. In case several CLOUDSAT profiles meet the collocation criteria, we use the cloud top that is spatially closest to the Met10EUM AMV. CLOUDSAT cloud tops are reported on geometric heights. Similar to MISR stereo AMVs temperature and pressure from the spatially and temporally closest ECMWF grid cell are used to convert geometric heights to pressure.

Collocated O-B speed bias (Met10EUM AMV - ECMWF) as function of CLOUDSAT cloud type is given in Figure 5.6 for high-level, mid-level and low-level winds. At high-levels (Figure 5.6a), most collocated clouds are cirrus clouds, followed by Altostratus clouds, which is not surprising as they considered the best tracers for estimating AMVs because they show radiance gradients can be readily tracked and they are likely to be passive tracers of the flow at a single level (e.g., Nieman et al., 1993). As expected, no stratus or stratocumulus cloud have been identified or matched at these altitudes. The O-B speed bias is relative similar for cirrus and altostratus clouds and around -1.5 ms^{-1} (ECMWF faster than Met10EUM AMV), indicating no clear dependency of collocated speed bias and cloud type at these levels. Note, we separated results for different zonal bands (35°S - 15°S , 15°S - 15°N , 15°N - 35°N) but no significant change with respect to results presented in Fig. 27a were found (plots not shown).

At mid-level, most clouds that could be collocated with Met10EUM AMVs were identified as altocumulus, cumulus and stratocumulus clouds (Figure 5.6b). As for high levels, there is no clear correlation between cloud type and collocated O-B speed bias, which is on average $< 1.5 \text{ ms}^{-1}$ (ECMWF faster than Met10EUM AMV) for these three cloud types. As for high levels, results were separated for three different zonal bands but no significant change with respect to the results presented in Figure 5.6b were found.

At low levels, clouds are predominately of stratocumulus, while a small portion is classified as cumulus and altocumulus. For these three cloud types, collocated O-B speed bias is around $< 0 \text{ ms}^{-1}$.

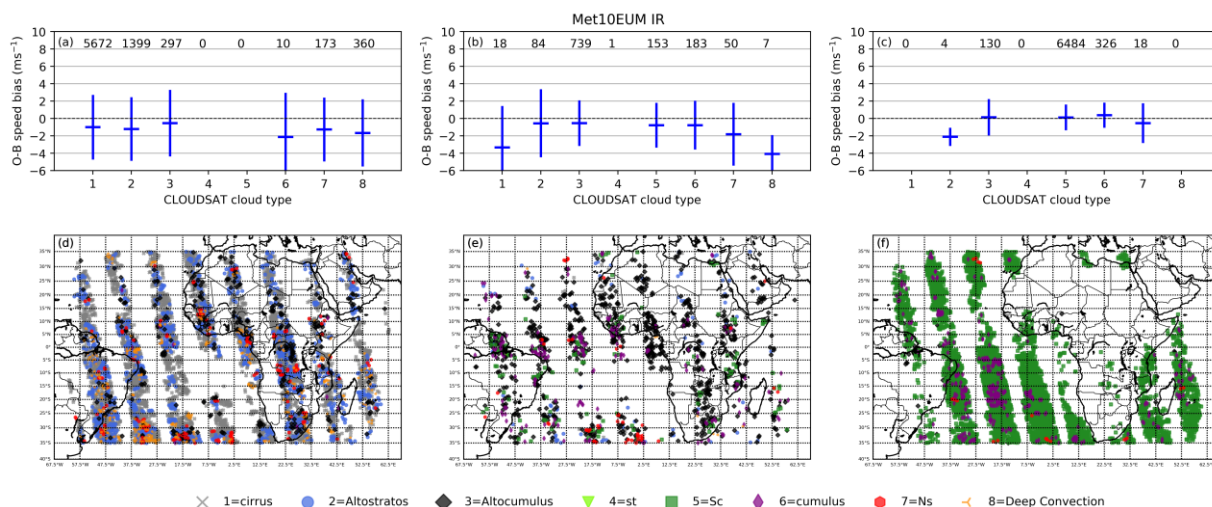



Figure 5.6 : Correlation of CLOUDSAT cloud types with observed O-B speed bias of Met10EUM AMVs against ECMWF winds for (a) high-level clouds, (b) mid-level and (c) low-level clouds. Horizontal blue lines denote mean wind speed differences Met10EUM AMV - ECMWF, while vertical blue lines denote the corresponding standard deviation. CLOUDSAT groups clouds into cirrus (1), altostratus (2), altocumulus (3), stratus (4), stratocumulus (5), cumulus (6, including cumulus congestus), nimbostratus (7) and deep convection (8). Depicted are also geographical distribution of CLOUDSAT and Met10EUM AMV collocations for (d) high-level clouds, (e) mid-level and (f) low-level clouds. Results for 8 months averages are presented (January to August).

5.5 OUTGOING LONG-WAVE RADIATION (OLR)

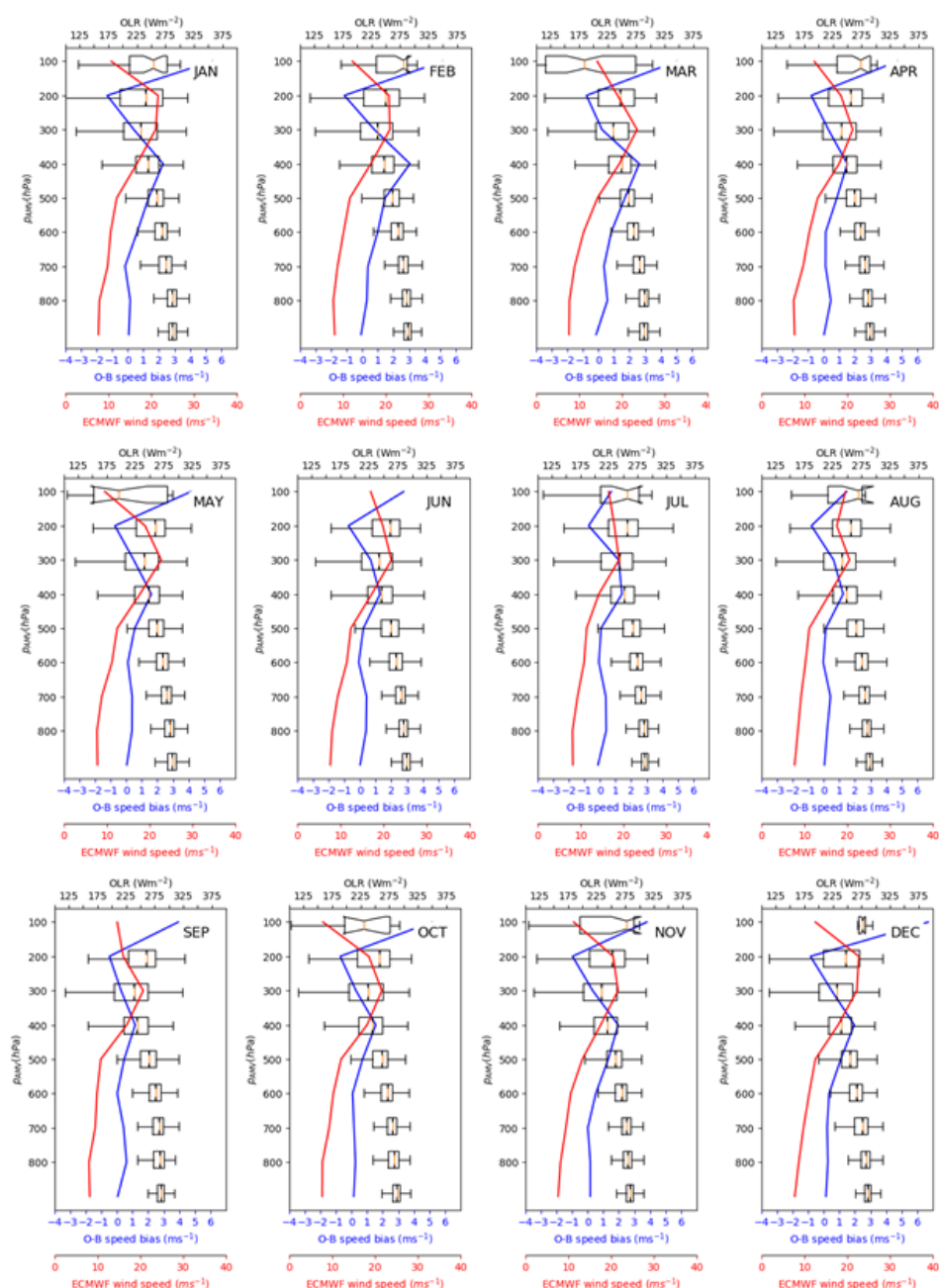
5.5.1 Accumulated OLR from ECMWF

It is aimed to relate O-B speed bias to convective regimes to check whether the strength of convection lead to weak/large O-B speed biases. OLR is commonly used to describe the general structure and depth of tropical convection. For instance, convective regions covered by cold tops typically appear as OLR minima ($OLR < 260 \text{ Wm}^{-2}$). In this Section OLR from ECWMF are used to check the correlation between OLR and speed bias. At ECMWF, radiation parameters at single levels are so-called accumulated parameters, that is, the data is accumulated over certain time period. The unit of the concerned products is Joule per square metre. Conversion to Wm^{-2} requires the accumulated values to be divided by the time period over which the data has been accumulated. For example, for a forecast step of 4 hours, the OLR in Wm^{-2} is calculated from the OLR in Jm^{-2} divided by 4×3600 seconds. As we do not want to compare OLRs accumulated over different time steps, one time step is selected for the comparison.

Figure 5.7 compares ECMWF's OLR from forecast step 1 (that is, for 1 and 13 UTC) to the O-B speed bias obtained in Sec. 4. For all months, the OLR profile is very similar. OLR decreases with altitude as the blocking of long-wave radiation penetrating through clouds and cloud albedo increases with altitude. Above 600 hPa ($p < 600 \text{ hPa}$), the medians of OLR are typically below 260 Wm^{-2} . The vertical profile of collocated O-B speed bias does not follow the vertical profile of OLR, indicating low correlation between convection strength and O-B speed bias.

	<p align="center">Study of AMV speed biases in the tropics</p> <p align="center">Final Report</p>	
Reference: AMV-TN-0008-TS_Ed1_Rev3	Date : 18/06/2020	Page : 50/118

Results for Metop-ECMWF speed differences vs OLR are given in Figure 5.8. Compared to Met10EUM, collocated OLR decreases stronger with altitude. In addition, OLR values are 20 - 50 Wm^{-2} lower than those obtained for Met10EUM above 400 hPa ($p < 400$ hPa), indicating that Metop is sensing in stronger convective regimes than Met10EUM at these altitudes. OLR minima above 200 hPa ($p < 200$ hPa) coincide with maxima in O-B speed biases of $> 2 \text{ ms}^{-1}$. As for Met10EUM, the vertical profile of collocated O-B speed bias does not follow the vertical profile of OLR, indicating low correlation between convection strength and O-B speed bias.




	<p style="text-align: center;">Study of AMV speed biases in the tropics</p> <p style="text-align: center;">Final Report</p>	
Reference: AMV-TN-0008-TS_Ed1_Rev3	Date : 18/06/2020	Page : 51/118

Figure 5.7 : Comparison of ECMWF OLR (step range = 1, see text) with Met10EUM AMVs. Box-and-whisker plots of OLR are shown for different AMV pressure levels. Each box extends from the lower to upper quartile values of the pressure differences, with a line at the median. Corresponding O-B speed bias is shown in blue, while ECMWF speeds are shown in red.

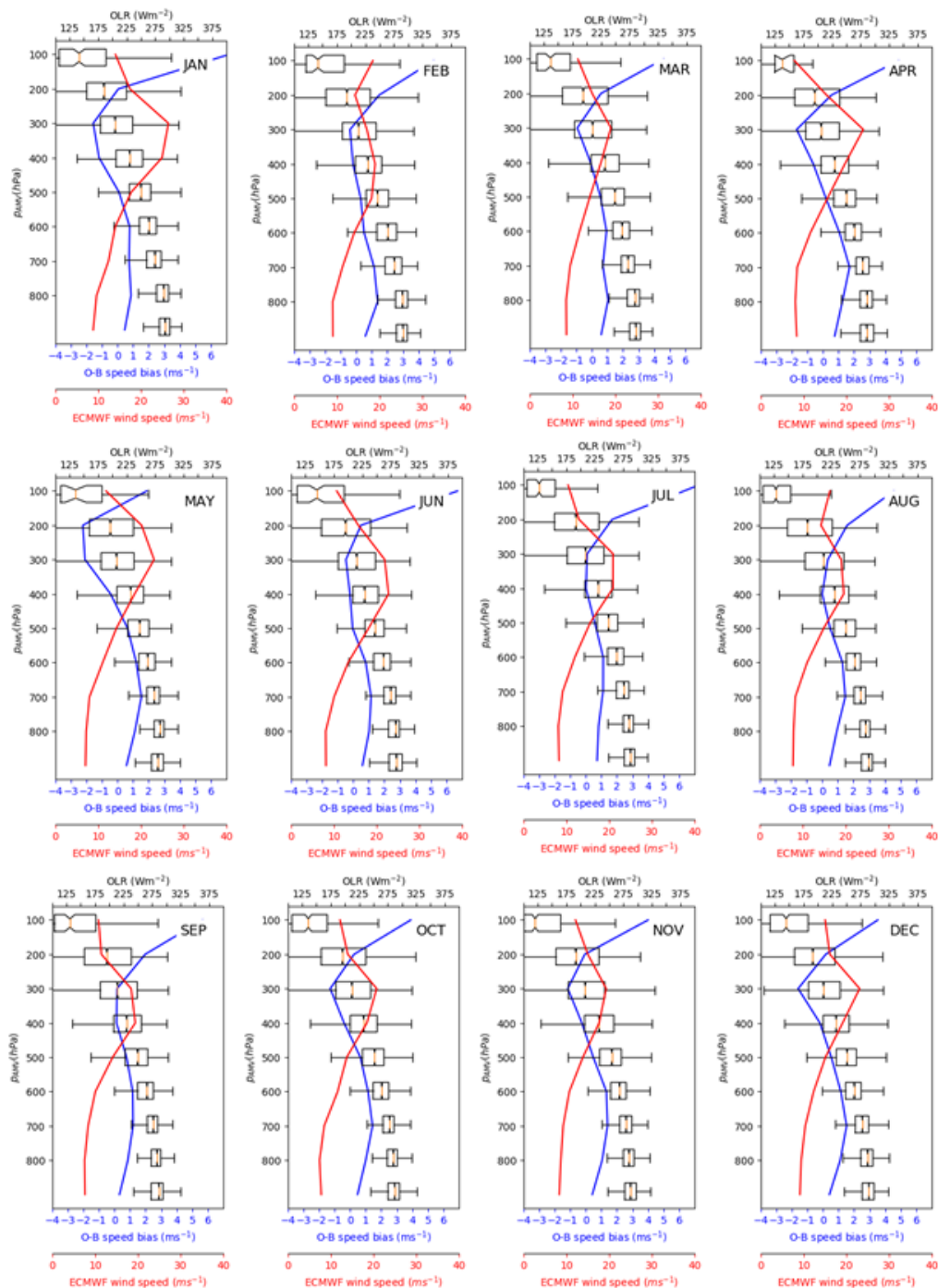



Figure 5.8 : As Figure 5.7, but for Metop AMVs.


	<p align="center">Study of AMV speed biases in the tropics</p> <p align="center">Final Report</p>	
Reference: AMV-TN-0008-TS_Ed1_Rev3	Date : 18/06/2020	Page : 52/118

5.5.2 OLR from AIRS

OLR provided by AIRS are collocated with AMVs if the horizontal separation between AMV and AIRS is less than 75 km and the temporal separation less than 30 min. The quality guidelines of the AIRS science team are followed and any data of low quality is discarded. OLR from AIRS/AMSU aboard AQUA and their comparison to Met10EUM and Metop AMVS and O-B speed biases are given in Figure 5.9 and Figure 5.10, respectively. Few matches are available for Metop/AIRS above 300 hPa ($p < 300$ hPa). Below these altitudes, results resemble that of Sec. 5.5.1 (for both Met10EUM and Metop).

5.5.3 OLR from FY2E/FY2G

OLR are also available from FY2G and FY2E. However, one disadvantage of both FY2E/FY2G OLR and AMV data is the lack of any quality indicator. Nevertheless, in order to complete the suite of OLR to AMV-ECMWF wind speed comparisons, results for FY2G for December 2016 and FY2E for June 2016 are presented in Figure 5.11. In both cases, a strong increase of the O-B speed bias with altitude is apparent. Conversely, the OLR decreases with altitude as expected. Obtained values of the mean speed differences are up to 15 ms^{-1} larger than that obtained for Met10EUM or Metop. However, parts of this large mean speed difference may be due to the lack of quality indicators.

	<p align="center">Study of AMV speed biases in the tropics</p> <p align="center">Final Report</p>	
Reference: AMV-TN-0008-TS_Ed1_Rev3	Date : 18/06/2020	Page : 53/118

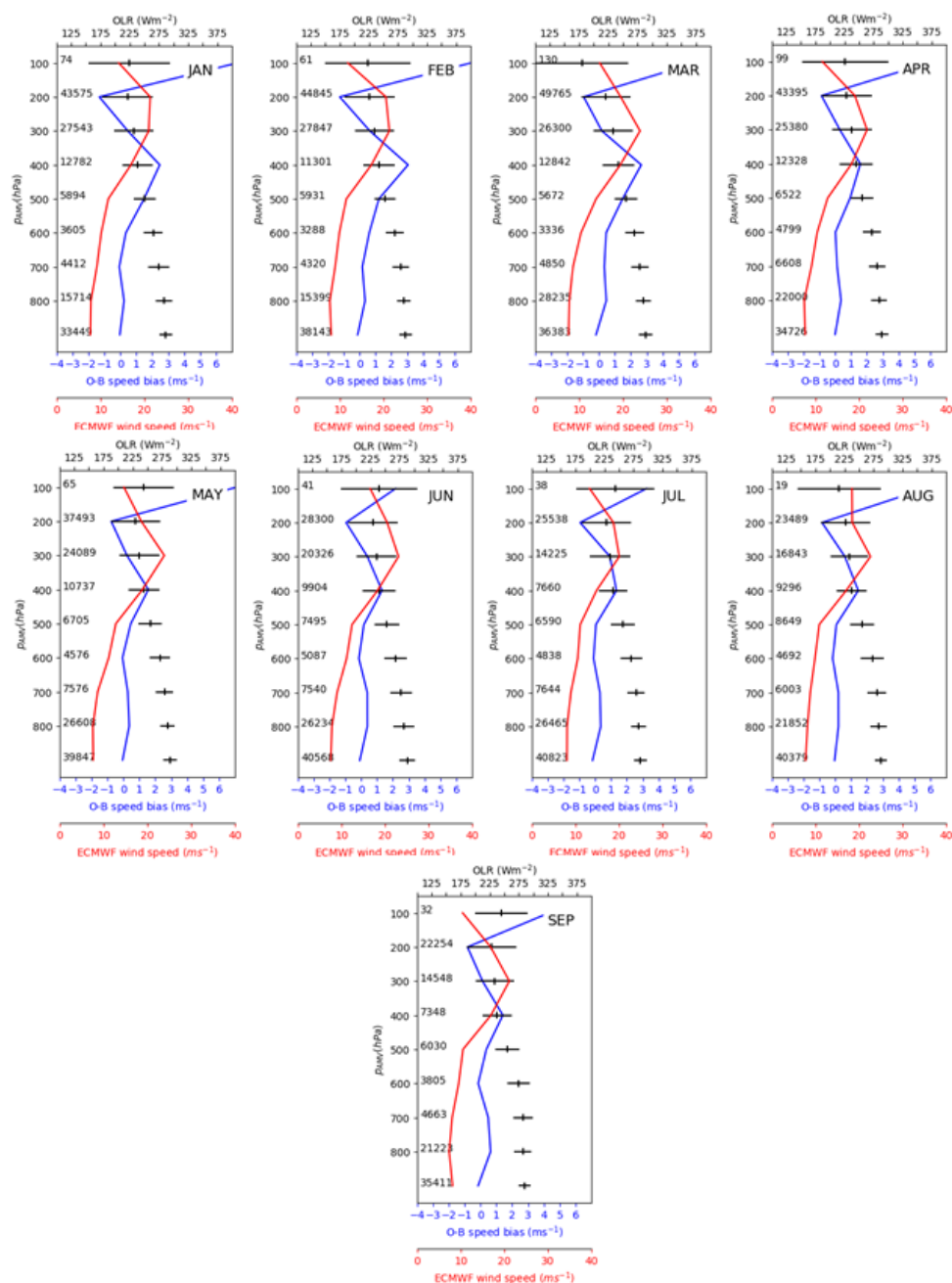



Figure 5.9 : Comparison of AIRS OLR with Met10EUM AMVs. Black horizontal lines denote the mean OLR plus corresponding standard deviations. Corresponding O-B speed bias (Met10EUM-ECMWF) is shown in blue, while collocated ECMWF wind speed is shown in red.

	<h1 style="text-align: center;">Study of AMV speed biases in the tropics</h1> <h2 style="text-align: center;">Final Report</h2>	
Reference: AMV-TN-0008-TS_Ed1_Rev3	Date : 18/06/2020	Page : 54/118

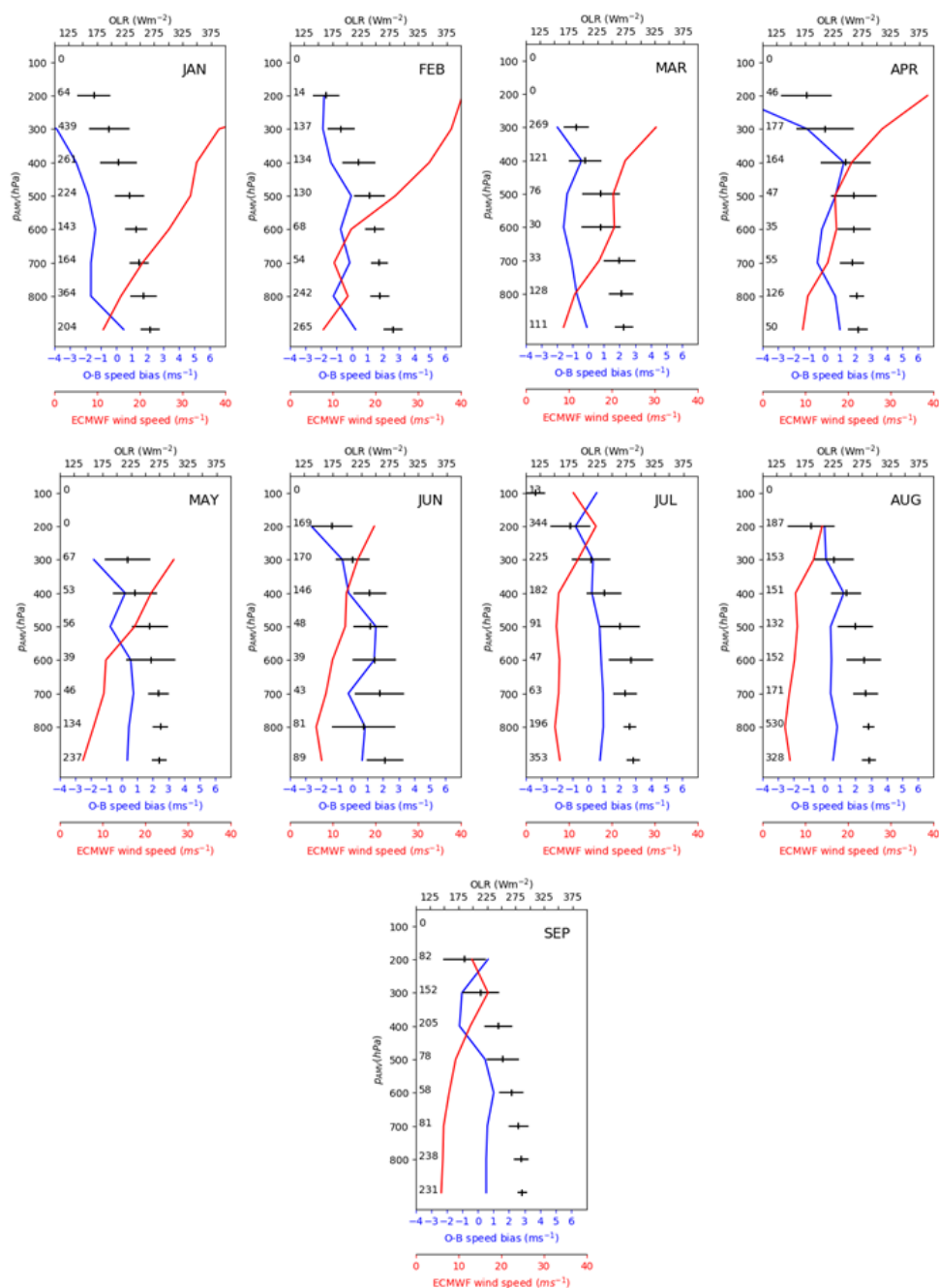



Figure 5.10 : As Figure 5.9, but for AIRS OLR and Metop AMV.

	<p align="center">Study of AMV speed biases in the tropics</p> <p align="center">Final Report</p>	
Reference: AMV-TN-0008-TS_Ed1_Rev3	Date : 18/06/2020	Page : 55/118

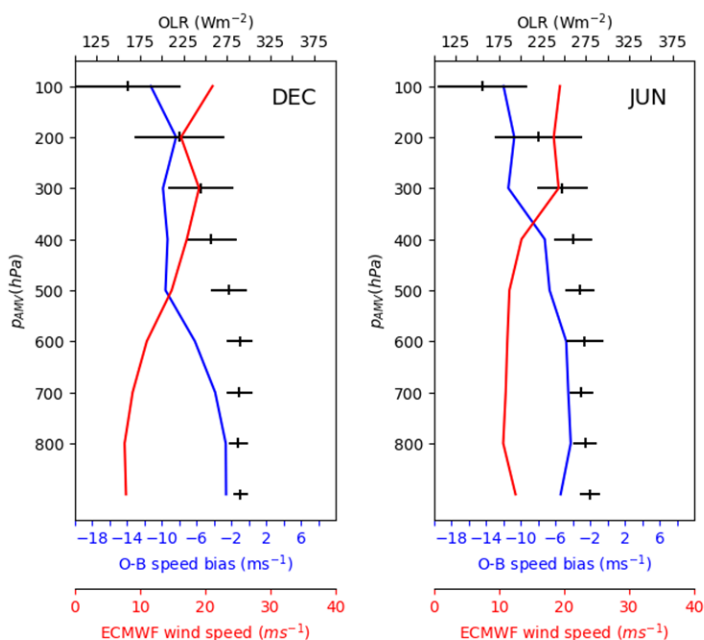


Figure 5.11 : As Fig. 30 but for collocated OLR and AMV from FY2G and FY2E, respectively. (Left) Mean and standard deviation of matched FY2G OLR vs FY2G AMV-ECMWF in December 2016. (Right) Mean and standard deviation of matched FY2E OLR vs FY2E AMV-ECMWF in June 2016.

5.6 STABILITY INDICES – THE GALVEZ-DAVISON INDEX (GDI)

Correlating mean AMV-ECWTF wind speed differences to GDI is another attempt at relating this bias to convection. GDI is described in Galvez and Davison (2016) and requires T and q at 950, 850, 700 and

500 hPa as inputs. Typical GDI values are given in Figure 5.12 and describe the potential for development of specific convective regimes. Note it was intended to calculate the GDI also from T and q profiles of RAOB radiosondes. However, none of the radiosondes flown in the tropics in 2016 provided a humidity profile.

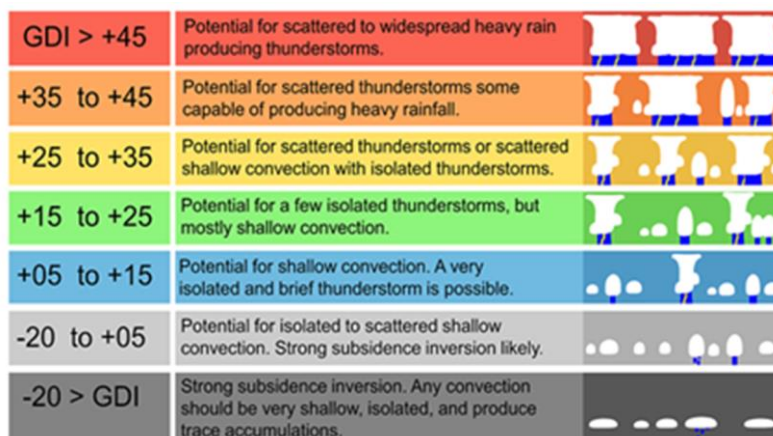



Figure 5.12 : Correspondence between GDI values and expected type of convection. Figure adapted from <http://www.wpc.ncep.noaa.gov/international/gdi/>

5.6.1 GDI from ECMWF

Based on the collocation database established in Sec. 4, collocated T and q profiles are used to compute the GDI. Results for GDI vs O-B speed bias is given in Figure 5.13 for Met10EUM and in Figure 5.14 for Metop, respectively. In general, these figures confirm the findings of the OLR/speed bias analysis. High-level Metop AMVs are taken in stronger convective regimes than Met10EUM AMVs but no clear correlation between convection type and speed bias could be deduced.

5.6.2 GDI from ATOVS

Based on the database of ECMWF and collocated Met10EUM and Metop AMVs established in Sec. 4, ATOVS T and q profiles are considered collocated if they are within a horizontal distance of 75 km and within 30 min. The quality guidelines were followed to ensure these profiles are of high quality. Results for ATOVS GDI and collocated mean speed differences are shown for Met10EUM in Figure 5.15 and for Metop AMVs in Figure 5.16. As for ECMWF OLR, GDI confirms that Metop tend to sense in stronger convective regimes, particularly above 200 hPa ($p < 200$ hPa). However, no clear correlation between convection type and speed bias could be deduced.

	<h1 style="text-align: center;">Study of AMV speed biases in the tropics</h1> <h2 style="text-align: center;">Final Report</h2>	
Reference: AMV-TN-0008-TS_Ed1_Rev3	Date : 18/06/2020	Page : 57/118

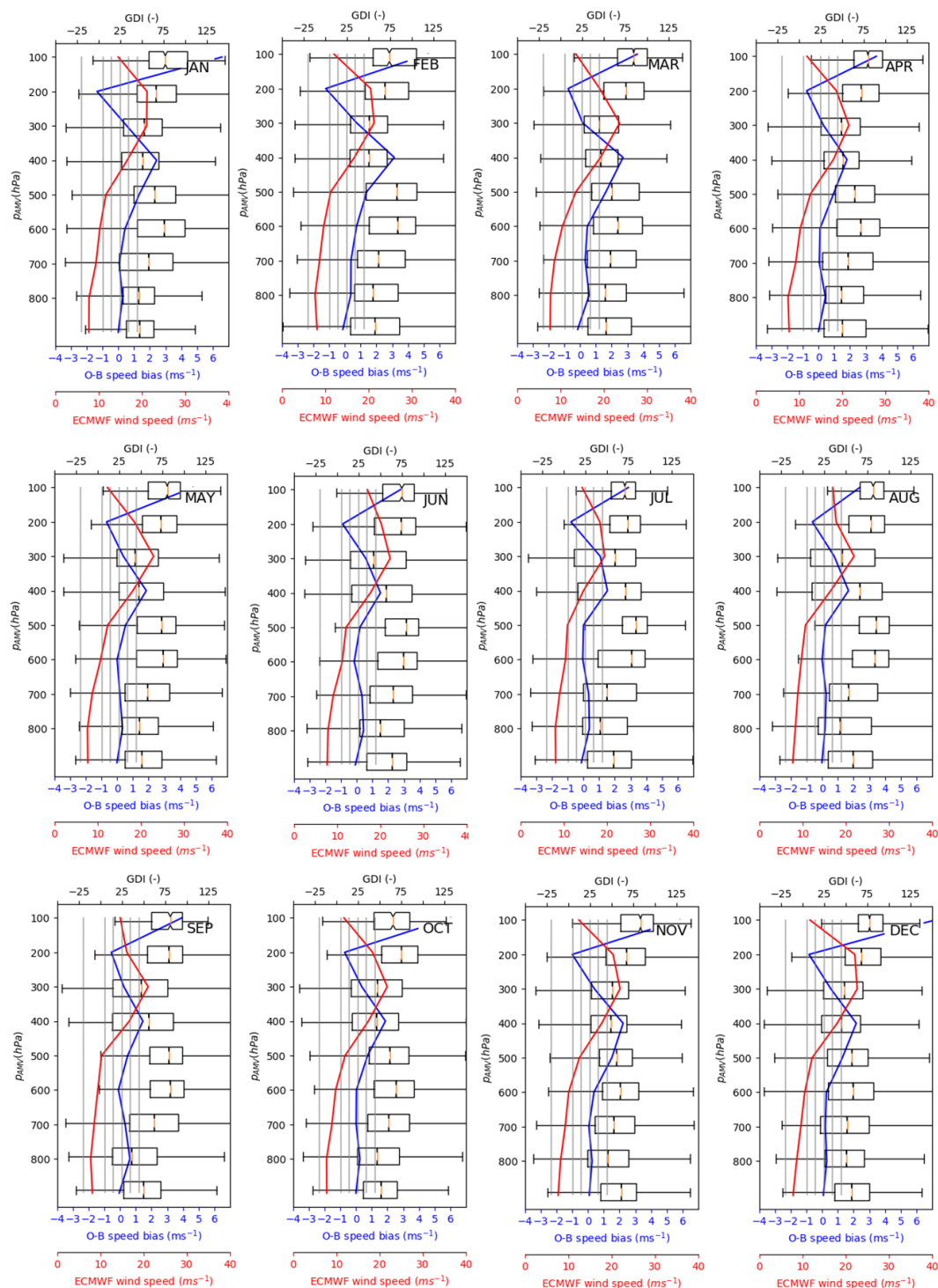

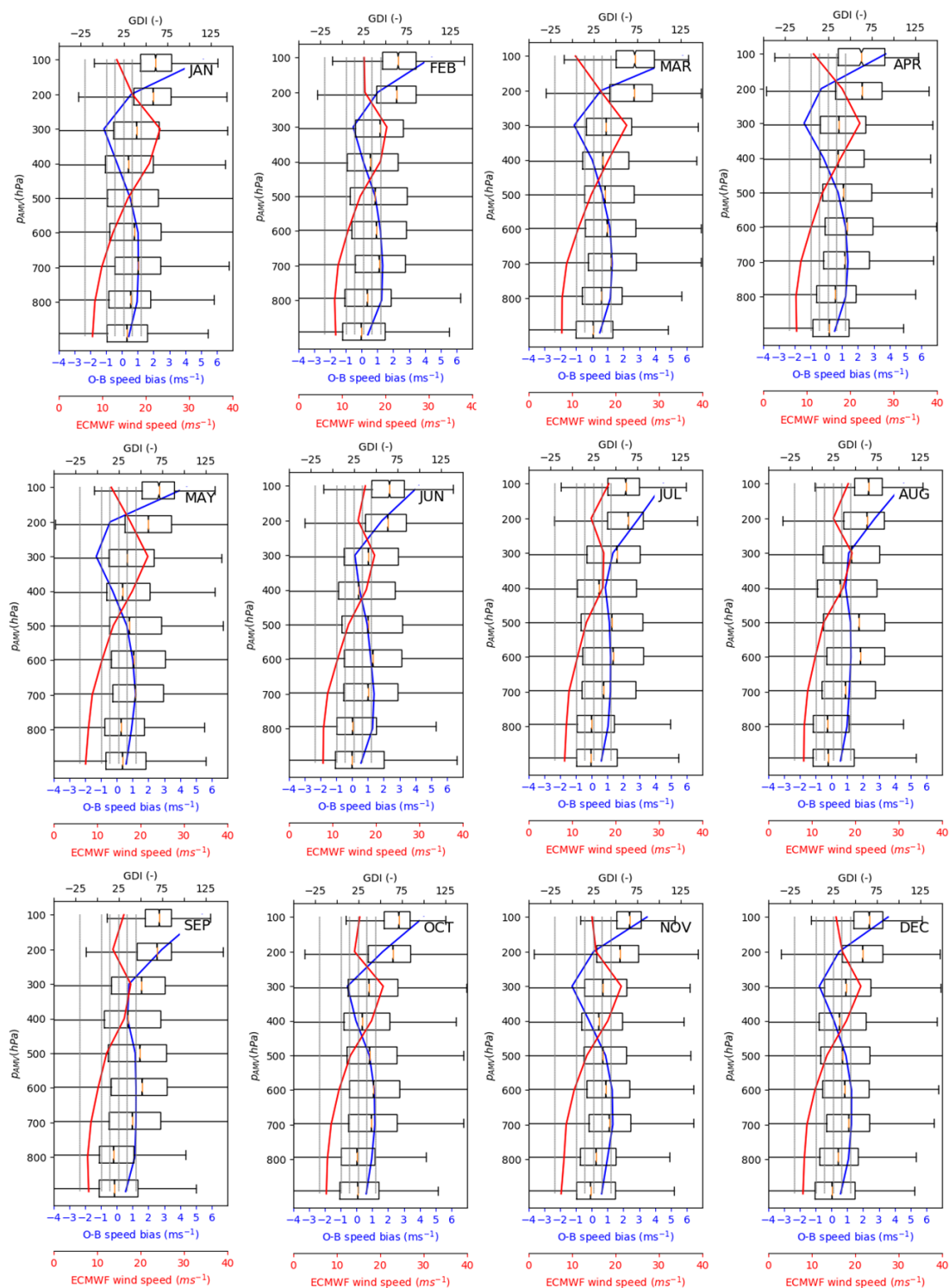


Figure 5.13 : Comparison of ECMWF GDI with Met10EUM AMVs. Box-and-whisker plots of GDI are shown for different AMV pressure levels. Each box extends from the lower (25%) to upper quartile (75%) values of the pressure differences, with a line at the median. Corresponding O-B

	<h1 style="text-align: center;">Study of AMV speed biases in the tropics</h1> <h2 style="text-align: center;">Final Report</h2>	
Reference: AMV-TN-0008-TS_Ed1_Rev3	Date : 18/06/2020	Page : 58/118

speed bias is shown in blue, while ECMWF speeds are shown in red. The grey vertical stripes denote the border of the different convective regimes according to Figure 5.12.




	<p style="text-align: center;">Study of AMV speed biases in the tropics</p> <p style="text-align: center;">Final Report</p>	
Reference: AMV-TN-0008-TS_Ed1_Rev3	Date : 18/06/2020	Page : 59/118

Figure 5.14 : As Figure 5.13, but for Metop AMVs.

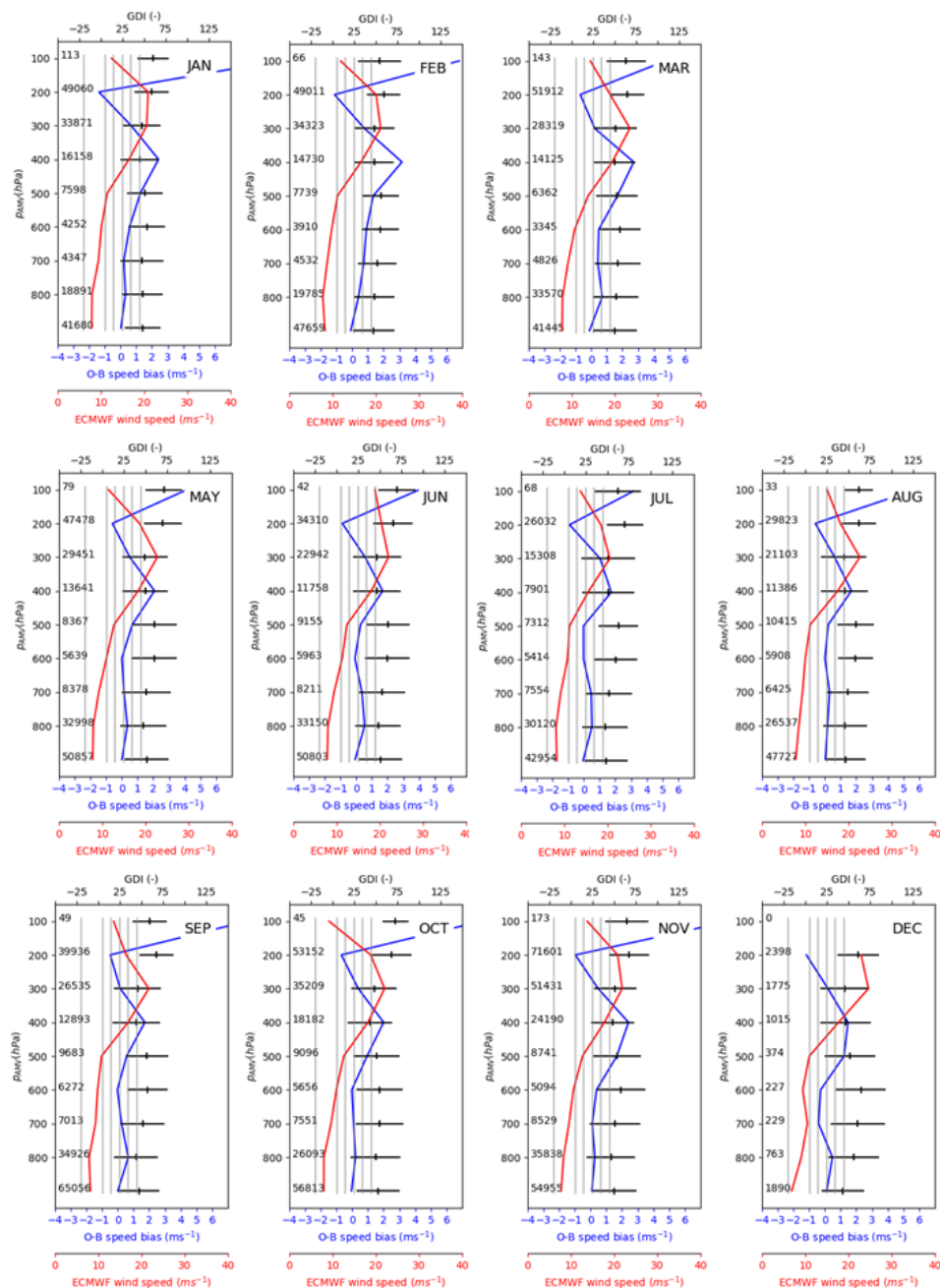



Figure 5.15 : Comparison of ATOVS GDI with Met10EUM AMVs. Black horizontal lines denote the mean GDI values plus corresponding standard deviations. Corresponding O-B speed bias (Met10EUM-ECMWF) is shown in blue, while ECMWF speed is shown in red. The grey vertical stripes denote the border of the different convective regimes according to Figure 5.12.

	<p align="center">Study of AMV speed biases in the tropics</p> <p align="center">Final Report</p>	
Reference: AMV-TN-0008-TS_Ed1_Rev3	Date : 18/06/2020	Page : 60/118

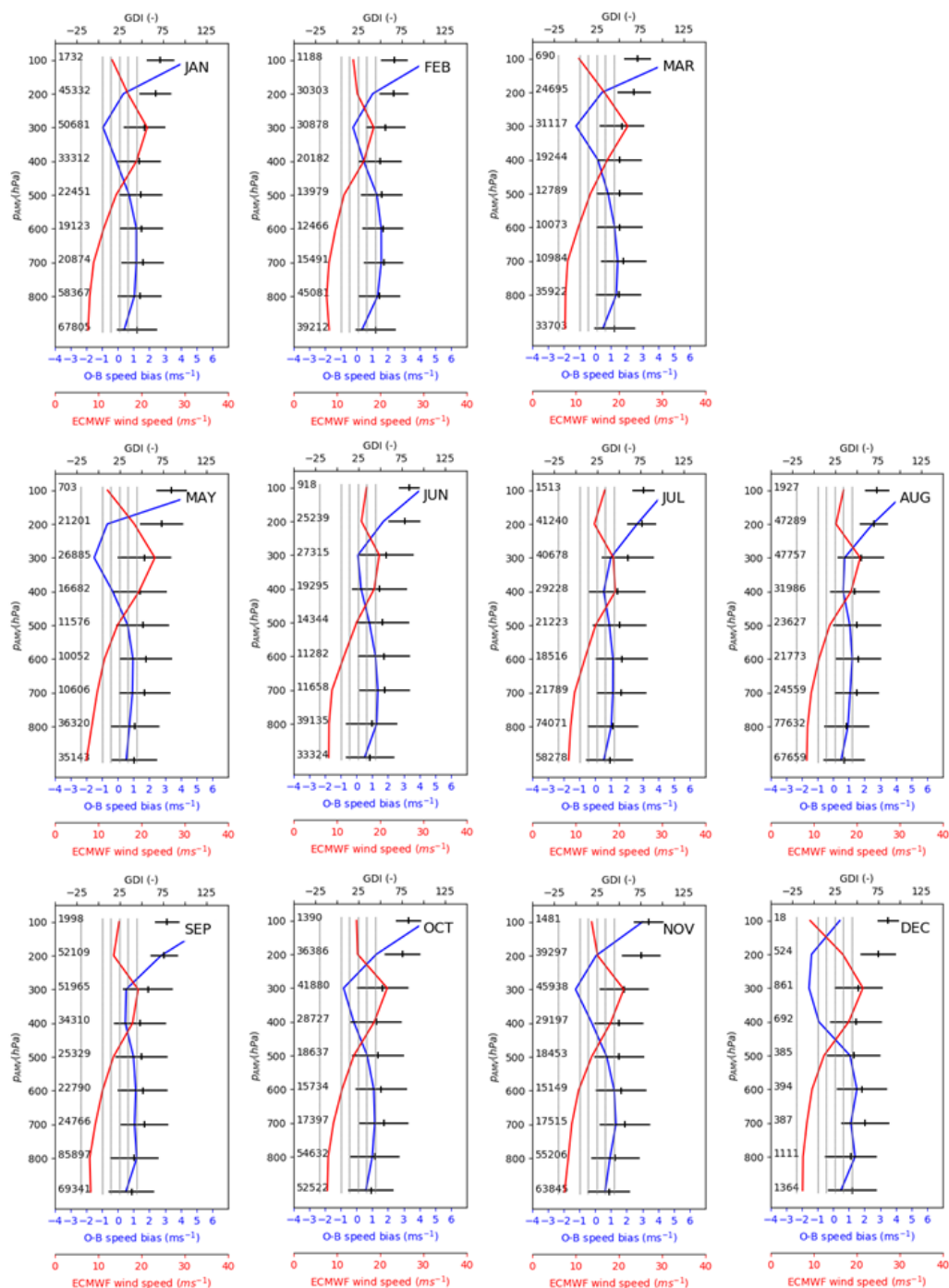



Figure 5.16 : As Figure 5.15, but for Metop AMVs.

	<p align="center">Study of AMV speed biases in the tropics</p> <p align="center">Final Report</p>	
Reference: AMV-TN-0008-TS_Ed1_Rev3	Date : 18/06/2020	Page : 61/118

6 CASE STUDIES

Two cases of AMV performance are being studied in detail. The first one (Section 6.1) studies the Met10EUM IR AMV mid- and high-level speed bias over Saharan desert in March 2016 during westerly jet, while the second (6.2) investigates the Dual-Metop IR AMV mid- and high-level speed bias over the Boiler-Box region in August 2016.

6.1 MET10EUM AMV PERFORMANCE OVER SAHARA DESERT

6.1.1 Analysis of semivariograms

6.1.1.1 Method

The previous analysis (Speed bias as function of time of day, OLR, GDI, CLOUDSAT cloud classification) indicate little dependency of O-B speed bias on the strength and type of convection and on cloud type. Comparison of Met10AMV pressures to CALIPSO/CALIOP cloud top heights revealed that AMVs tend to have assigned too low altitudes at high levels. However, collocated O-B speed bias tends to be negative (except for the 400 hPa level), which cannot be explained by having AMVs set too low in the atmosphere. Analysing the spatial variance of AMV and model speed over a region allows verifying the similarity of the wind fields (e.g. position and strength of jet). In spatial statistics, this is commonly achieved by plotting the semivariances as function of lag distance ("semivariogram"). The empirical semivariance $\gamma(h)$ can be calculated according to


$$\hat{\gamma}(h) = \frac{1}{2N(h)} \sum_i^{N(h)} (z(x_i) - z(x_i + h))^2 \quad (1)$$

Here, h is a distance, and $z(x_i)$ and $z(x_i + h)$ are two data points (e.g. model wind speed at the same pressure level and time) at locations x_i and $x_i + h$. The $N(h)$ term is the number of points we have that are separated by the distance h . The empirical semivariance $\gamma(h)$ then is the sum of squared differences between values separated by a distance h .

The semivariogram analysis use the collocation database established in Sec. 4. The ECMWF semivariances thus comprise only purely horizontal variances at a given time, while semivariances of AMV also include a small portion of vertical variances, which are introduced by the vertical matching criterion of 25 hPa.

6.1.1.2 Application to 7-day jet situation

Mean wind speeds reported by collocated ECMWF and Met10EUM over a 7-day westerly jet situation (22.3 – 28.3.2016) over Northern Africa are displayed in Figure 6.1 for high-level, mid-level and low-level winds. At high levels ($p_{\text{ECMWF}} \leq 400$ hPa), the geographic pattern of O-B speed bias – positive speed bias along northern edge of jet, negative bias along southern edge of jet – suggest a different location of the subtropical jet in observed and model winds. In contrast to high-level winds, for mid-level winds ($400 \text{ hPa} < p_{\text{ECMWF}} \leq 700$ hPa), O-B speed bias is mainly positive. In addition, in contrast to ECMWF, AMVs faster than 45 ms^{-1} extend to lower levels, indicating that height assignment errors are mainly responsible for the observed O-B speed bias. At low levels ($p_{\text{ECMWF}} > 700$ hPa), model and observed wind typically agree better than 1 ms^{-1} .

	<p align="center">Study of AMV speed biases in the tropics</p> <p align="center">Final Report</p>	
Reference: AMV-TN-0008-TS_Ed1_Rev3	Date : 18/06/2020	Page : 62/118

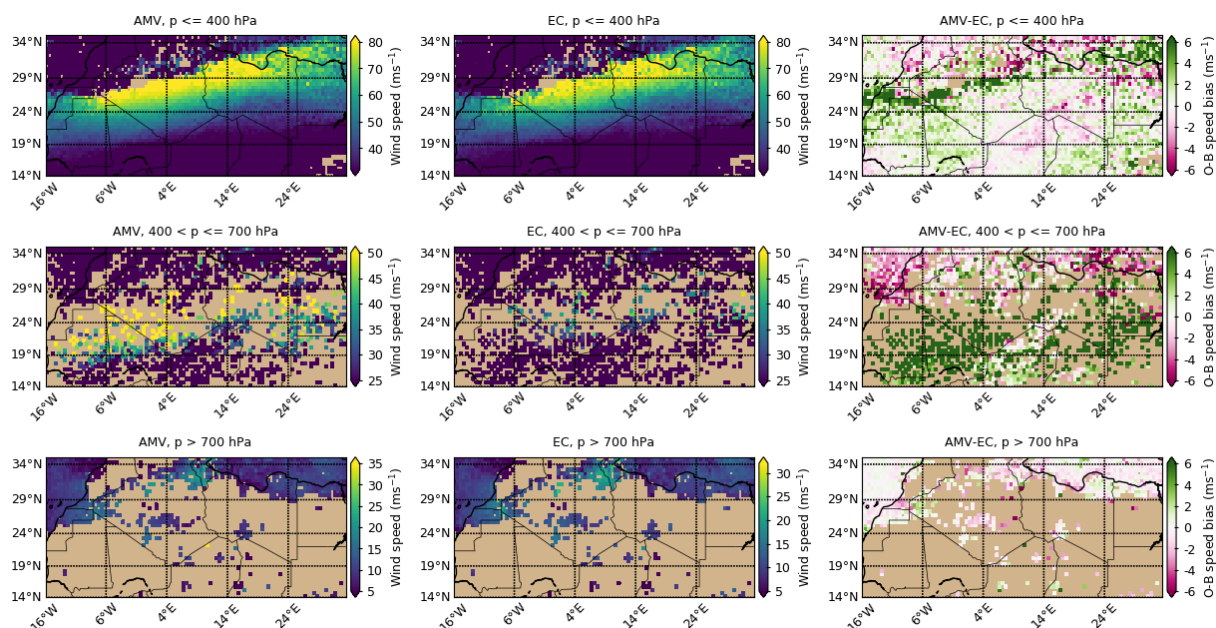


Figure 6.1 : 7-day jet situation (22.3 – 28.3.2016) over Northern Africa as seen by Met10EUM and ECMWF. (Left) Mean wind speed observed by Met10EUM at high-, mid- and low-level. (Centre) Mean wind speed observed by ECMWF at high-, mid- and low-level. (Right) Corresponding wind speed differences between Met10EUM and ECMWF.

Mean wind speeds along $\pm 1.5^\circ$ broad North-South transects and corresponding semivariograms are used to investigate the position of the jet in collocated observed and model winds. At 200 hPa, the latitudinal wind speed profile of AMV and ECMWF appear similar (Figure 6.2), which is confirmed by the corresponding semivariograms (Figure 6.3). At 300 hPa, latitudinal wind speed profiles indicate faster AMVs than model winds, particularly between -16° to $10^\circ\text{E}/20^\circ$ to 26°N differences amount to 10 ms^{-1} (Figure 6.4). Corresponding semivariograms (Figure 6.5) indicate a relatively similar pattern of semivariances for AMVs and ECMWF winds (e.g. position of lows and peaks as well as evolution of semivariances with increasing lag distance h). However, AMV semivariances increase much faster with distance h than ECMWF semivariances, i.e., AMVs exhibit lower correlation within increasing distance than ECMWF, which may be interpreted that the jets observed by AMVs reach higher speed levels (i.e. faster winds) than ECMWF. Differences in the pattern of the semivariograms (mostly at lag distances $> 400\text{ km}$) may indicate that the jet observed by AMVs peak at slightly different locations. At 400 hPa, latitudinal wind profiles of AMV and model winds are regularly found different (Figure 6.6), with AMV wind speeds frequently reaching speed levels that have been found also at 300 hPa. AMV semivariances increase much stronger with increasing distance than ECMWF semivariances (Figure 6.7) and the structure of the semivariances is quite different between model and observed winds, indicating that rather than the horizontal position of the jet, differences in the vertical position of the jet lead to the observed O-B speed biases of up to 20 ms^{-1} .

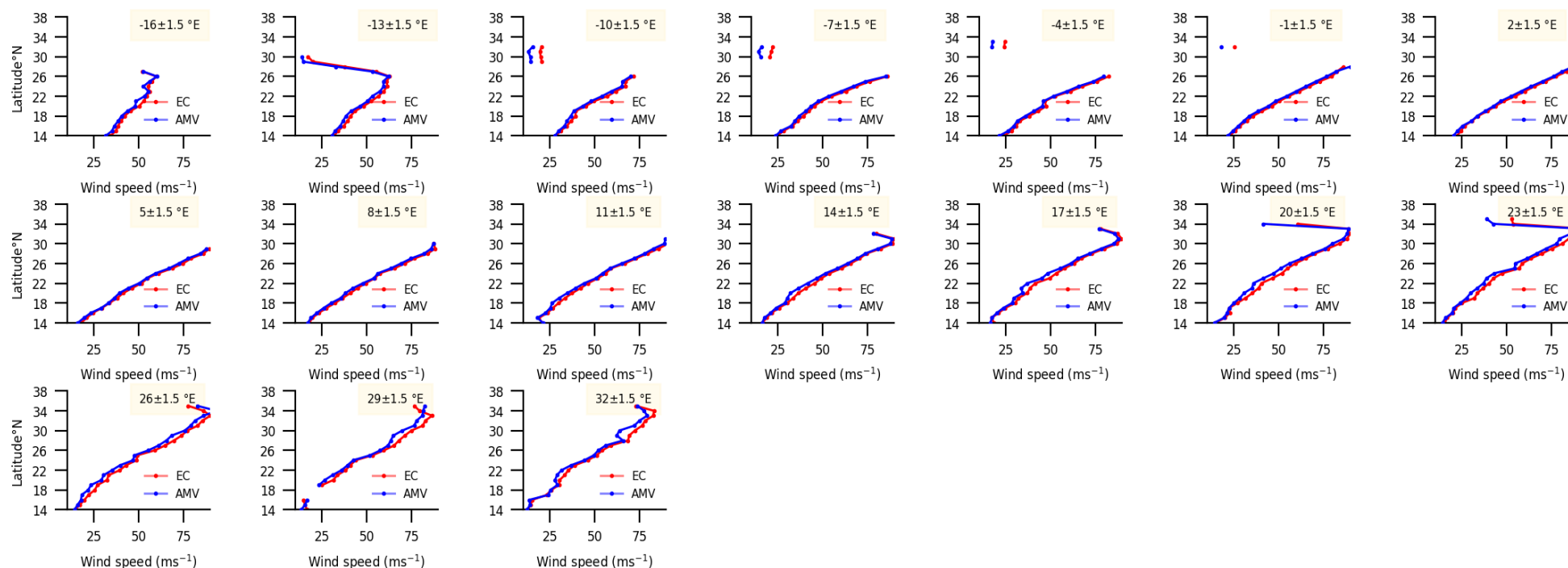


Figure 6.2 : Observed and model winds over the Sahara desert at the 200 hPa, averaged from 22.3 to 28.3.2016. Depicted are ECMWF winds (red) and AMV from Met10EUM (blue) over $\pm 1.5^\circ$ longitude bands (transects).

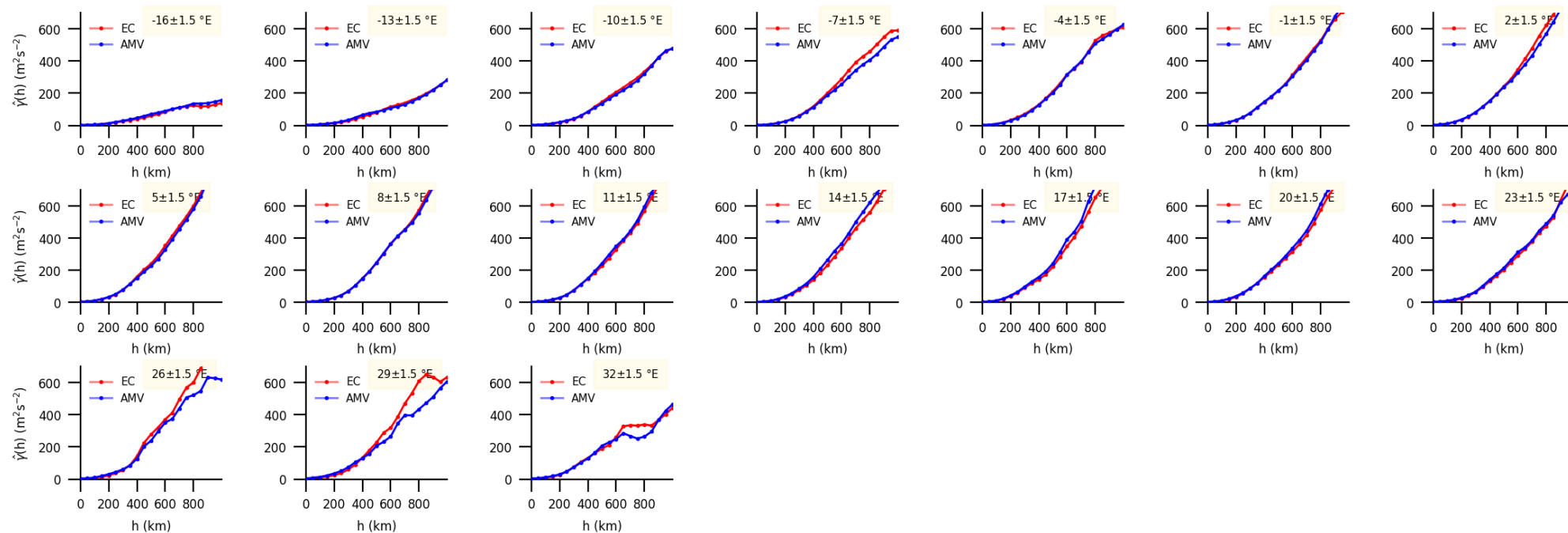


Figure 6.3: Semivariograms along North-South transects of observed (AMV) and model (ECMWF) winds over the Sahara desert at the 200 hPa, averaged from 22.3 to 28.3.2016.

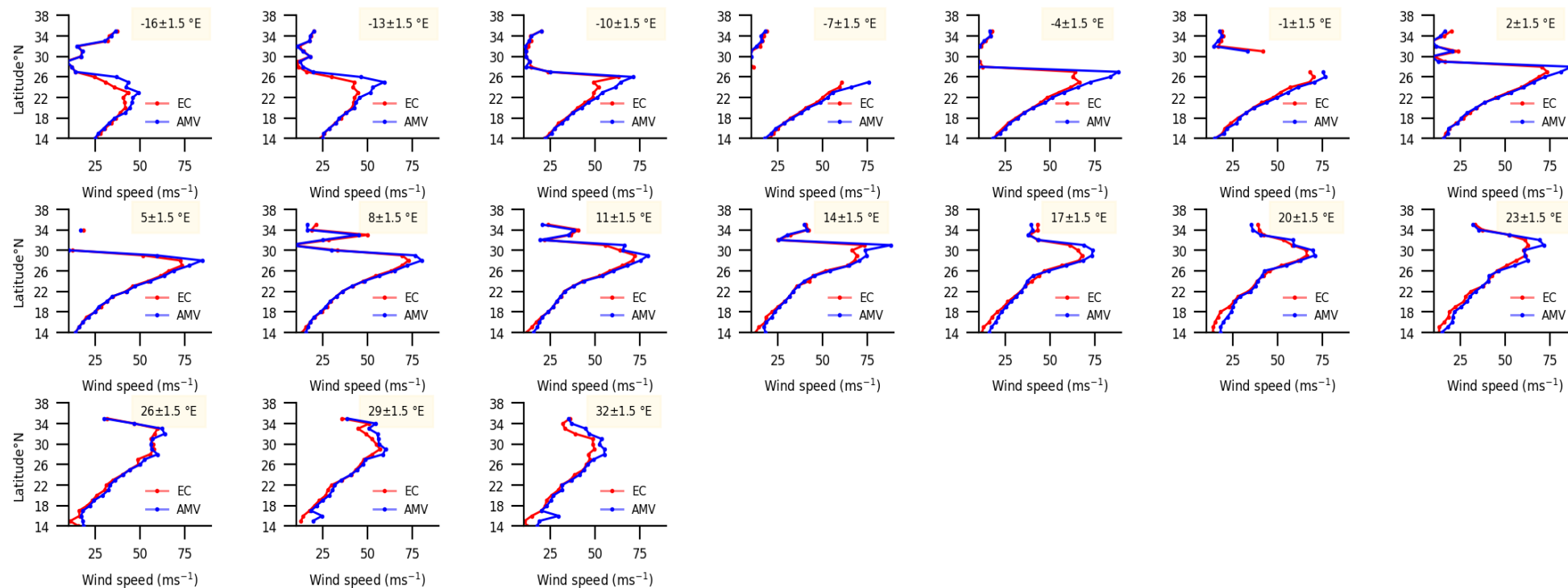


Figure 6.4 : Observed and model winds over the Sahara desert at the 300 hPa, averaged from 22.3 to 28.3.2016. Depicted are ECMWF winds (red) and AMV from Met10EUM (blue) over $\pm 1.5^\circ$ longitude bands (transects).

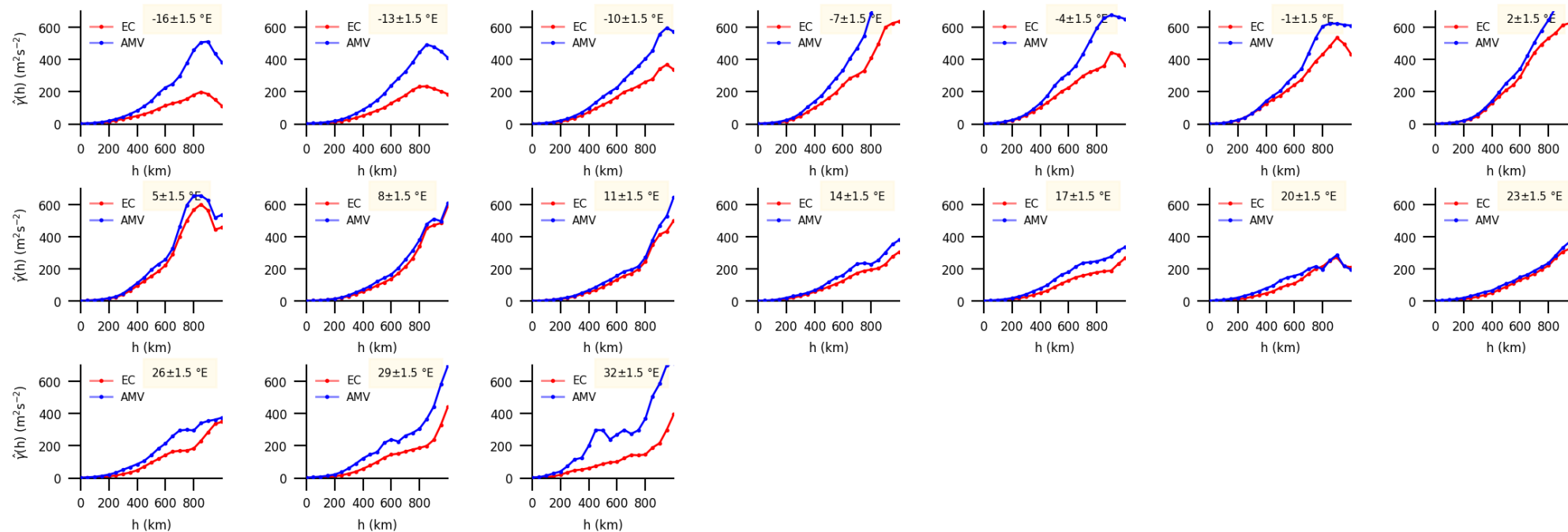


Figure 6.5: Semivariograms along North-South transects of observed (AMV) and model (ECMWF) winds over the Sahara desert at the 300 hPa, averaged from 22.3 to 28.3.2016.

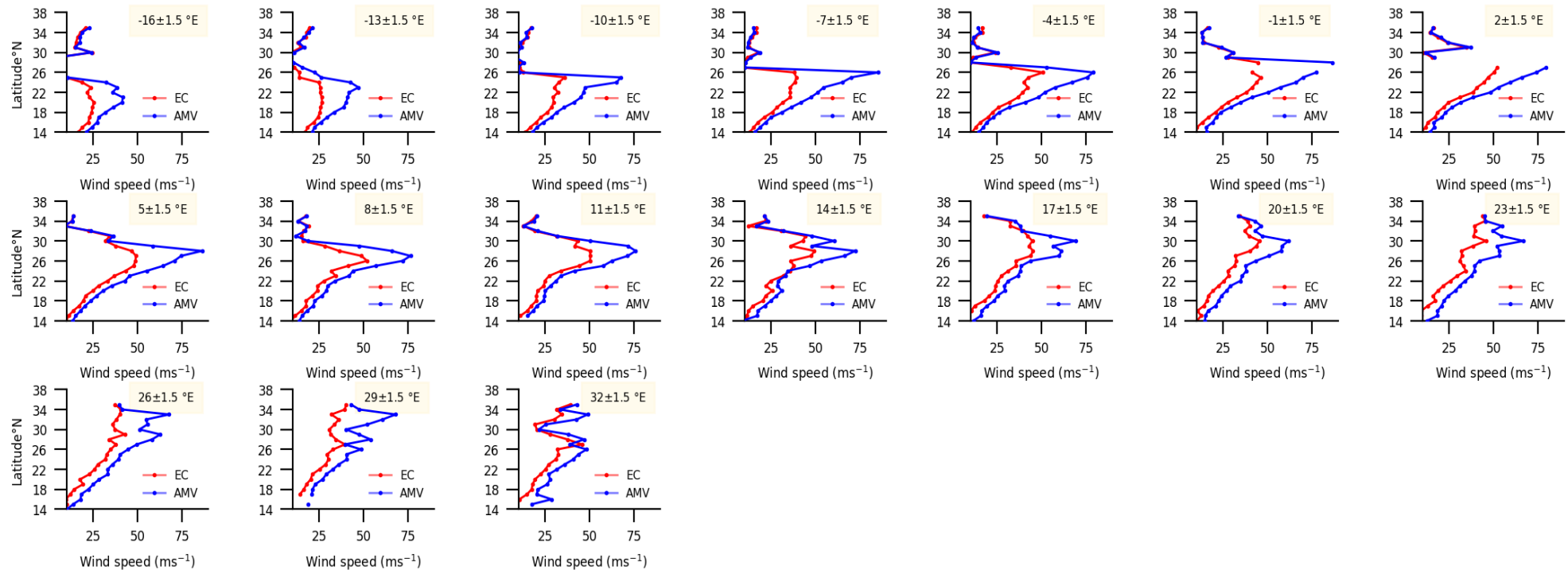


Figure 6.6 : Observed and model winds over the Sahara desert at the 400 hPa, averaged from 22.3 to 28.3.2016. Depicted are ECMWF winds (red) and AMV from Met10EUM (blue) over $\pm 1.5^\circ$ longitude bands (transects).

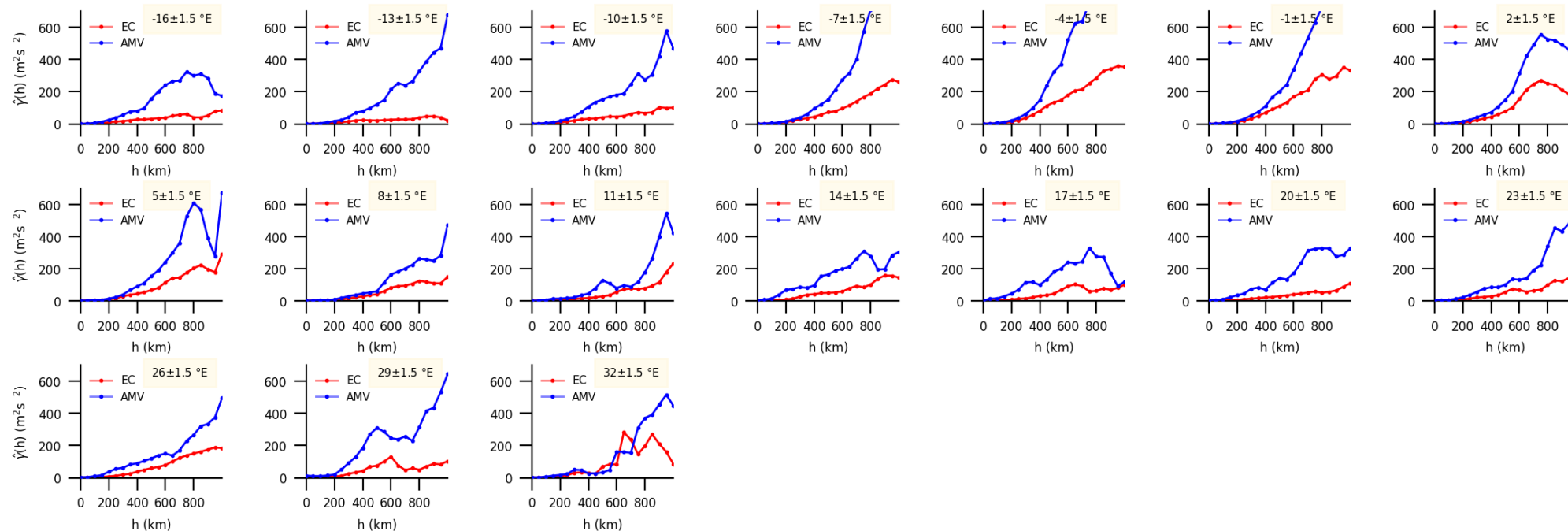



Figure 6.7 : Semivariograms along North-South transects of observed (AMV) and model (ECMWF) winds over the Sahara desert at the 400 hPa, averaged from 22.3 to 28.3.2016.

	<p align="center">Study of AMV speed biases in the tropics</p> <p align="center">Final Report</p>	
Reference: AMV-TN-0008-TS_Ed1_Rev3	Date : 18/06/2020	Page : 69/118

6.1.2 Visual comparison of wind fields

The analysis of semivariograms (Sec. 6) revealed that Met10EUM AMVs and model winds exhibit different spatial structures of wind over the Sahara desert, particularly for levels between 300 and 400 hPa. While at 300 hPa the different (horizontal) position of the jet appear responsible for the observed speed biases, at 400 hPa erroneous AMV heights likely are responsible. Due to large wind speed and wind shears during subtropical westerly jet in March 2016, proper height assignment is critical. Any errors, for instance from contributions from below the cloud top (e.g. warm desert surface temperature, errors in surface emissivity) that lead to retrieving a too warm (and therefore too low) cloud top, can translate to relatively large discrepancies in between satellite-derived and model wind. We compare visually the AMVs to ECMWF fields to check for similarities in the obtained wind fields. Thus, no vertical collocation criterion is applied. Cloud top heights and cloud type classification data from the cloud profiling radar (CPR) aboard CLOUDSAT are utilised in the visual comparison as they indicate if heights are assigned correctly. CALIPSO (both launched April 28, 2006) is also part of the so-called "A-Train" constellation and flies along the same orbit at a distance of only 10-15 seconds (CLOUDSAT leads) so that footprints of both sensors (CPR and CALIOP) overlap. However, in March 2016, CALIPSO data are not available for the first two weeks of the month.

An example of a CLOUDSAT overpass over the region of interest during afternoon and corresponding AMVs found within ± 30 min of the CLOUDSAT overpass are given in Figure 6.8. Along this CLOUDSAT overpass, cloud top heights and corresponding cloud type classification obtained by the CPR are compared to AMV pressure. As CPR heights are given as geometric heights, their conversion to pressure uses geopotential and temperature profiles from ECMWF. When comparing CPR and AMV pressure, one has to keep in mind SEVIRI and CLOUDSAT do not necessarily observe the same clouds. This due to spatio-temporal collocations as well as the fact that AMVs are derived from SEVIRI images by tracking cloudy pixels using a correlation algorithm, while the nadir-looking radar derives heights from the measured power of backscattered clouds at an along-track resolution of 1.7 km. Nevertheless, qualitative comparison of both products can reveal potentially erroneous AMV altitudes.

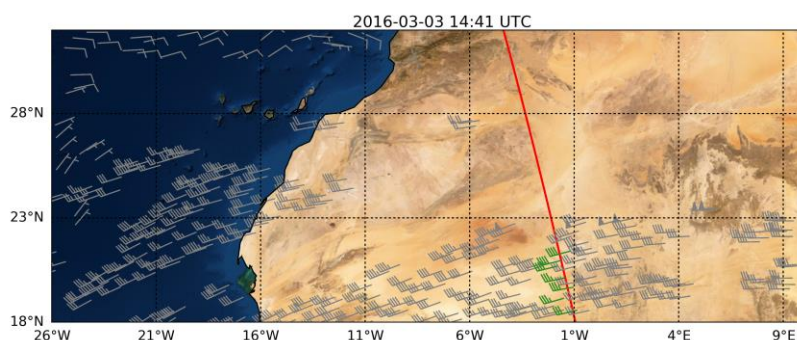



Figure 6.8 : CLOUDSAT overpass on 3 March 2016 at 14:41 UTC. Wind barbs denote the Met10EUM found within ± 30 min of the CLOUDSAT overpass. Green wind bars are within $\pm 0.4^\circ$ latitude and $\pm 0.4^\circ$ longitude of the CLOUDSAT overpass.

Figure 6.9 reveals that the observed (positive) AMV-to-model wind discrepancies larger than 3 ms^{-1} (e.g. the two AMVs assigned to around 400-hPa; see Figure 6.10) can be related to altitudes assigned too low in the atmosphere. Furthermore, by moving these AMVs up, visual agreement with ECMWF winds can be achieved, corroborating the observation from CPR CLTH. Interestingly, one AMV (at 19°N , ~ 260 hPa) is about 6 ms^{-1} slower than model winds interpolated to the AMV altitude (Figure 6.10). Typically,

	<p align="center">Study of AMV speed biases in the tropics</p> <p align="center">Final Report</p>	
Reference: AMV-TN-0008-TS_Ed1_Rev3	Date : 18/06/2020	Page : 70/118

negative speed biases are explained by having assigned an altitude too high in the atmosphere. However, according to CPR heights, the assigned altitude is too low.

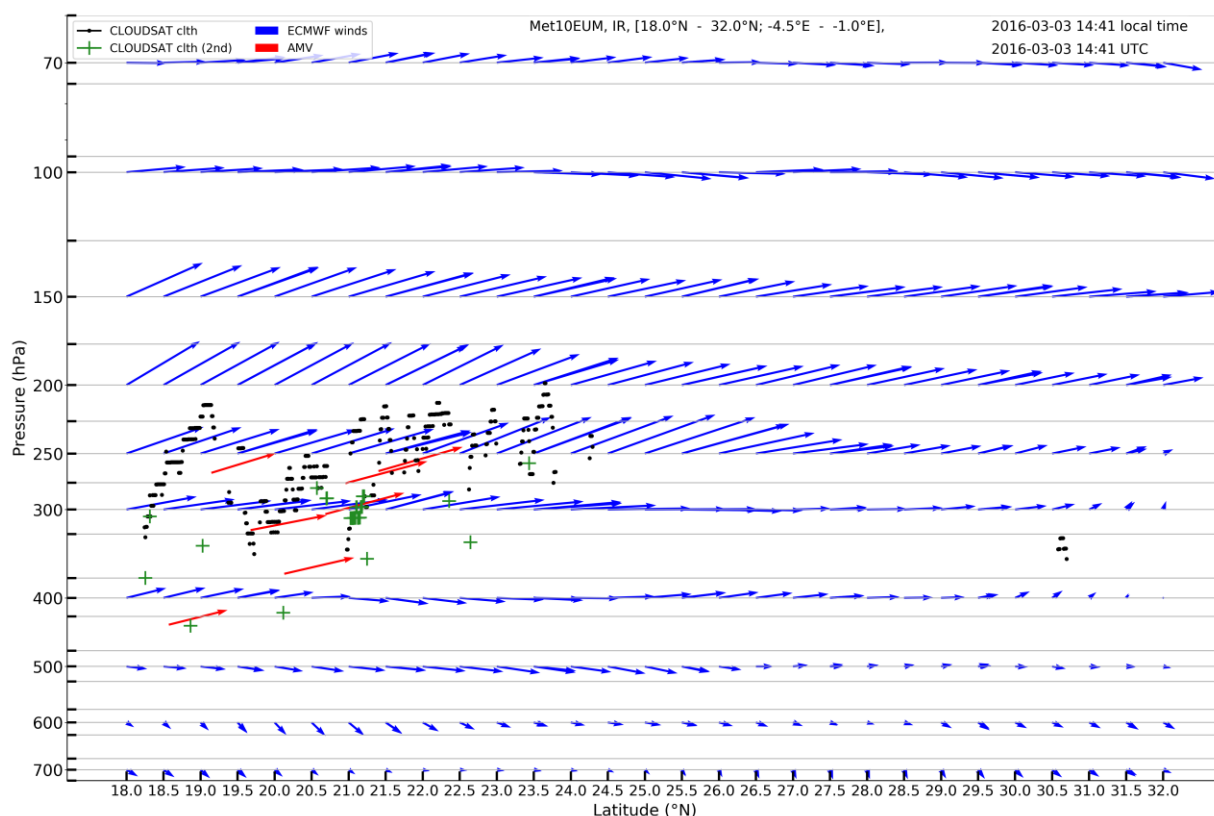


Figure 6.9 : Observed and model winds for a CLOUDSAT overpass over the Sahara desert on 3 March, 14:41 UTC. (Blue) ECMWF wind fields. (Red arrows) AMV obtained within $\pm 0.4^\circ$ latitude and $\pm 0.4^\circ$ longitude and ± 30 min of the CLOUDSAT overpass. (Black dots) Cloud top height computed from CPR data. (Green crosses) Height of a second cloud layer computed from CPR data. Numbers in the square bracket denote latitude and longitude information of the transect. Each ECMWF pressure level is surrounded by two grey lines, indicating the upper and lower limit of the $\Delta p \leq 25\text{hPa}$ collocation criterion used to derive mean statistics presented in Section 4.2.

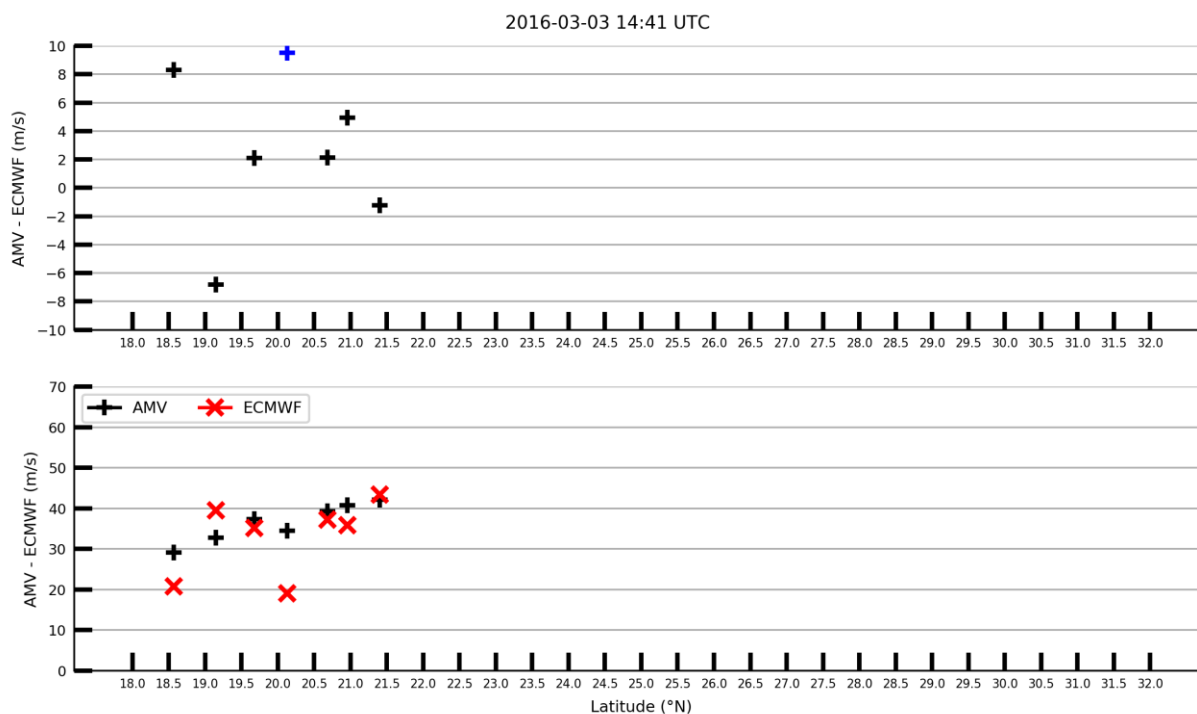



Figure 6.10 : Model wind vs Met10EUM AMVs during a CLOUDSAT overpass over the Sahara desert on 3 March, 14:41 UTC. (Upper panel): Wind speed differences between AMV and model winds interpolated to the AMV altitude. The blue plus sign indicates that the observed difference is larger than 9.5 ms⁻¹. (Lower panel): Corresponding wind speed of AMV and model.

Another example of a north-south transect is given in Figure 6.11 to Figure 6.12. Most AMVs agree with model winds within ± 2 ms⁻¹ (Figure 6.13). Two AMVs, located between 250 to 300 hPa, are about 6 ms⁻¹

	<p align="center">Study of AMV speed biases in the tropics</p> <p align="center">Final Report</p>	
Reference: AMV-TN-0008-TS_Ed1_Rev3	Date : 18/06/2020	Page : 72/118

faster than nearby model winds. Visual comparison to ECMWF as well as CPR cloud top heights indicate that both AMVs have altitudes assigned too low.

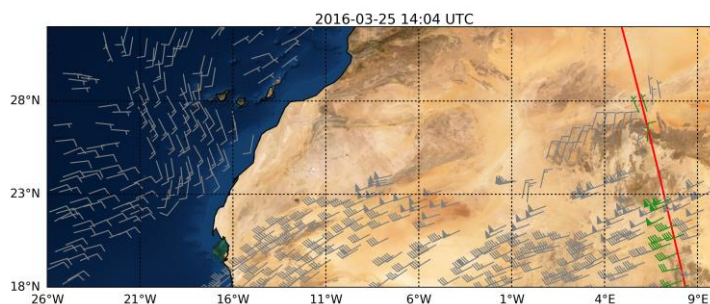


Figure 6.11 : CLOUDSAT overpass on 25 March 2016 at 14:04 UTC. Wind barbs denote the Met10EUM found within ± 30 min of the CLOUDSAT overpass. Green wind bars are within $\pm 0.4^\circ$ latitude and $\pm 0.4^\circ$ longitude of the CLOUDSAT overpass.

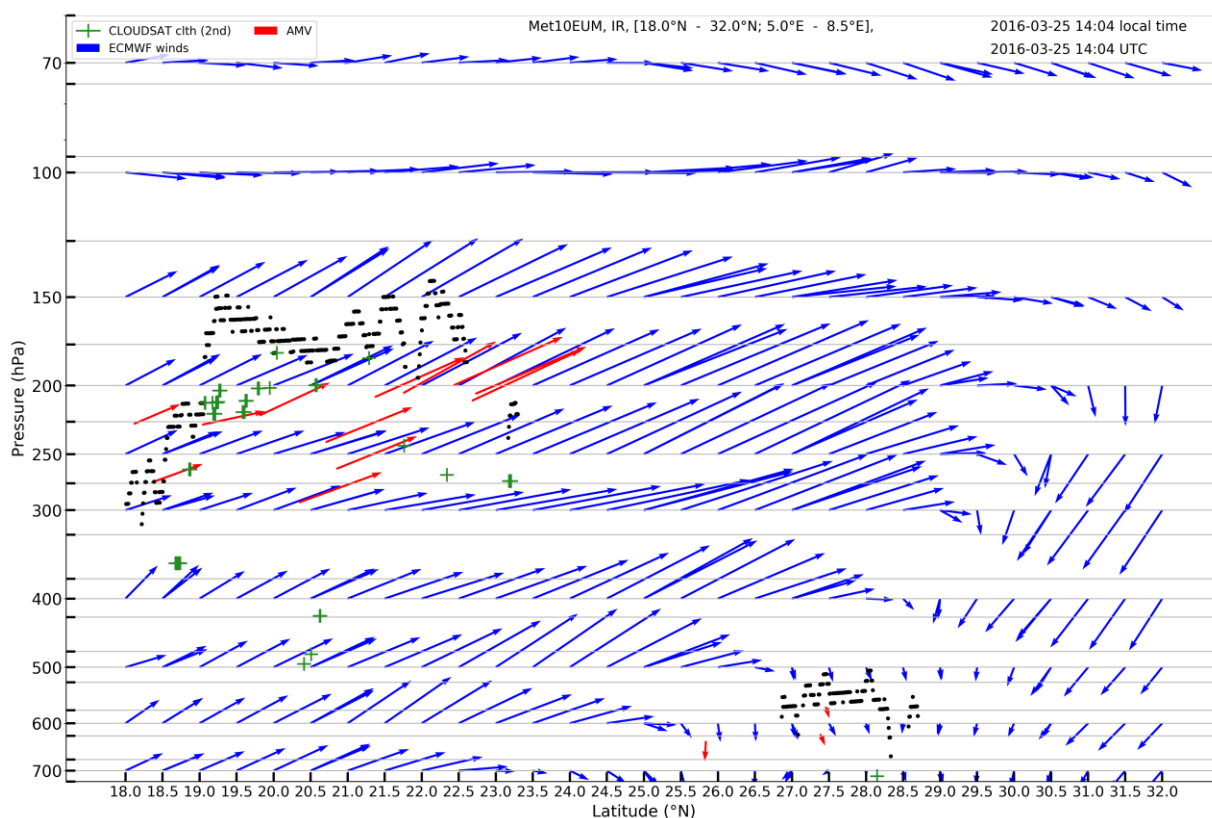


Figure 6.12 : Observed and model winds for a CLOUDSAT overpass over the Sahara desert on 25 March, 14:04 UTC. (Blue) ECMWF wind fields. (Red arrows) AMV obtained within $\pm 0.4^\circ$ latitude and $\pm 0.4^\circ$ longitude and ± 30 min of the CLOUDSAT overpass. (Black dots) Cloud top height computed from CPR data. (Green crosses) Height of a second cloud layer computed from CPR data.

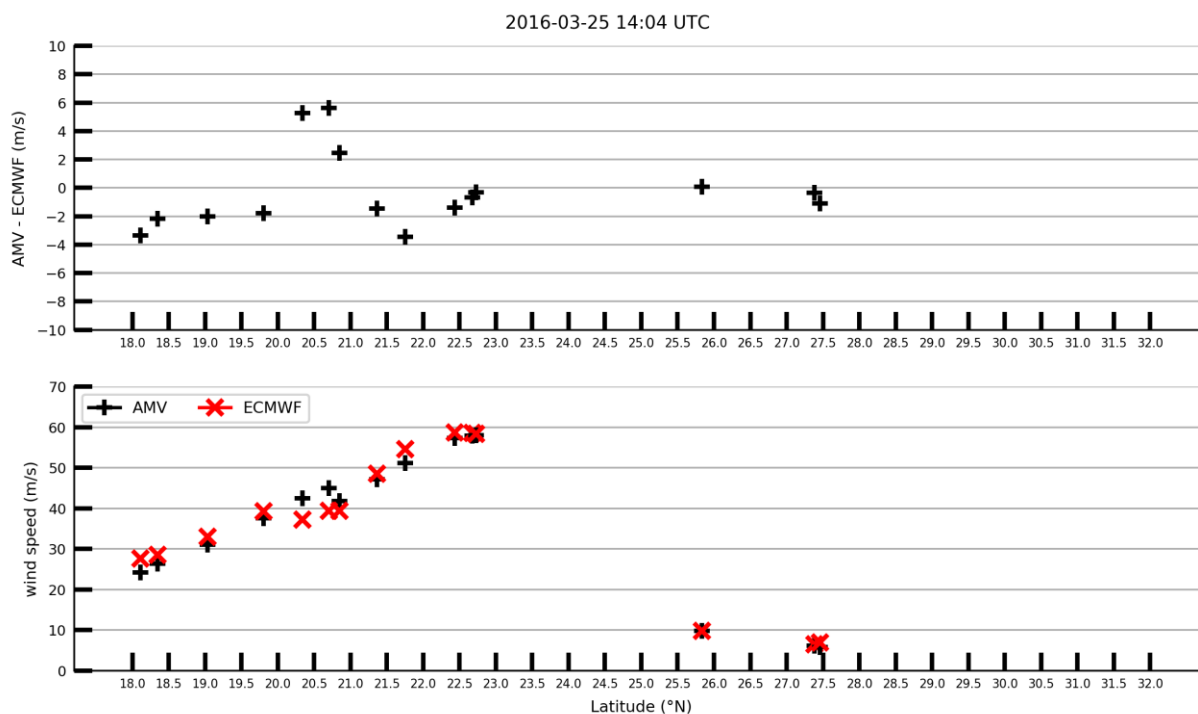



Figure 6.13 : Model wind vs Met10EUM AMVs during a CLOUDSAT overpass over the Sahara desert on 25 March, 14:04 UTC. (Upper panel): Wind speed differences between AMV and model winds interpolated to the AMV altitude. (Lower panel): Corresponding wind speed of AMV and model.

CLOUDSAT also provides cloud type classification. Figure 6.14 and Figure 6.15 provide these cloud classifications for the above presented north-south transects. High-level AMVs are derived for clouds classified by CLOUDSAT as cirrus or altostratus. From these two plots, no dependency of fast wind speed biases on cloud type can be deduced as they occur for both cloud types. We have repeated this analysis and have studied more north-south transects than the ones shown here. While fast wind speed biases are regularly present between 350 to 500 hPa, no correlation between cloud types was evident, i.e. there was no clear evidence that presence of fast (or too low) winds takes preferably place for one cloud type. Similar results were found for the presence of multilayer clouds. While certain fast wind speed biases coincide with presence of multilayer clouds, a clear dependency of the fast wind speed bias could not be deduced as in most cases the presence of multilayer clouds did not adversely affect the agreement model winds and AMV.

Overall, over the Saharan jet region, largest O-B speed biases occur at 350 to 500 hPa. These large speed biases coincides with largest pressure differences between AMV and CALIPSO/CALIOP (Figure 6.16). As wind speed increases strongly above 400 hPa, (positive) differences of 50-100 hPa translate to speed biases of $> 5 \text{ ms}^{-1}$ during jet situations over deserts.

	<p align="center">Study of AMV speed biases in the tropics</p> <p align="center">Final Report</p>	
Reference: AMV-TN-0008-TS_Ed1_Rev3	Date : 18/06/2020	Page : 74/118

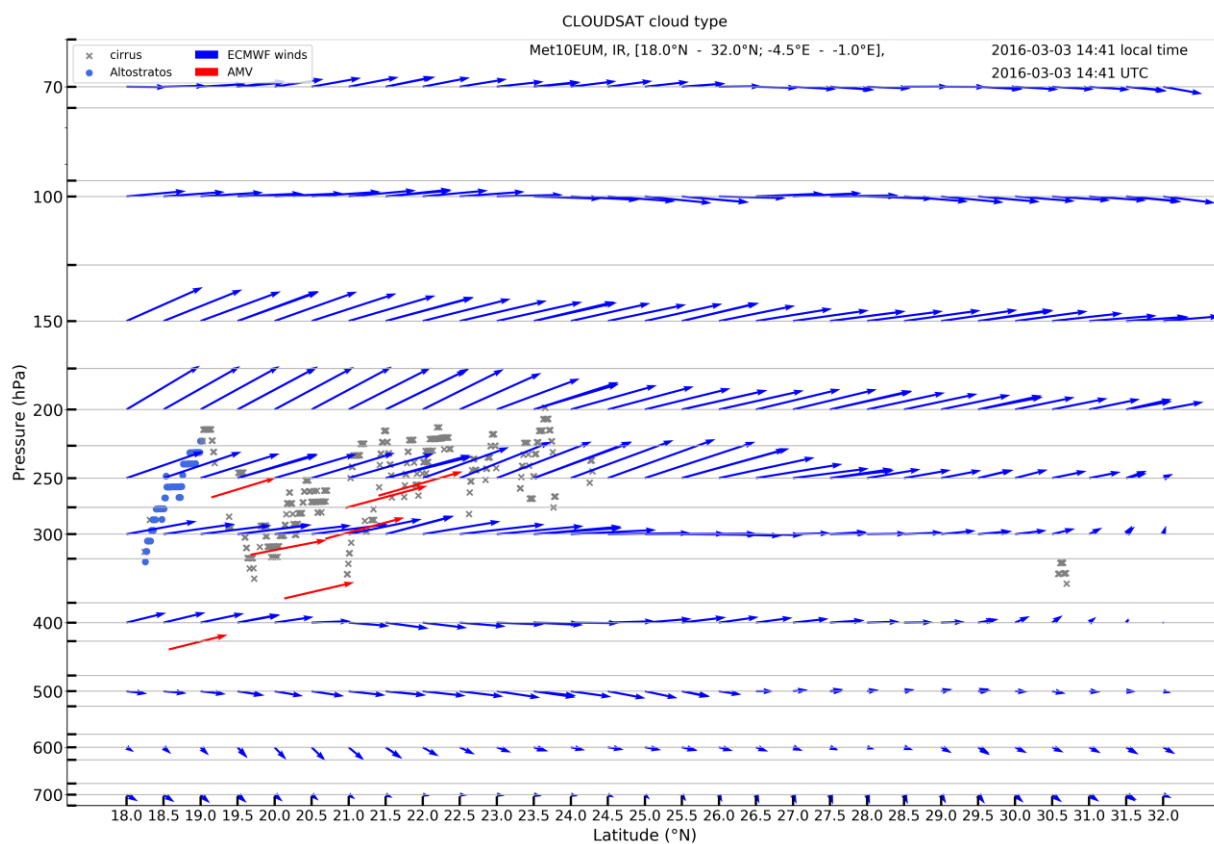



Figure 6.14 : Observed and model winds for a CLOUDSAT overpass over the Sahara desert on 3 March, 14:41 UTC. (Blue) ECMWF wind fields. (Red arrows) AMV obtained within $\pm 0.4^\circ$ latitude and $\pm 0.4^\circ$ longitude and ± 30 min of the CLOUDSAT overpass. (Grey and light blue symbols) Cloud type classification at top of cloud as given by CLOUDSAT. Numbers in the square bracket denote latitude and longitude information of the transect. Each ECMWF pressure level is surrounded by two grey lines, indicating the upper and lower limit of a $\Delta p \leq 25$ hPa collocation criterion used to derive mean statistics presented in Section 4.2.

	<p align="center">Study of AMV speed biases in the tropics</p> <p align="center">Final Report</p>	
Reference: AMV-TN-0008-TS_Ed1_Rev3	Date : 18/06/2020	Page : 75/118

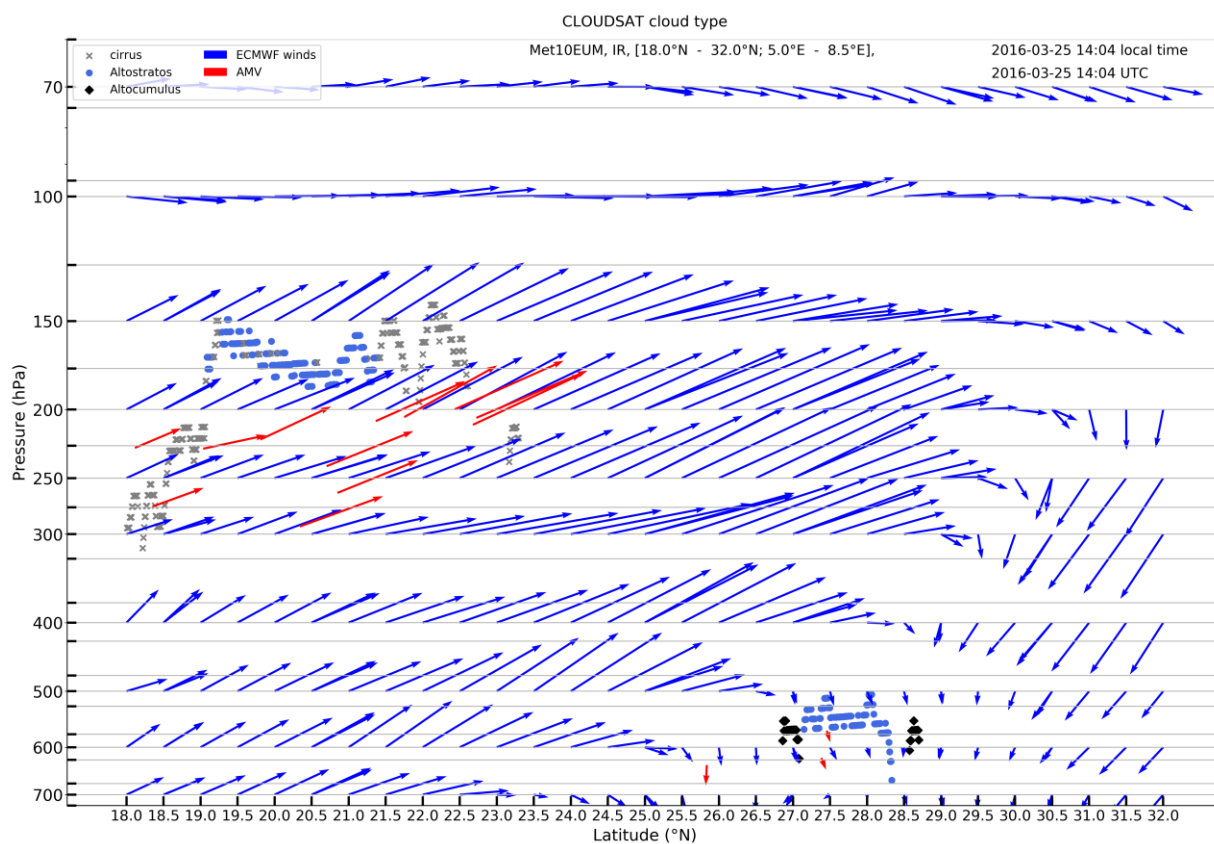



Figure 6.15 : Similar to Figure 6.14, but for a CLOUDSAT overpass over the Sahara desert on 25 March, 14:04 UTC.

	<p style="text-align: center;">Study of AMV speed biases in the tropics</p> <p style="text-align: center;">Final Report</p>	
Reference: AMV-TN-0008-TS_Ed1_Rev3	Date : 18/06/2020	Page : 76/118

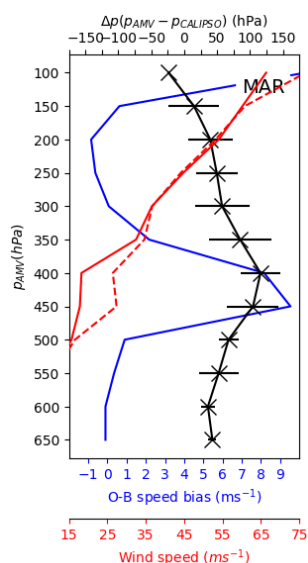



Figure 6.16 : Comparison of CALIPSO cloud top height with Met10EUM AMV for two weeks in March 2016 over Saharan desert [$18^{\circ}\text{N} < \text{latitude} < 32^{\circ}\text{N}$; -15°E , longitude $< 10^{\circ}\text{E}$]. (Black) Mean difference (Δp) between AMV pressure (p_{AMV}) and CALIPSO cloud top pressure (p_{CALIPSO}) and corresponding standard deviation. Corresponding O-B speed bias is shown in blue, while corresponding speed of model winds ECMWF and satellite winds are shown as solid red line and dashed red line, respectively. The method outlaid in Sec. 5.4 is used to collocate CALIPSO and AMVs and derive pressure differences over this region of interest.

	<p align="center">Study of AMV speed biases in the tropics</p> <p align="center">Final Report</p>	
Reference: AMV-TN-0008-TS_Ed1_Rev3	Date : 18/06/2020	Page : 77/118

6.2 METOP AMV PERFORMANCE OVER THE BOILER-BOX REGION

The monthly of Metop AMVs vs model wind speeds revealed a positive O-B speed bias along the equator for all months. For instance, these biases are typically $> 4 \text{ ms}^{-1}$ for the Boiler-Box over the Indonesian archipelago. This region is characterized by warm sea surface temperatures that provide ample moisture supply for deep convection (e.g. Smith, 2007), which typically appear as OLR minima (Figure 6.17).

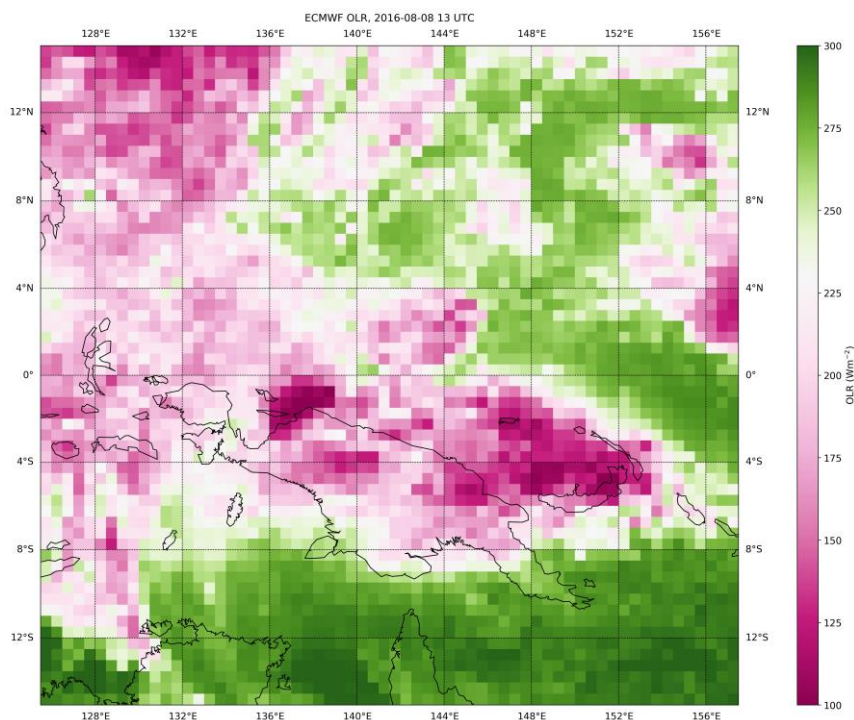



Figure 6.17 : Outgoing Longwave Radiation (OLR) in Wm^{-2} , computed from ECMWF fields over the Boiler-Box region on 8 August 2016, 13:00 UTC.

	<p align="center">Study of AMV speed biases in the tropics</p> <p align="center">Final Report</p>	
Reference: AMV-TN-0008-TS_Ed1_Rev3	Date : 18/06/2020	Page : 78/118

As no satellites flying in the A-train formation overpass the same region at similar time as Metop, CALIOP/CALIPSO or CPR/CLOUDSAT data cannot be used to verify if the altitudes assigned to Dual-Metop AMVs are correct. RAOB wind profiles were available as reference data. RAOB winds, together with Metop AMV and model winds are given in Figure 6.18 for a north-south transect during a Metop overpass on evening (local time).

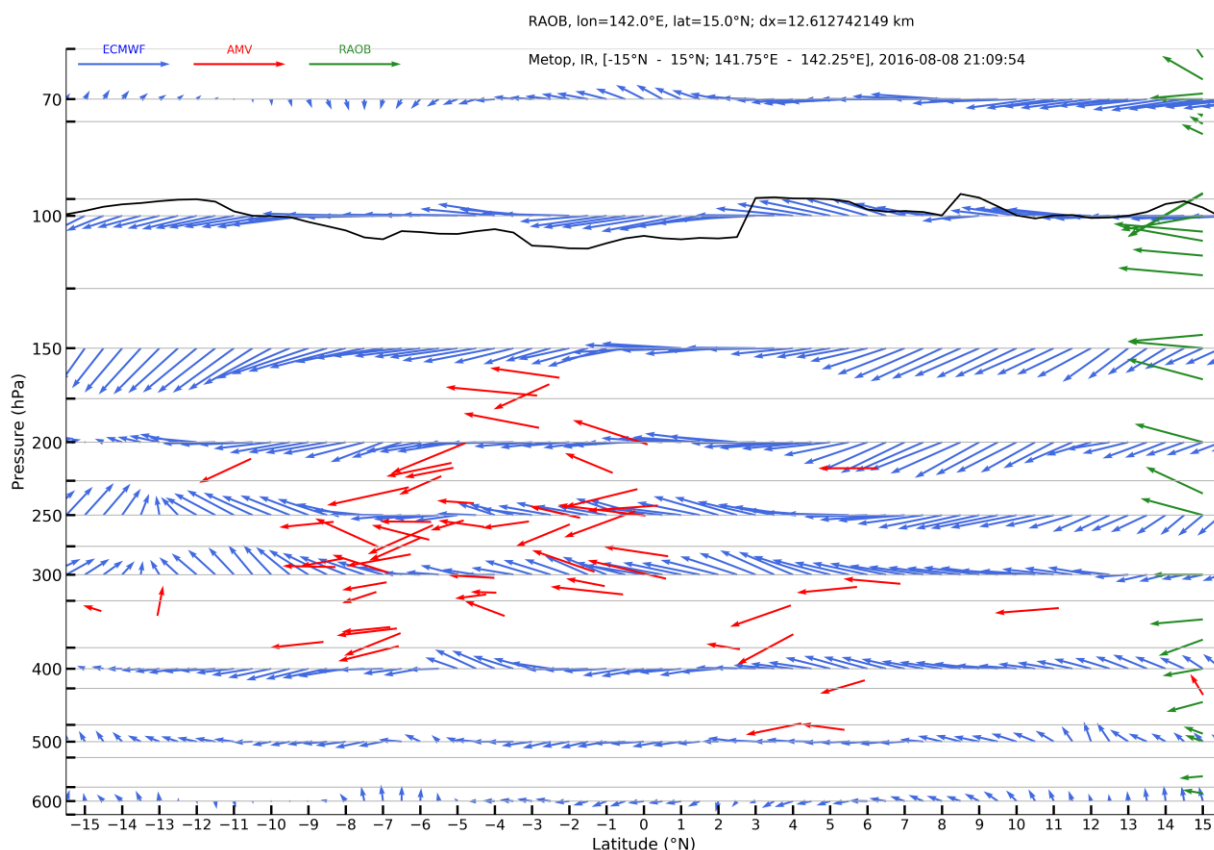


Figure 6.18 : North-south transect of Metop AMVs (red) and model winds (blue) for a Metop overpass at about 142°E on 8 March, 21:09 local time. Collocated RAOB wind data at 142°E, 15°N are plotted in green. The black solid line denotes the thermal tropopause calculated from high resolution ECMWF temperature fields (137 level resolution).

Apparent are the substantial differences between RAOB wind speeds and directions to both model and satellite winds. Little information is given on the quality of RAOB IGRA wind data. However, gross errors were removed as part of the quality procedures. These large differences in the wind field from the different datasets may be due to RAOB seeing motion on a different spatio-temporal scale than Metop or ECMWF. Other north-south transects of this Metop overpass are given in Figure 6.19 and Figure 6.20. These north-south transects reveal that Metop AMVs are faster than model winds at all altitudes. Compared to the jet situation over the Saharan desert (Section 6.1), wind direction change frequently with altitude, likely attributable to strong convection over the Boiler-Box (Figure 6.17). The larger size of the considered region and thus the large number of AMVs further renders visual checking of the agreement between ECMWF and Metop to evaluate height assignment errors difficult. In order to verify if the height assignment is correct, we evaluate the best-fit pressure using the method outlined in Salonen

et al. (2015) but without searching for a second or a very broad minimum as we just aim a quick overlook to which ECMWF pressure level AMVs fit best. Even when compared to the best-fit level, few AMVs agree with model wind speeds and directions. Hence, erroneous AMV altitudes unlikely explain the observed discrepancies in the wind fields of the two datasets.

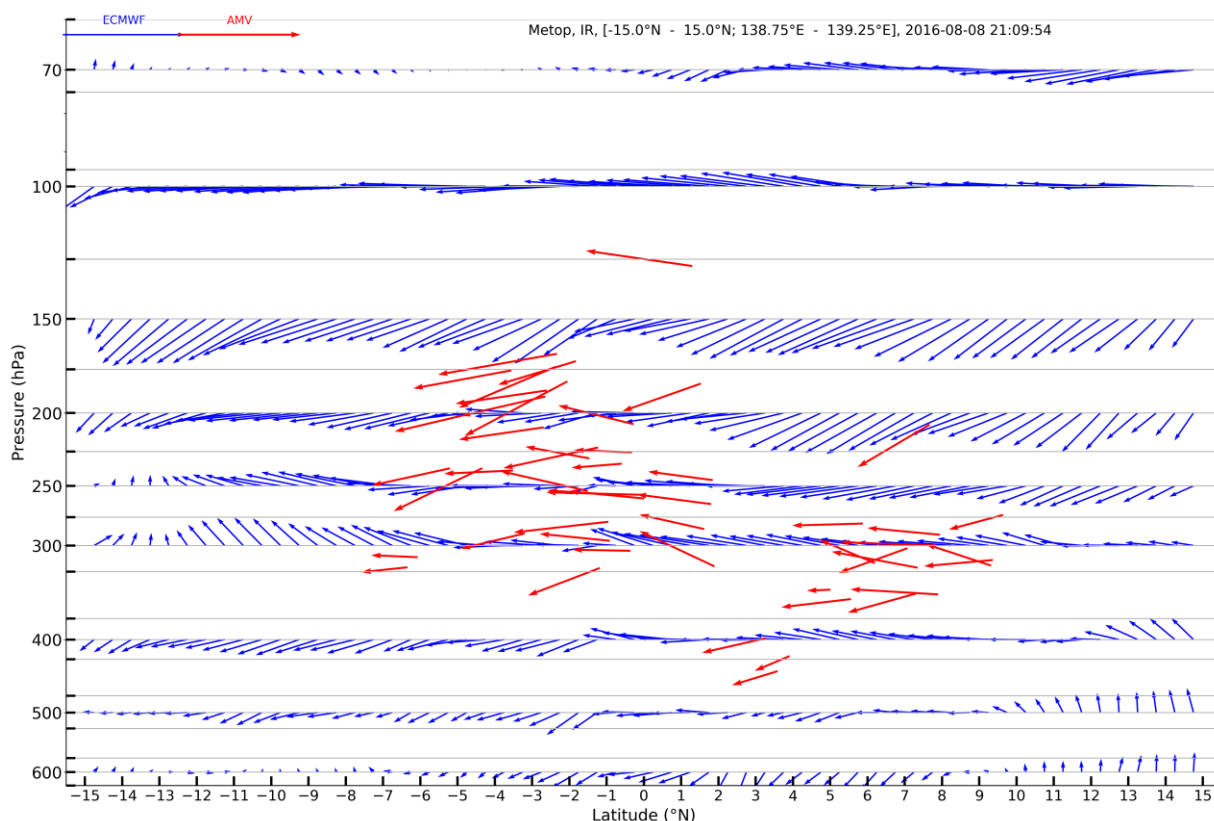



Figure 6.19 : North-south transect of Metop AMVs (red) and model winds (blue) for a Metop overpass at about 139°E on 8 March, 21:09 local time.

	<p align="center">Study of AMV speed biases in the tropics</p> <p align="center">Final Report</p>	
Reference: AMV-TN-0008-TS_Ed1_Rev3	Date : 18/06/2020	Page : 80/118

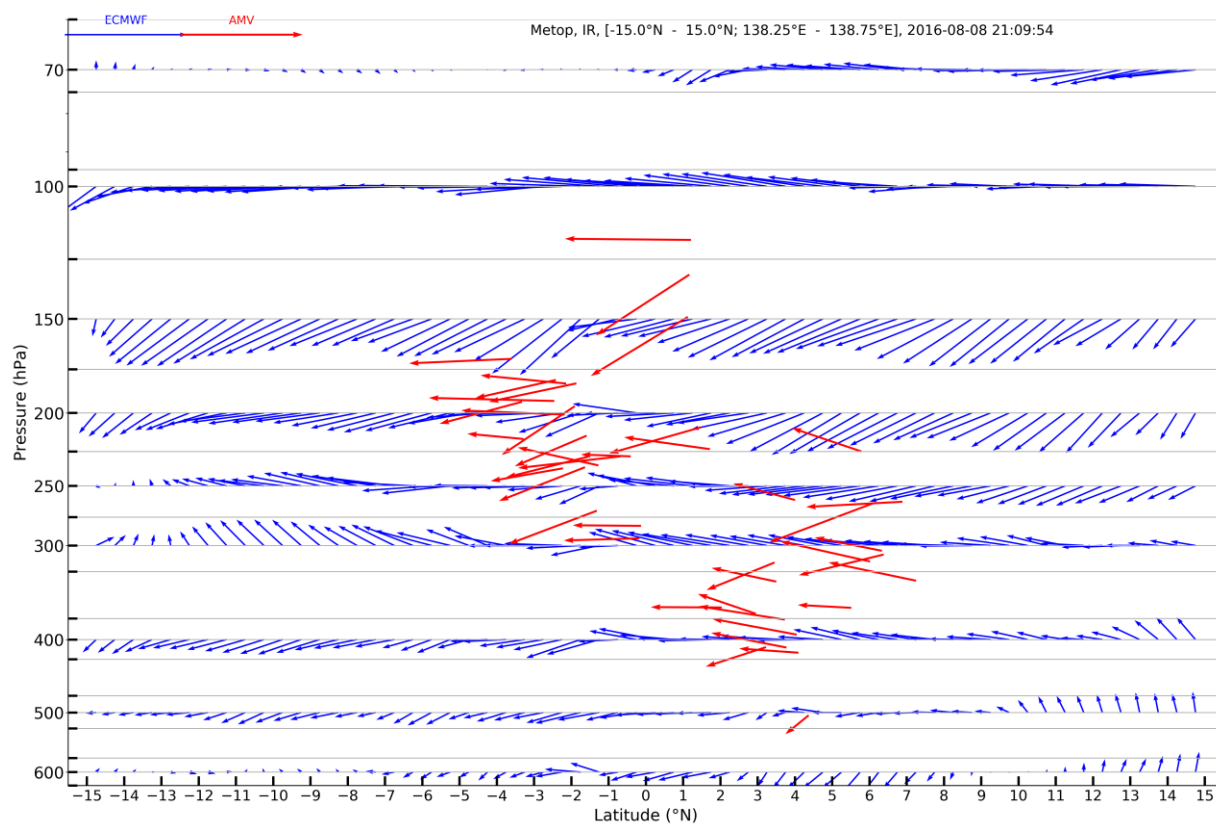



Figure 6.20 : North-south transect of Metop AMVs (red) and model winds (blue) for a Metop overpass at about 138.5°E on 8 March, 21:09 local time.

	<p align="center">Study of AMV speed biases in the tropics</p> <p align="center">Final Report</p>	
Reference: AMV-TN-0008-TS_Ed1_Rev3	Date : 18/06/2020	Page : 81/118

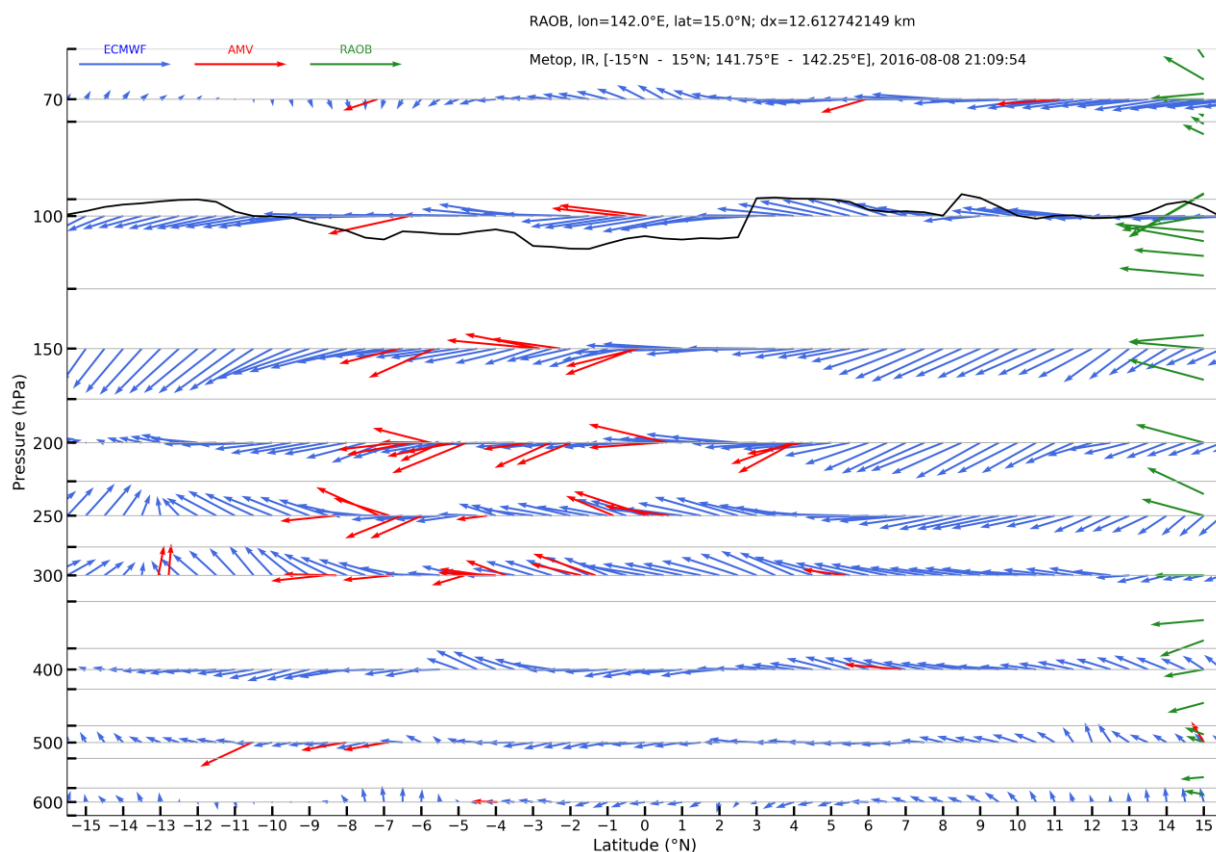



Figure 6.21 : North-south transect of Metop AMVs (red) and model winds (blue) for a Metop overpass at about 142°E on 8 March, 21:09 local time. Similar to Figure 6.18, but model winds are plotted against the best-fit pressure, which are assigned to AMVs (see text).

North-south transects over the Boiler-Box region for a Metop overpass during morning (local time) are given in Figure 6.22 and Figure 6.23. Particularly intriguing is the area north of 10°N, as wind differences are about 90° and no visual (or qualitative) agreement between satellite wind and model wind can be achieved by moving concerned AMVs up or down.

	<p align="center">Study of AMV speed biases in the tropics</p> <p align="center">Final Report</p>	
Reference: AMV-TN-0008-TS_Ed1_Rev3	Date : 18/06/2020	Page : 82/118

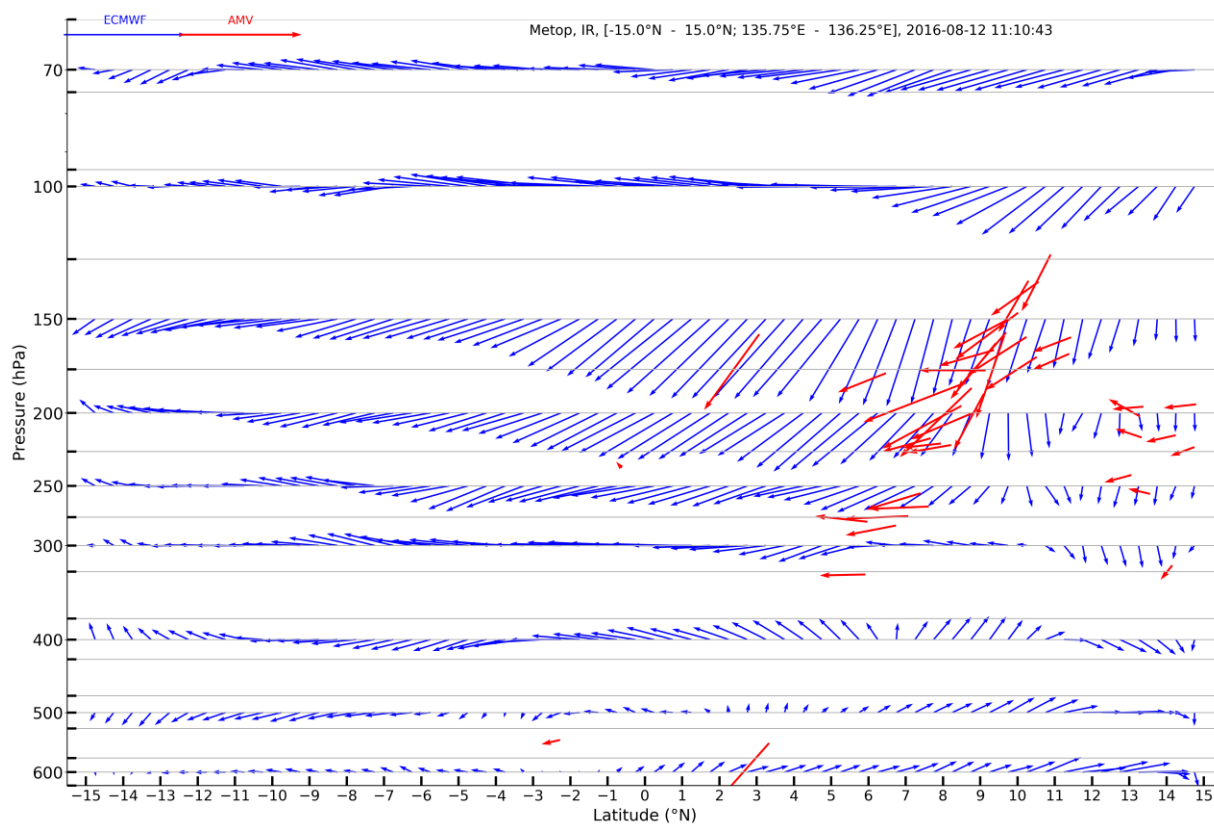



Figure 6.22 : North-south transect of Metop AMVs (red) and model winds (blue) for a Metop overpass at about 136°E on 12 March, 11:10 local time.

	<p align="center">Study of AMV speed biases in the tropics</p> <p align="center">Final Report</p>	
Reference: AMV-TN-0008-TS_Ed1_Rev3	Date : 18/06/2020	Page : 83/118

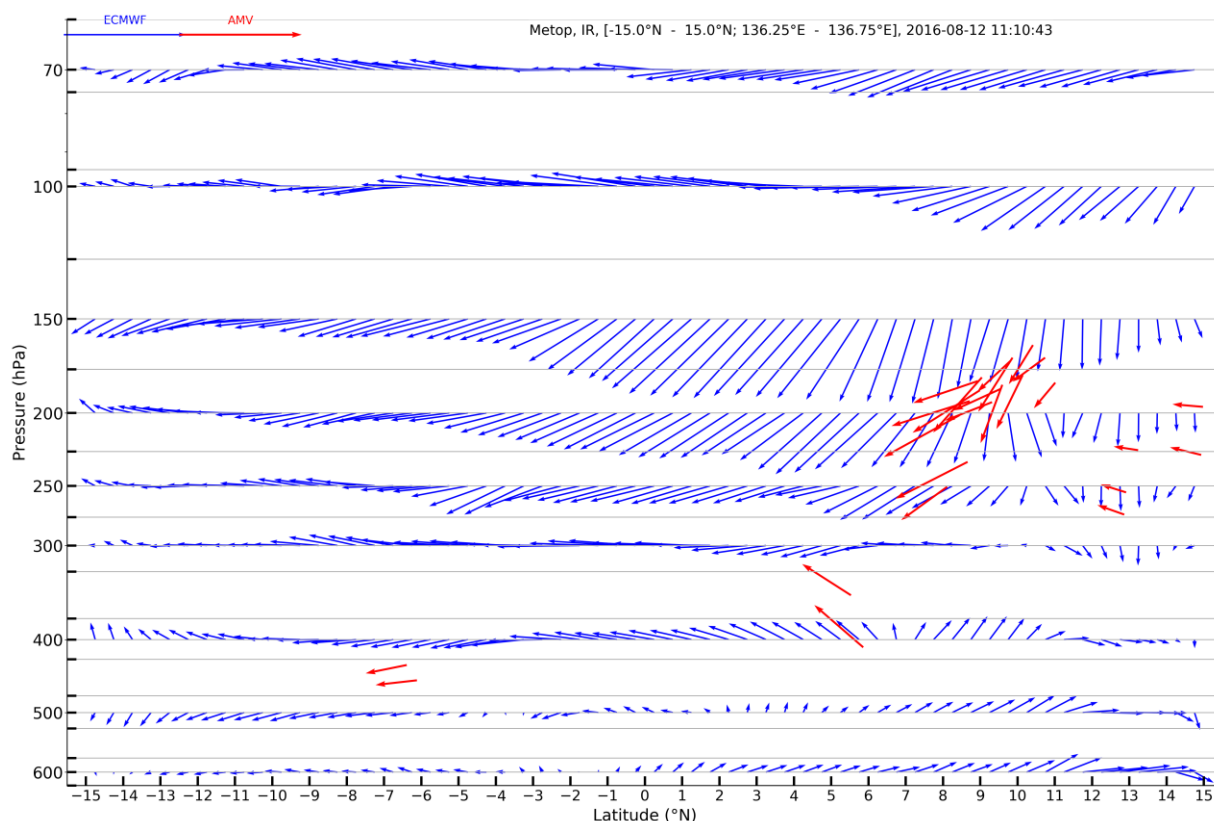



Figure 6.23 : North-south transect of Metop AMVs (red) and model winds (blue) for a Metop overpass at about 136.5°E on 12 March, 11:10 local time.

The quality and representativeness of AMVs is related to the used target size and image frequency, the size and lifetime of the selected feature and proper identification of the cloud top height. Assuming that model winds are correct, height assignment errors alone cannot explain these obtained wind field discrepancies. Hence, the question arises to what motion Metop AMVs over the Boiler-Box region are representing. Several studies have investigated the relationship between tracer size, temporal gap and the impact of the wind guess in tracking step of the AMV extraction on AMV quality and representativeness (see Garcia-Pereda and references therein). For instance, it was found that winds derived using a small target window represent rather motion on local scale, while larger target windows reflect mean synoptic-scale motion.

To extract AMVs from Metop A/B image pairs, a target box of 30 km x 30 km (about 0.3° latitude x 0.3° longitude box in the tropics) is utilised. IR counts and derived brightness temperatures from the morning and evening Metop overpasses presented above are given Figure 6.24-Figure 6.25 and Figure 6.26-Figure 6.27, respectively. These figures indicate that, due to the strong convection that alters the shape of clouds and due to the long temporal gap of about 50 min, the feature to be tracked is difficult to relate between two images pairs. Furthermore, the differences in brightness temperatures between two images indicate a relatively low correlation between the pixels (see Figure 6.28).

	<p align="center">Study of AMV speed biases in the tropics</p> <p align="center">Final Report</p>	
Reference: AMV-TN-0008-TS_Ed1_Rev3	Date : 18/06/2020	Page : 84/118

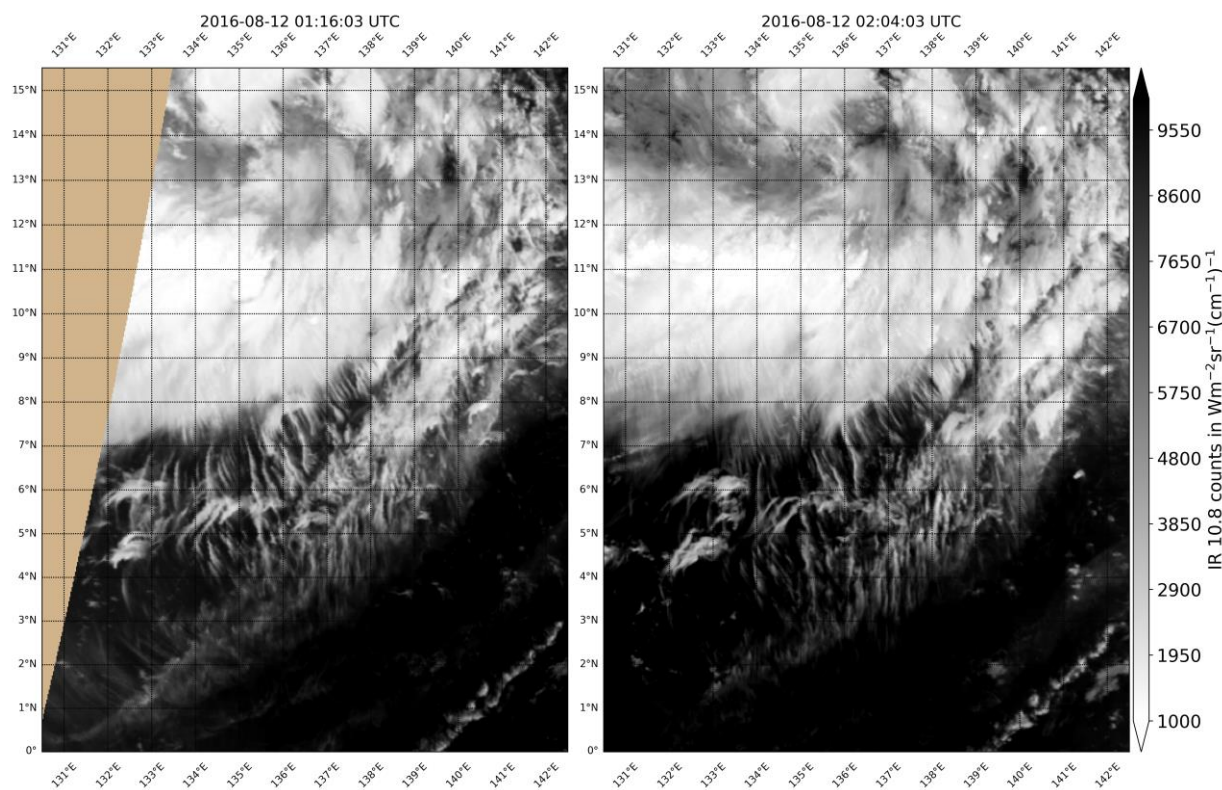



Figure 6.24 : AVHRR IR counts for the Metop image pairs, used in the algorithm to extract the AMVs displayed in Figure 6.22 and Figure 6.23 (morning overpass).

	<p align="center">Study of AMV speed biases in the tropics</p> <p align="center">Final Report</p>	
Reference: AMV-TN-0008-TS_Ed1_Rev3	Date : 18/06/2020	Page : 85/118

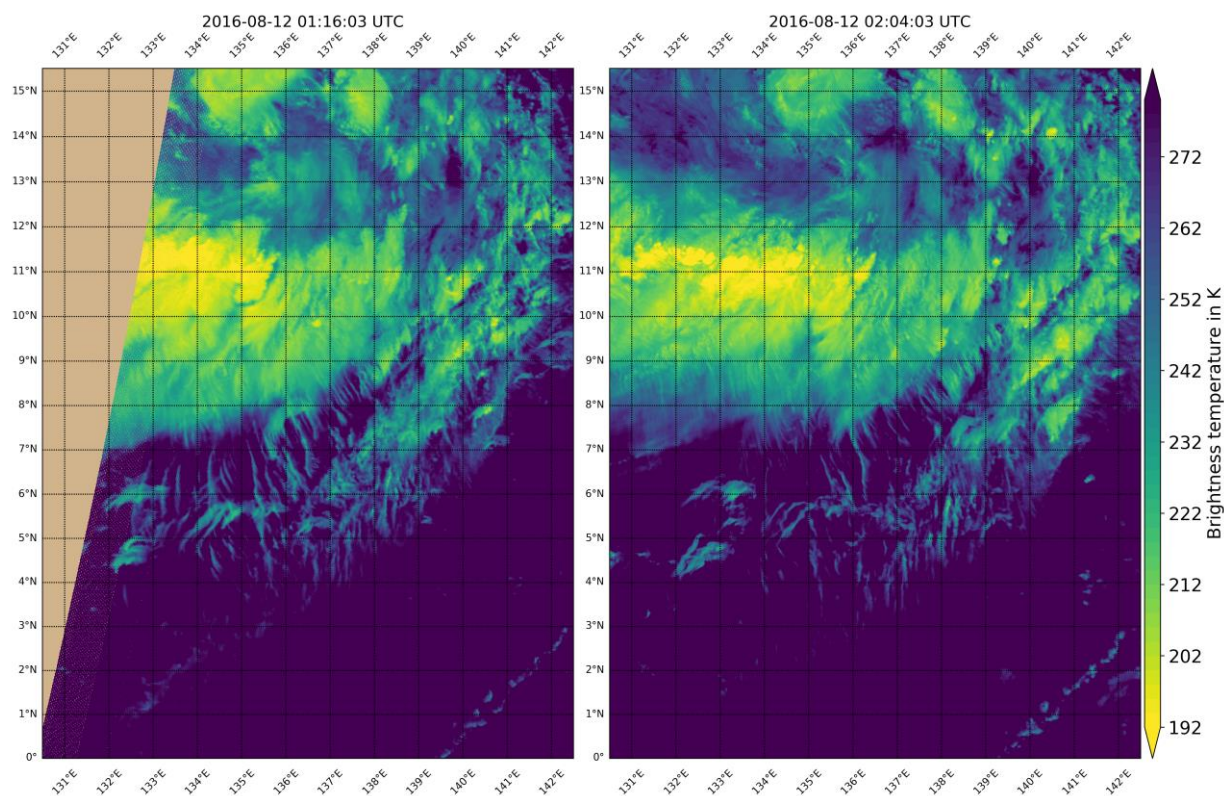



Figure 6.25 : Brightness temperature (TB) fields derived from AVHRR IR counts. TB is plotted for the Metop image pairs, used in the algorithm to extract the AMVs displayed in Figure 6.22 and Figure 6.23 (morning overpass).

	<p align="center">Study of AMV speed biases in the tropics</p> <p align="center">Final Report</p>	
Reference: AMV-TN-0008-TS_Ed1_Rev3	Date : 18/06/2020	Page : 86/118

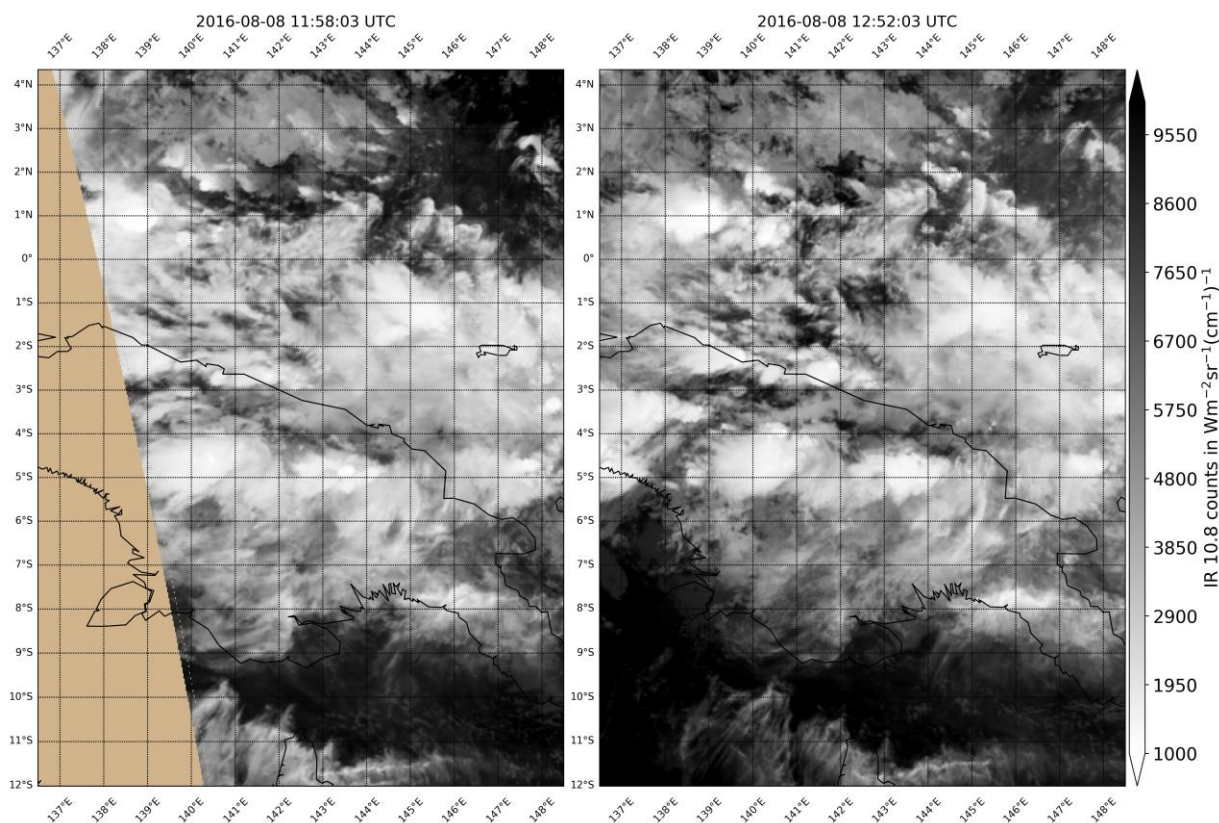



Figure 6.26 : AVHRR IR counts for the Metop image pairs, used in the algorithm to extract the AMVs displayed in Figure 6.18 to Figure 6.20 (evening overpass).

	<p align="center">Study of AMV speed biases in the tropics</p> <p align="center">Final Report</p>	
Reference: AMV-TN-0008-TS_Ed1_Rev3	Date : 18/06/2020	Page : 87/118

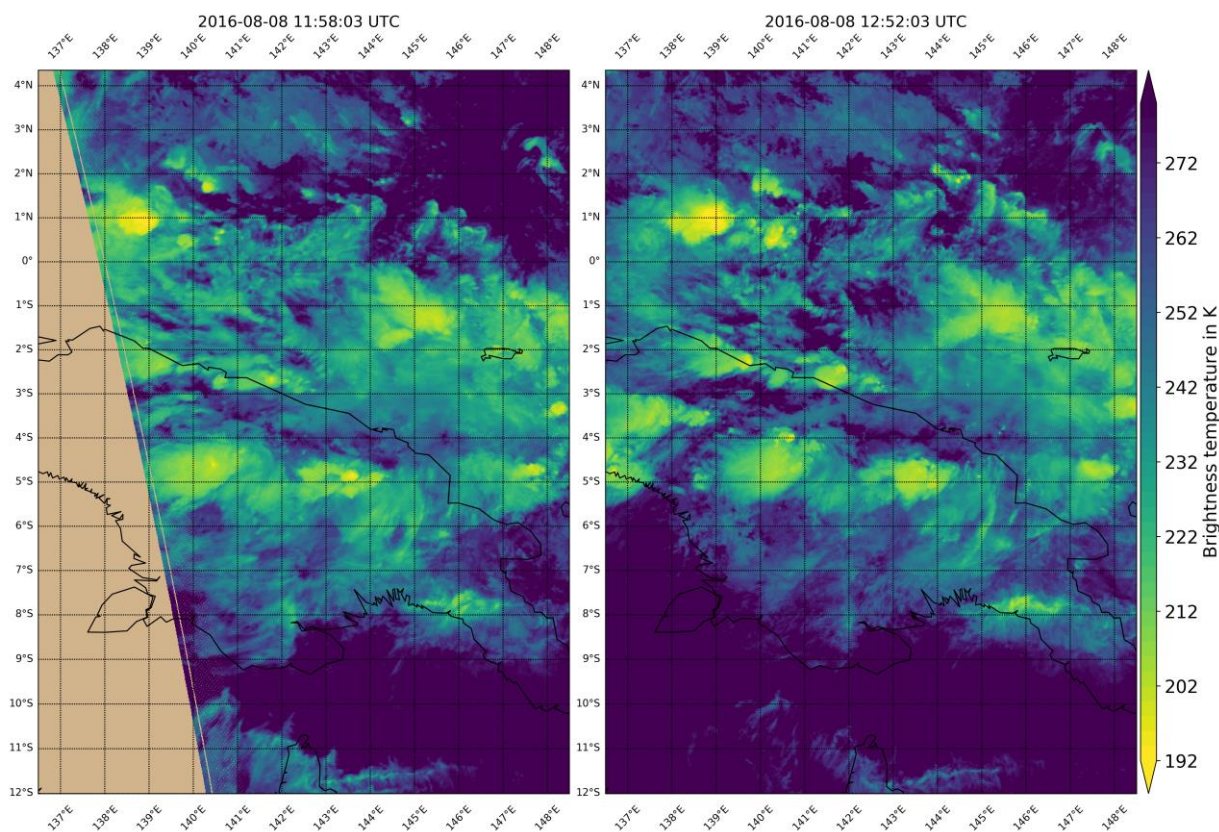



Figure 6.27 : Brightness temperature (TB) fields derived from AVHRR IR counts. TB is plotted for the Metop image pairs, used in the algorithm to extract the AMVs displayed in Figure 6.18 to Figure 6.20 (evening overpass).

	<p align="center">Study of AMV speed biases in the tropics</p> <p align="center">Final Report</p>	
Reference: AMV-TN-0008-TS_Ed1_Rev3	Date : 18/06/2020	Page : 88/118

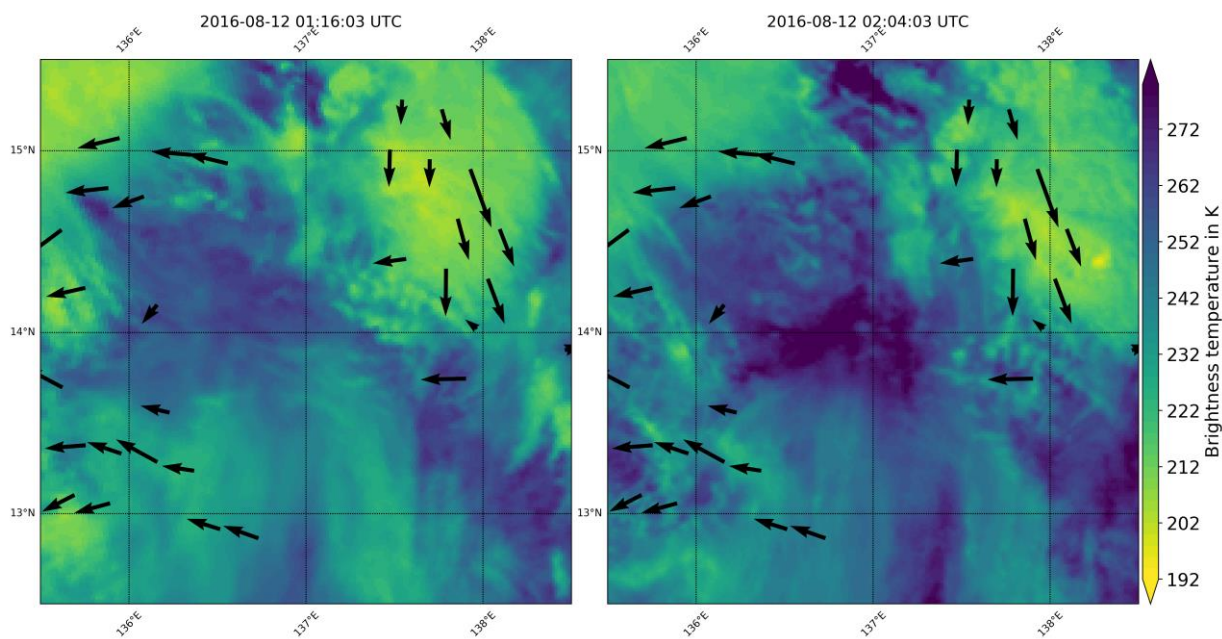



Figure 6.28 : Zoom to the brightness temperature field displayed in Figure 6.25. Note the different scale for the brightness temperature compared to Figure 6.25 and Figure 6.27. Dual-Metop AMVs, derived from this image pair, are shown as black arrows.

	<p align="center">Study of AMV speed biases in the tropics</p> <p align="center">Final Report</p>	
Reference: AMV-TN-0008-TS_Ed1_Rev3	Date : 18/06/2020	Page : 89/118

7 COMPARISON TO WIND PROFILES FROM ADM-AEOLUS

7.1 DATA AND METHODS

7.1.1 Data availability and screening


We use version L2B v3.20 of ADM-Aeolus data. Due to the period covered by this ADM-Aeolus data set, comparison of AMVs to wind-component profiles measured by the Atmospheric LAser Doppler INstrument (ALADIN) aboard the ADM-Aeolus mission is limited to 1 October to 17 November 2019. This period further renders any comparison of ADM-Aeolus to AMV derived from images from Meteosat-10 and Meteosat-7 impossible. AMVs derived by EUMETSAT from Meteosat-11 and Meteosat-8 images are used instead. Since ADM-Aeolus crosses the equator at 6 am local time (descending node of orbit) and 6 pm local time (ascending node of orbit), no comparison to Dual-Metop AMVs is possible within a reasonable temporal matching criterion (equator crossing time of 9:30 local time). In order to compare high quality AMVs to HLOS winds from ADM-Aeolus, the QI assigned to Meteosat-11 and Meteosat-9 AMVs must exceed a value of 80, which is precisely the same value used for AMVs derived from geostationary satellites as in the previous tasks (see for instance Section 4.1).

The ALADIN instrument is designed to probe the lowermost 30 km of the atmosphere by its molecular (Rayleigh) and particle (Mie) channels to provide profiles of wind, aerosols and clouds along the satellite's orbital path. The wind information of ADM-Aeolus is the horizontal line-of-sight (HLOS) component, i.e. the wind component in the direction perpendicular to the satellite's velocity. We use the Level 2B ADM-Aeolus data in bufr format, which comprise geo-located consolidated HLOS wind observations after application of actual atmospheric corrections to Rayleigh channel data. ECMWF geopotential heights are used to convert ADM-Aeolus heights to pressure. Finally, ADM-Aeolus data are screened according to the criteria given in Table 7.1 to ensure high data quality.

Table 7.1 : Quality criteria applied to HLOS winds from ADM-Aeolus.

Criteria regarding height	The height difference between the Top and the Bottom observation level shall be greater than 300 m.
	The height above the surface shall be greater than 250 m
Validity of HLOS winds	Only valid winds are considered, i.e. the field confidence flag must be 0 in the bufr file.
Quality of HLOS winds	<p>For the Mie-channel and data classified as cloud, only data where the error is < 5 m/s are considered.</p> <p>Likewise, for the Rayleigh channel and data classified as clear sky, for pressure < 200 hPa only data with an error < 12 m/s are considered. For pressure ≥ 200 hPa, only data with an error < 8.5 m/s are considered.</p>

The Level-2B HLOS winds are averaged over a certain length-scale. Figure 7.1 shows the cumulative histogram of horizontal integration length in October 2019 over the tropics (latitude ≤ 35°), separated for

	<p align="center">Study of AMV speed biases in the tropics</p> <p align="center">Final Report</p>	
Reference: AMV-TN-0008-TS_Ed1_Rev3	Date : 18/06/2020	Page : 90/118

Mie/Cloudy and Rayleigh/clear data. In order to be able to use at least 50% of the data, we chose a minimum integration length of 80 km for the Rayleigh/clear case and 10 km for the Mie/cloudy case.

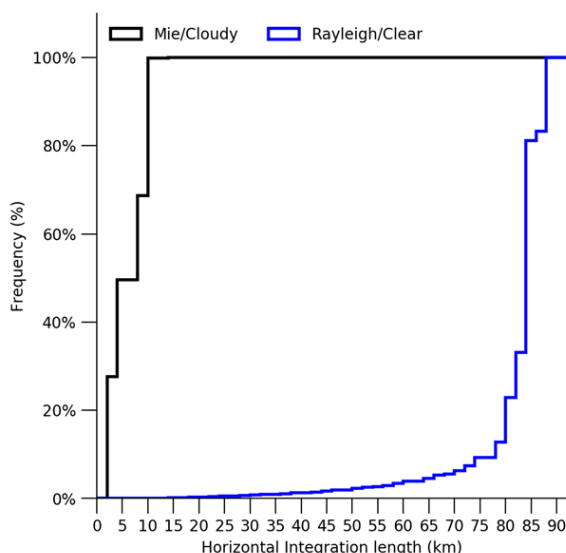


Figure 7.1 : Cumulative frequency of horizontal integration length for Mie and Rayleigh channel in October 2019 in the tropics ($35^{\circ}\text{S} < \text{latitude} < 35^{\circ}\text{N}$).

7.1.2 HLOS forward model

The basic forward model to form HLOS winds from the horizontal vector wind (u, v) is: $\text{HLOS}_{\text{wind}} = -u \cdot \sin(\alpha) - v \cdot \cos(\alpha)$, where α denotes the line-of-sight azimuth angle of ADM-Aeolus. Note, in this formula, the vertical wind component is not included as it is not part of the AMV extraction algorithm. HLOS winds can be positive or negative. For instance, a westerly wind will be negative for descending and positive for ascending orbits in the Aeolus L2B wind product.

7.1.3 Collocation criteria

For the comparison of AMVs to ECMWF winds and reference observations (Section 4.1), we allowed a temporal separation of maximal 1.5 hours. However, as AMVs are extracted approximately every 15 minutes from images by geostationary Meteosat satellites, a much tighter temporal collocation criterion can be used to compare HLOS winds from the polar orbiting ADM-Aeolus mission to AMVs. Figure 7.2 reveals that with a temporal collocation criterion of 15 minutes and horizontal separation of less than 50 km, the altitudes to which AMVs are set agree mostly better than 25 hPa of the altitude of collocated ADM-Aeolus winds, even if winds are obtained over desertic areas, where height assignment errors can be found frequently. However, in order to increase the sample size of collocations, we increase the spatio-temporal collocation criteria to 100 km and 30 min. The vertical separation criterion is kept at 15 hPa. While this increased match radius certainly leads to slightly different comparison statistics, it does not change the overall results and interpretation of the comparison study. In addition, if more the one ADM-Aeolus HLOS wind component matches an AMV, the HLOS wind minimising the pressure difference to the AMV altitude is considered.

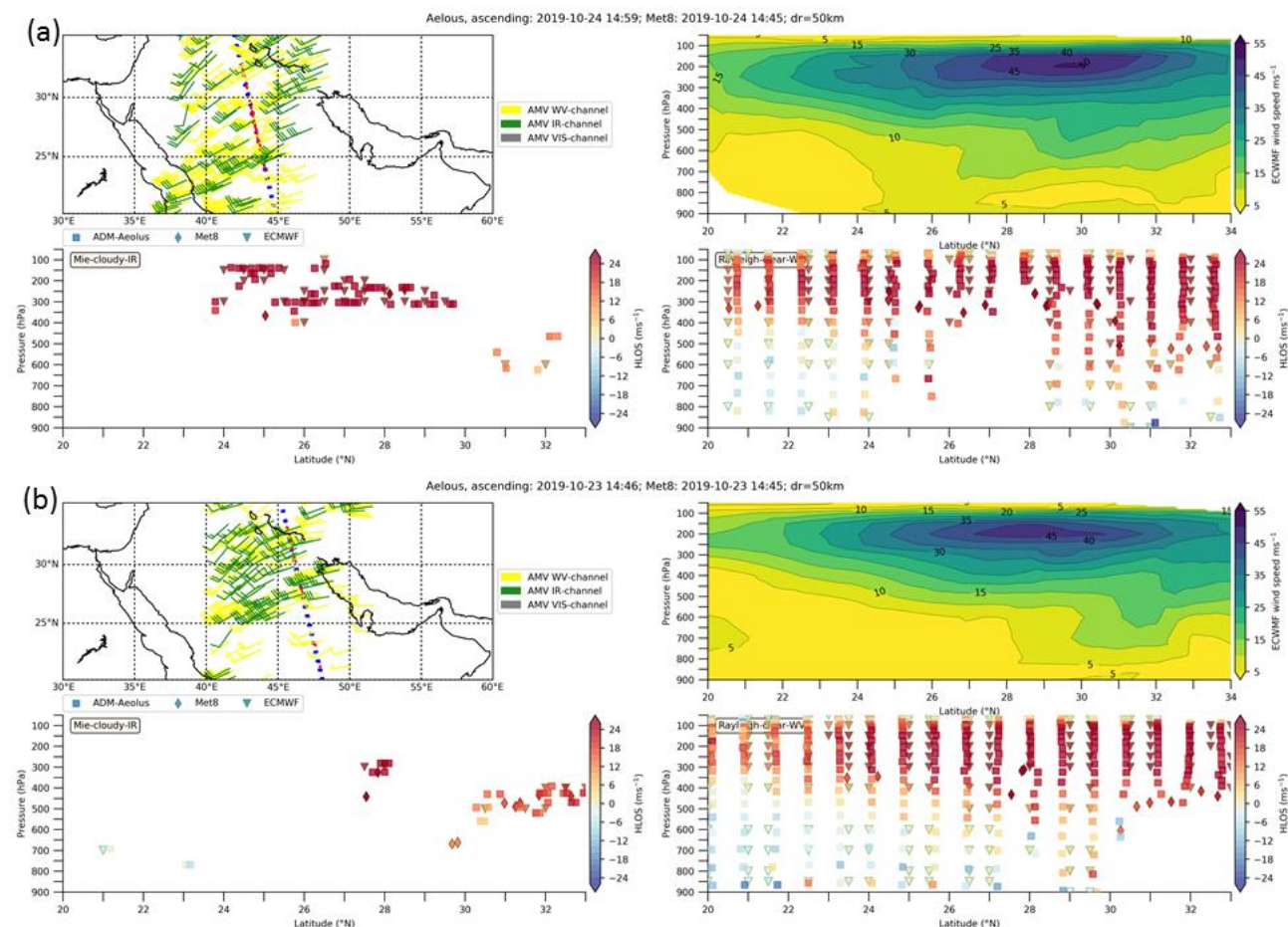



Figure 7.2 : Wind situation along two ADM-Aeolus orbits over Arabia. (a) ADM-Aeolus passes (ascending orbit) over Arabia on 24 October 2019 at 14:59 UTC. (b) ADM-Aeolus passes (ascending orbit) over Arabia on 23 October 2019 at 14:46 UTC. (Upper panel, left) Red point indicate ADM-Aeolus data from Mie channel, while blue points indicate data from Rayleigh channel. Collocated AMVs from Meteosat-8 are displayed as yellow (WV channel), green (IR) and grey (VIS) arrows. (Upper panel, right). ECMWF wind speeds along ADM-Aeolus orbit. (Lower panel, left). HLOS wind speed from collocated ADM-Aeolus (Mie channel), ECMWF and Meteosat-8 (IR channel) as function of pressure. (Lower panel, right). HLOS wind speed from collocated ADM-Aeolus (Rayleigh channel), ECMWF and Meteosat-8 (WV channel) as function of pressure.

7.2 COMPARISON STATISTICS

7.2.1 Mean statistics

Mie-cloudy-IR collocated data: Scatterplots of HLOS winds from ADM-Aeolus Mie channel against HLOS winds from Meteosat-8 and Meteosat-11 IR channel during October 2019 are given in Figure 7.3. Corresponding mean of HLOS speed differences ($HLOS_{ADM} - HLOS_{AMV}$), standard deviation and correlation coefficient are also shown. Results for both Meteosat satellites are similar; with both satellites

	Study of AMV speed biases in the tropics Final Report	
Reference: AMV-TN-0008-TS_Ed1_Rev3	Date : 18/06/2020	Page : 92/118

reporting mostly slightly faster (0.05 to 0.64 ms^{-1}) HLOS winds than ADM-Aeolus. For both satellites, the agreement with ADM-Aeolus is better for high-level levels than for low-level winds.

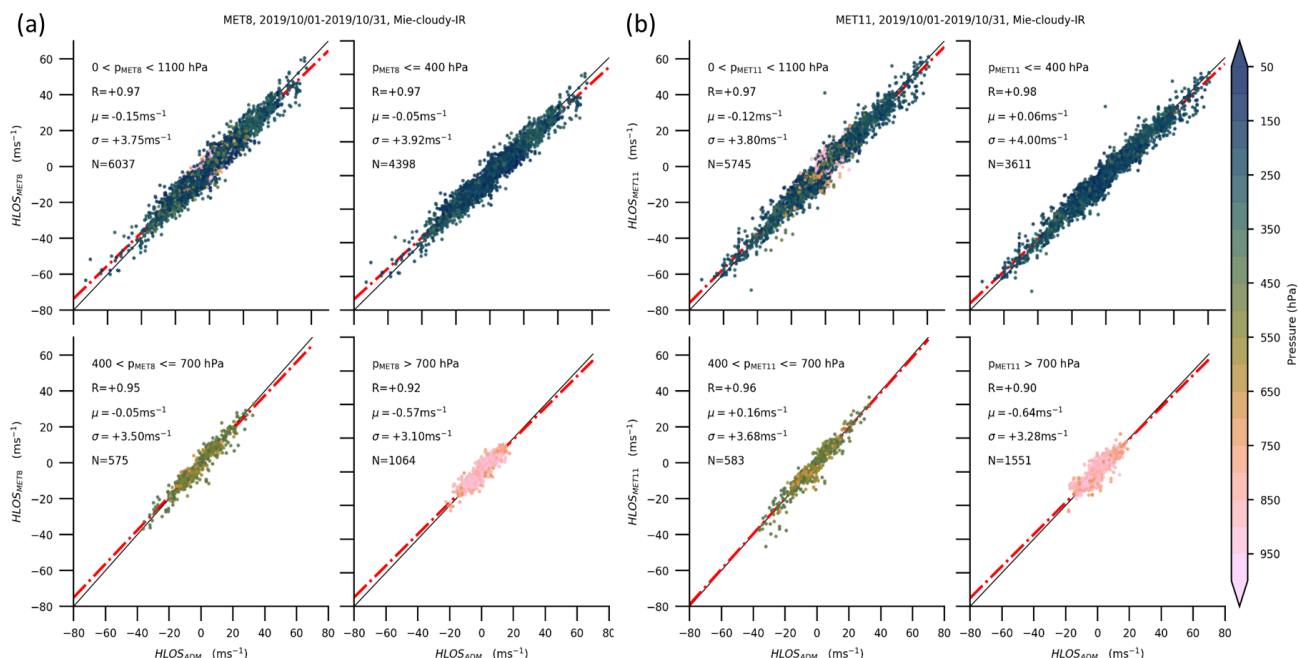



Figure 7.3 : Scatterplots of HLOS winds from Mie-channel ADM-Aeolus data ($HLOS_{ADM}$) against HLOS winds derived from (a) Meteosat-8 and (b) Meteosat-11 IR AMVs.

Rayleigh-clear-WV collocated data: Scatterplots of HLOS winds from ADM-Aeolus Rayleigh-channel against WV AMV from Meteosat-8 and Meteosat-11 are given in Figure 7.4. We use AMV wind speed data from all WV channels decoded in the bufr file (wind derived from cloud motion observed in the water vapour channel, wind derived from motion observed in the water vapour channel in clear air, wind derived from motion observed in water vapour channel (cloud or clear air not specified)). In contrast to IR AMV, no low tropospheric WV AMVs could be compared to ADM-Aeolus. For mid- to high-level winds, more collocations of WV AMVs to ADM-Aeolus are obtained compared to the Mie-IR case (compare Figure 7.4 to Figure 7.3). Mean HLOS speed differences ($HLOS_{ADM} - HLOS_{AMV}$) range from -0.42 ms^{-1} (high-level, Meteosat-8) to -1.40 ms^{-1} (mid-level, Meteosat-8), which is an about 0.5 to 1 ms^{-1} higher bias than for the Mie/IR dataset. This higher bias goes hand in hand with $2\text{-}3 \text{ ms}^{-1}$ larger standard deviation.

	<p align="center">Study of AMV speed biases in the tropics</p> <p align="center">Final Report</p>	
Reference: AMV-TN-0008-TS_Ed1_Rev3	Date : 18/06/2020	Page : 93/118

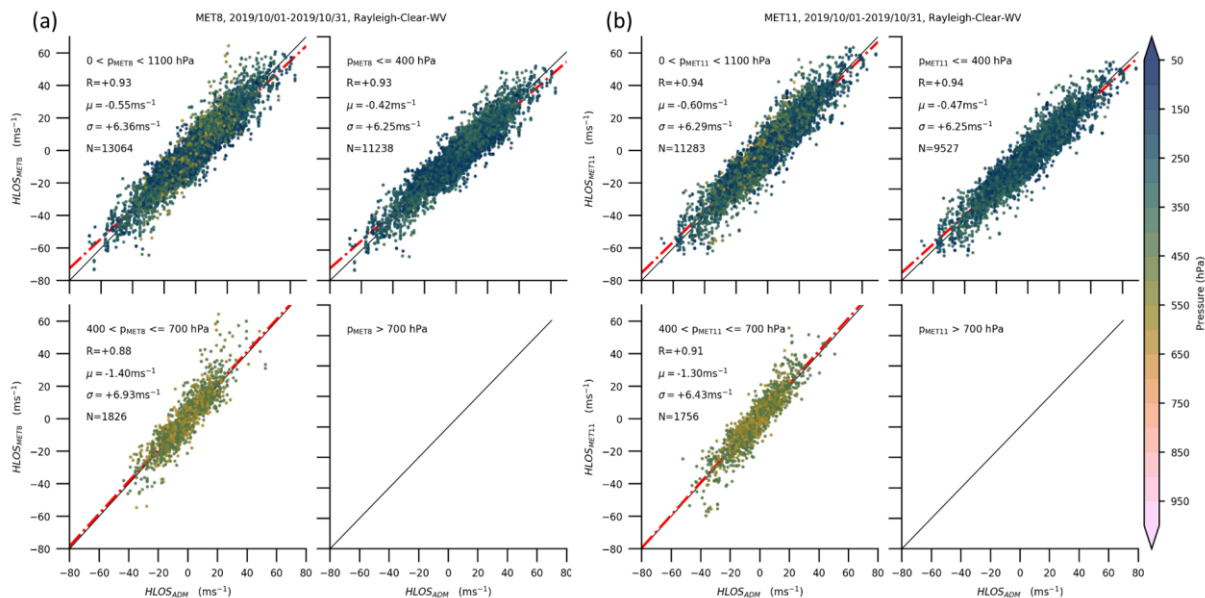



Figure 7.4 : Scatterplots of HLOS winds from Rayleigh-channel ADM-Aeolus data ($HLOS_{ADM}$) against HLOS winds derived from (a) Meteosat-8 and (b) Meteosat-11 WV AMVs.

Lastly, in order to complete our comparison of HLOS winds to various AMV-channel combinations, HLOS winds from the ADM-Aeolus Mie channel are compared against VIS AMV from Meteosat-8 and Meteosat-11. Apparent are the lack of comparison data for high- and mid-level winds, which may can be explained by the fact that ADM-Aeolus reports wind profiles above the cloud top, which is not necessary the case for VIS AMV. In addition, VIS AMV can only be extracted during daylight, which drastically reduces the sample size. The low-level HLOS derived from both Meteosat satellites agree well to ADM-Aeolus winds. Mean differences $HLOS_{ADM} - HLOS_{AMV}$ of less than 0.22 ms^{-1} are reported, with the standard deviation ranging between 2.65 ms^{-1} and 3.71 ms^{-1} .

	<p align="center">Study of AMV speed biases in the tropics</p> <p align="center">Final Report</p>	
Reference: AMV-TN-0008-TS_Ed1_Rev3	Date : 18/06/2020	Page : 94/118

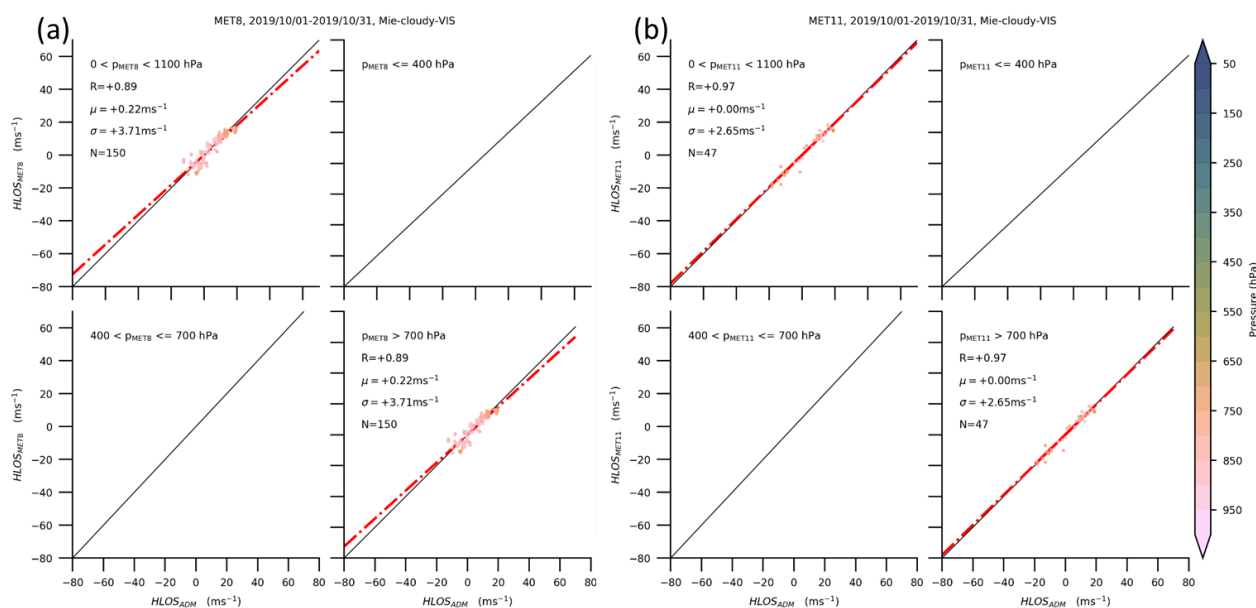


Figure 7.5 : Scatterplots of HLOS winds from Mie-channel ADM-Aeolus data ($HLOS_{ADM}$) against HLOS winds derived from (a) Meteosat-8 and (b) Meteosat-11 VIS AMVs.

7.2.2 Ascending vs descending orbit

The previous analysis did not discern between ascending and descending orbit. In Figure 7.6 and Figure 7.7, we split obtained results for IR and WV channel into results for ascending and descending orbit, respectively. While there is little difference in obtained bias and corresponding standard deviation of HLOS differences in the cloudy case, there is tendency to a better agreement between WV/Rayleigh winds from Meteosat-8/11 and ADM-Aeolus during the descending phase. Differences in mean HLOS wind speed differences between ascending and descending orbit of approximately 3 ms^{-1} are reported for mid-level winds. For high-level winds, these differences amount to approximately 1 ms^{-1} .

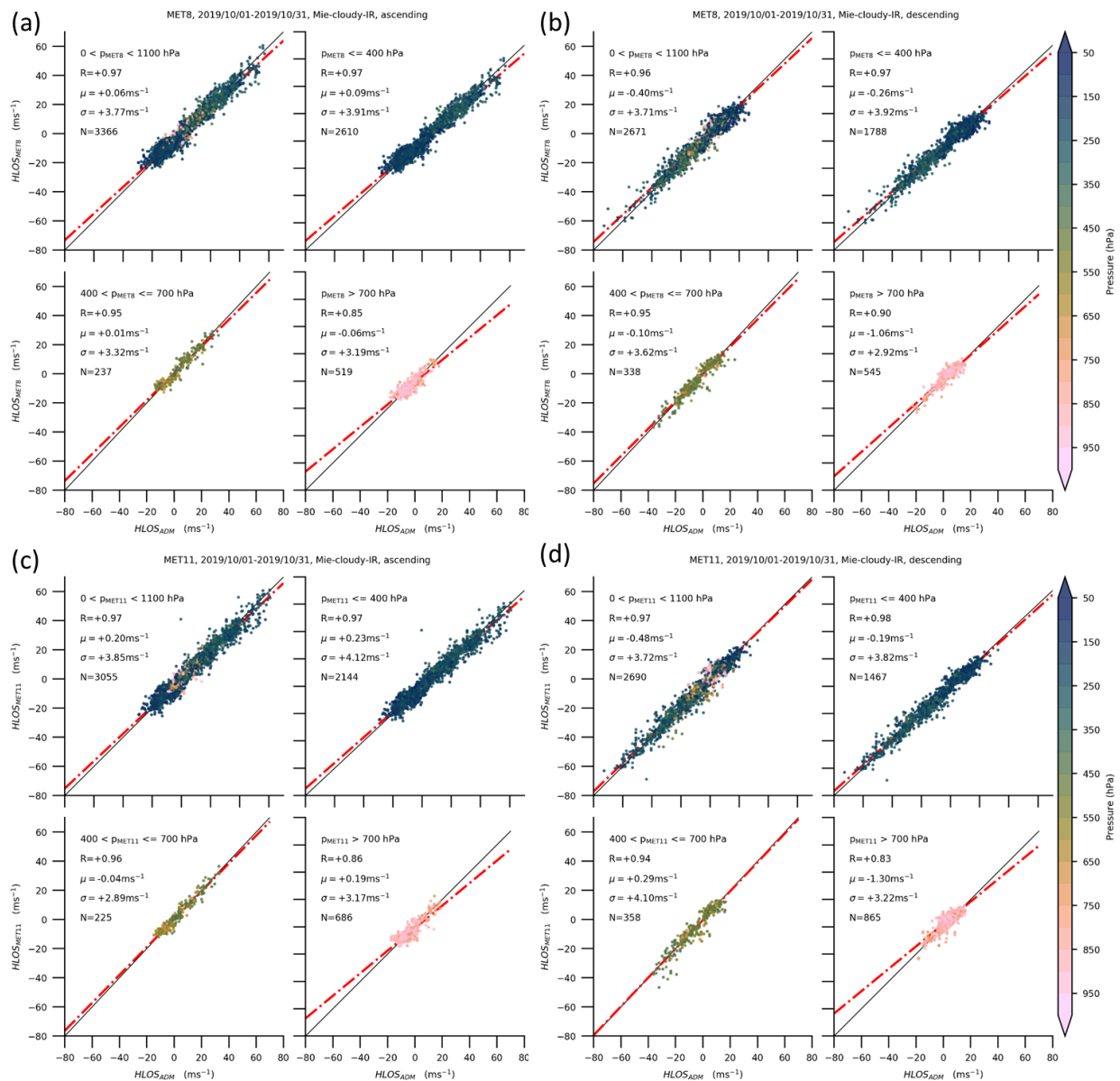


Figure 7.6 : Scatterplots of HLOS winds from Mie-channel ADM-Aeolus data ($HLOS_{ADM}$) against HLOS winds derived from (a, b) Meteosat-8 and (c, d) Meteosat-11 IR AMVs. (Left column) Results for ascending orbit. (Right column) Results for descending orbit.

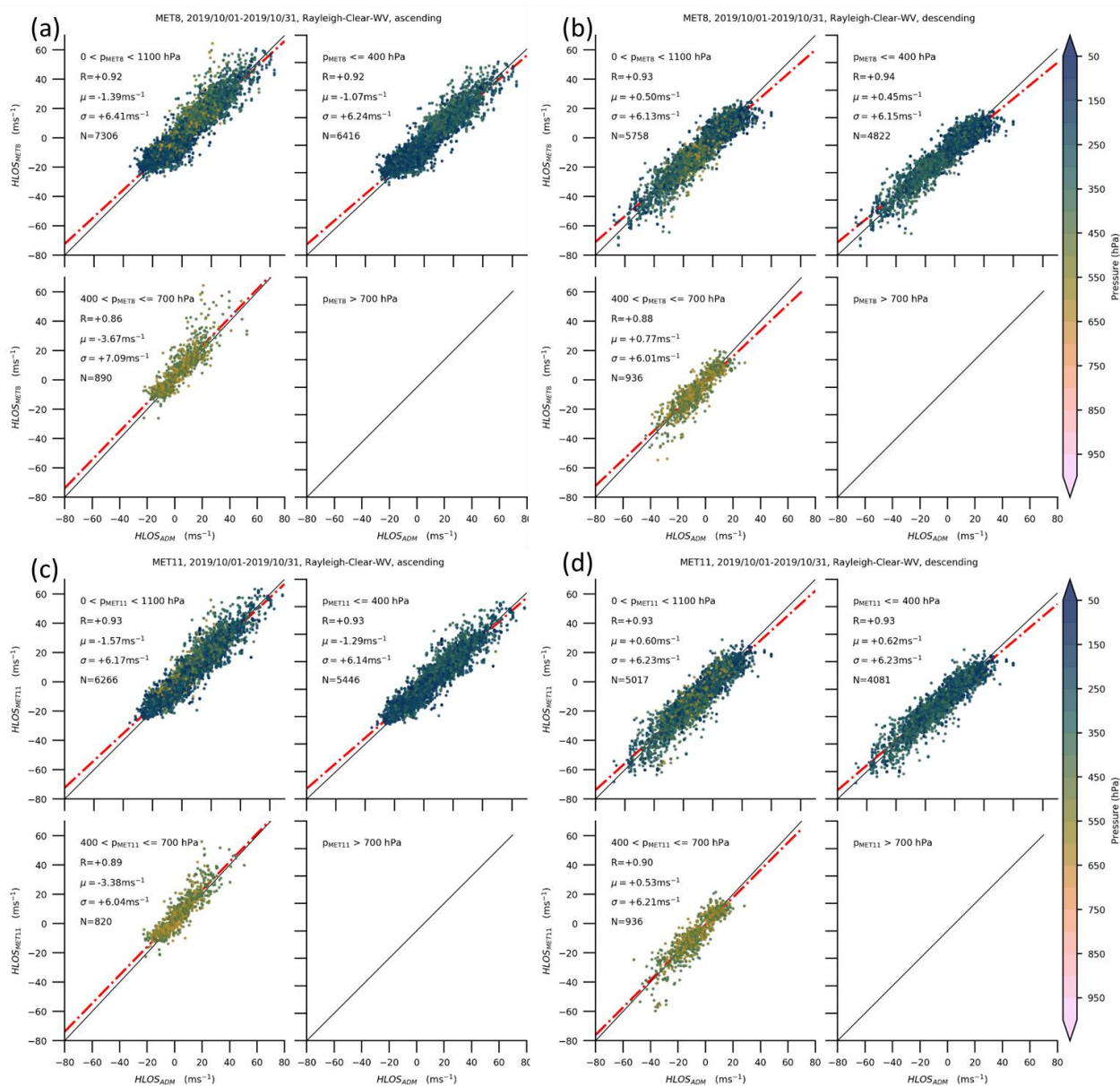



Figure 7.7 : Scatterplots of HLOS winds from Rayleigh-channel ADM-Aeolus data ($HLOS_{ADM}$) against HLOS winds derived from (a, b) Meteosat-8 and (c, d) Meteosat-11 WV AMVs. (Left column) Results for ascending orbit. (Right column) Results for descending orbit.

7.2.3 Best-fit pressure statistics

Scatter plots of Rayleigh/clear ADM-Aeolus pressure against Meteosat-8 and Meteosat-11 WV AMV pressure are shown in Figure 7.8a, b and Figure 7.9a, b respectively. Here, for each AMV we search for a collocated wind profile of ADM-Aeolus and selected the element of this wind profile that minimizes the

	<p align="center">Study of AMV speed biases in the tropics</p> <p align="center">Final Report</p>	
Reference: AMV-TN-0008-TS_Ed1_Rev3	Date : 18/06/2020	Page : 97/118

HLOS difference to the AMV irrespective of the pressure difference; that is, the 15-hPa vertical collocation constraint was relaxed. Correlation of AMV and ADM-Aeolus pressure is relatively weak ($R < 0.30$). Mean pressure differences $p_{ADM} - p_{Met8/11}$ range from about -35 to -65 hPa. Interestingly, mean pressure differences are smaller for the ascending orbit, while the mean statistics of the wind speed differences indicated better agreement between Meteosat-8/11 and ADM-Aeolus for the descending orbit. Figure 7.8c, d and Figure 7.9c, d indicate that the obtained pressure difference increase with increasing pressure. While for $p_{Met8/11} < 250$ hPa, mean of pressure differences is close to 0 hPa, mean of pressure differences amounts to 250 hPa for $p_{Met8/11} > 250$ hPa, casting some doubt on the mid-level wind speed agreement obtained in Section 7.2.1 (see Figure 7.4). Figure 7.10 confirms these finding as most collocations (80%) are found within a pressure difference of about 200 hPa.

Scatter plots of Mie/cloudy ADM-Aeolus pressure against Meteosat-8 IR AMV pressure are shown in Figure 7.11a, b. Results for ascending and descending orbit are relatively similar. On average, Meteosat-8 WV AMV tend to be set slightly too high (~16 hPa) in the atmosphere with respect to the ADM-Aeolus pressure. Pressure differences as function of AMV pressure are given in Figure 7.11c, d. The pressure differences $p_{ADM} - p_{Met8}$ tend to be positive for $p_{Met8} < 500$ hPa (p_{Met8} is set higher in the atmosphere than ADM-Aeolus) and negative for $p_{Met8} > 500$ hPa (p_{Met8} is set lower in the atmosphere than ADM-Aeolus) for both ascending and descending orbit. Results for Meteosat-11 IR AMVs are quite similar compared to the results of Meteosat-8 IR AMVs (Figure 7.12). Overall, most collocations (80%) are found within a pressure difference of less than 100%, which is a substantially smaller pressure difference than what was found for the Rayleigh/clear case.

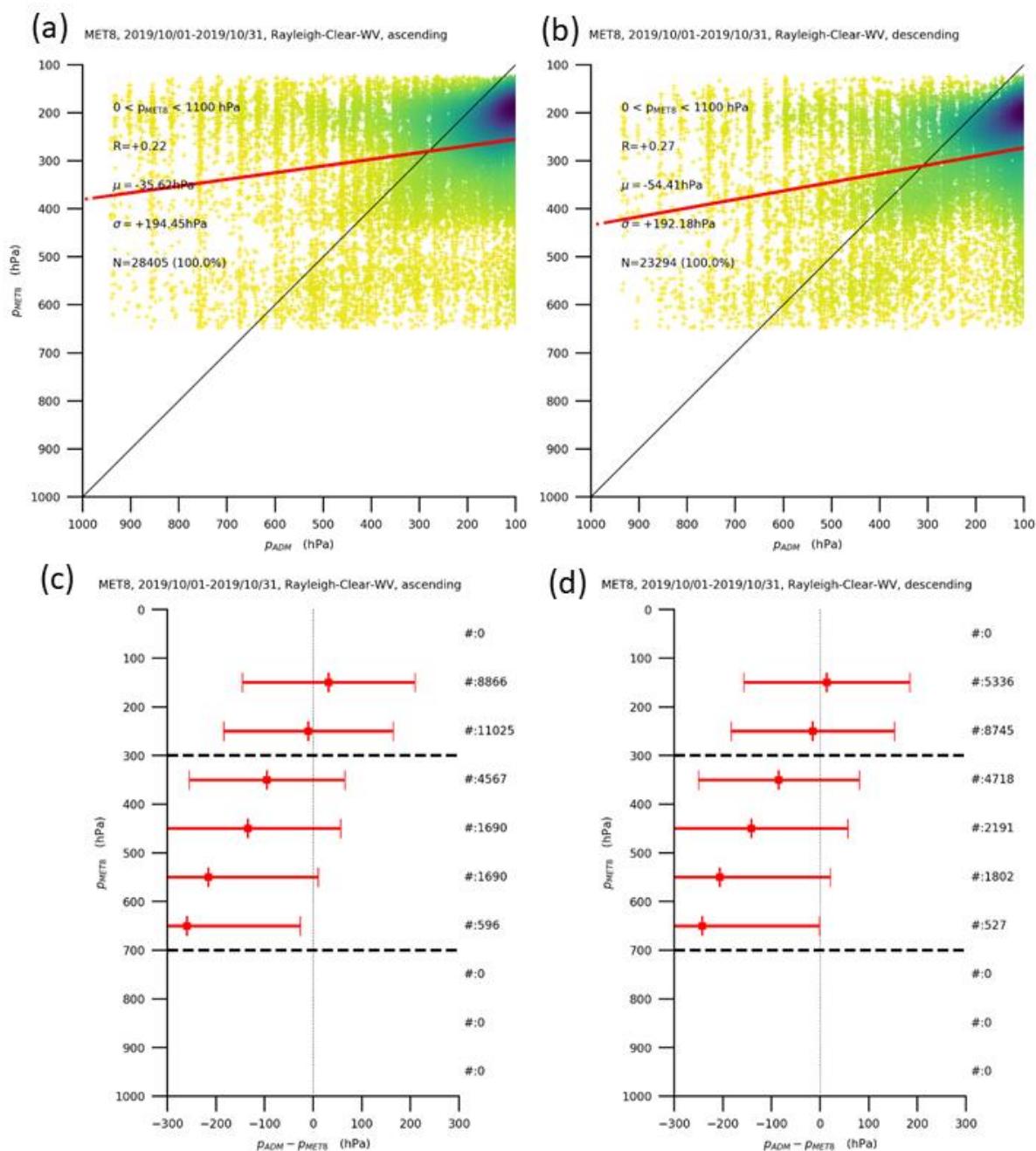


Figure 7.8 : Rayleigh/clear ADM-Aeolus pressure against Meteosat-8 WV AMV pressure (Upper panel). Meteosat-8 pressure against ADM-Aeolus for (a) ascending and (b) descending orbit. R denotes Pearson's correlation coefficient, μ the mean differences between ADM-Aeolus and Meteosat-8 and σ the standard deviation of the pressure differences. N denotes the sample size used to calculate σ , μ and R. (Lower panel) Mean pressure differences and corresponding standard deviation of 100 hPa thick layers.

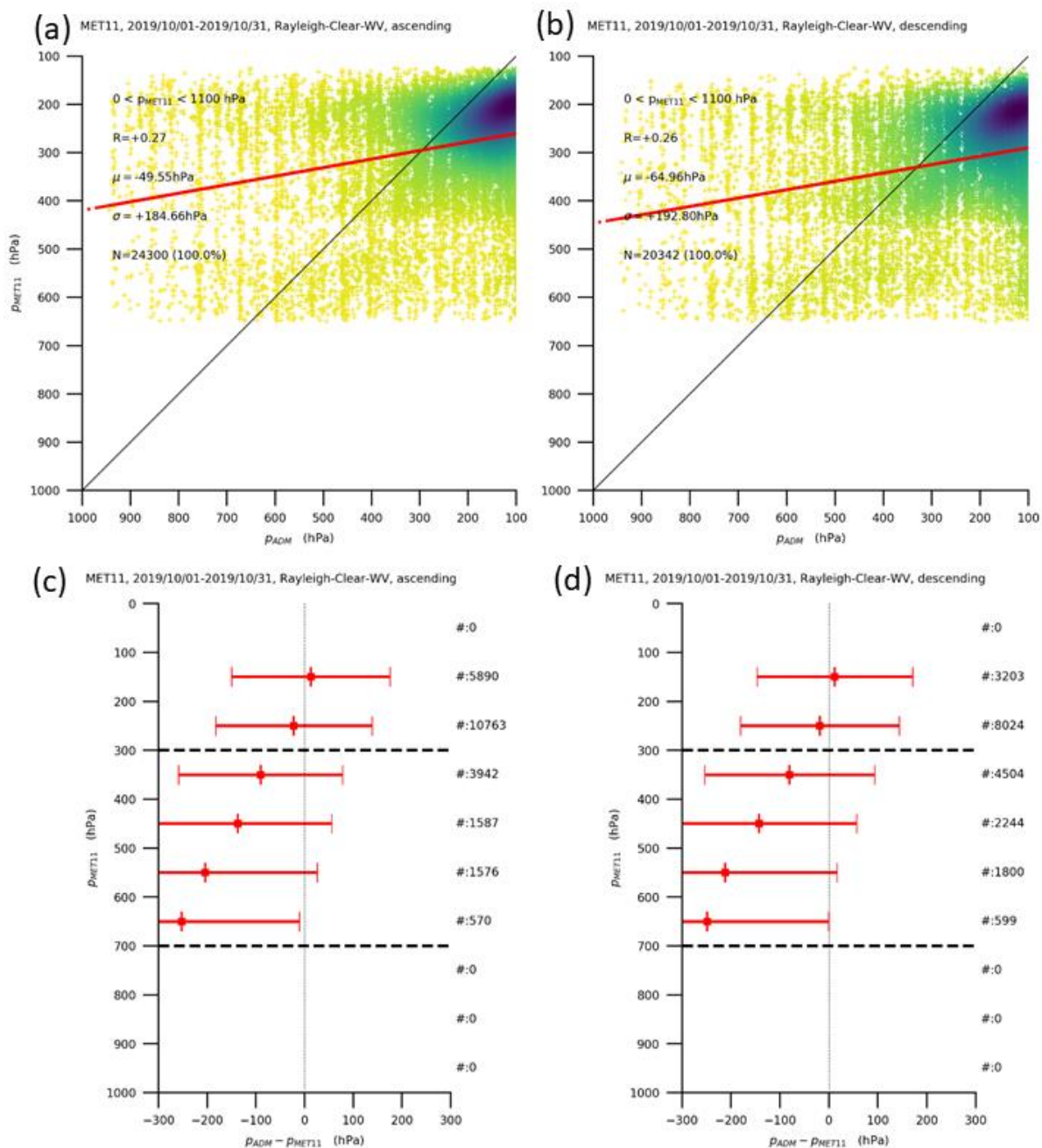



Figure 7.9 : As Figure 7.8 but pressures assigned to Meteosat-11 WV AMVs are compared to ADM-Aeolus Rayleigh/clear HLOS winds.

	<p align="center">Study of AMV speed biases in the tropics</p> <p align="center">Final Report</p>	
Reference: AMV-TN-0008-TS_Ed1_Rev3	Date : 18/06/2020	Page : 100/118

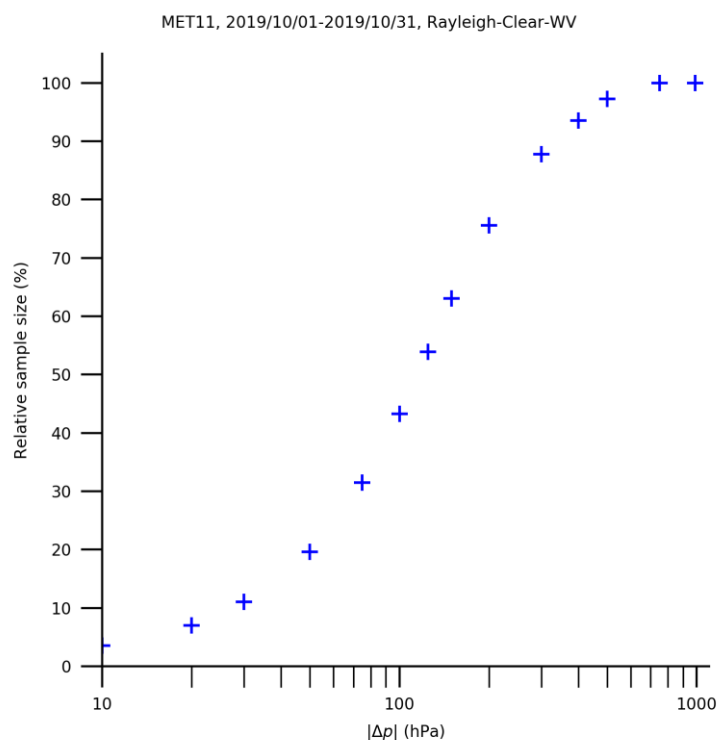


Figure 7.10 : Relative sample size of Rayleigh/clear ADM-Aeolus - Meteosat-11 IR AMV best-fit pressure collocations as function of allowed pressure difference $|\Delta p|$. Each AMV was searched for a collocated wind profile of ADM-Aeolus and the element of this wind profile that minimizes the HLOS difference to the AMV within an allowed pressure difference Δp is added to the sample. The obtained size of this sample is then related to the size of the sample where no Δp criterion is imposed.

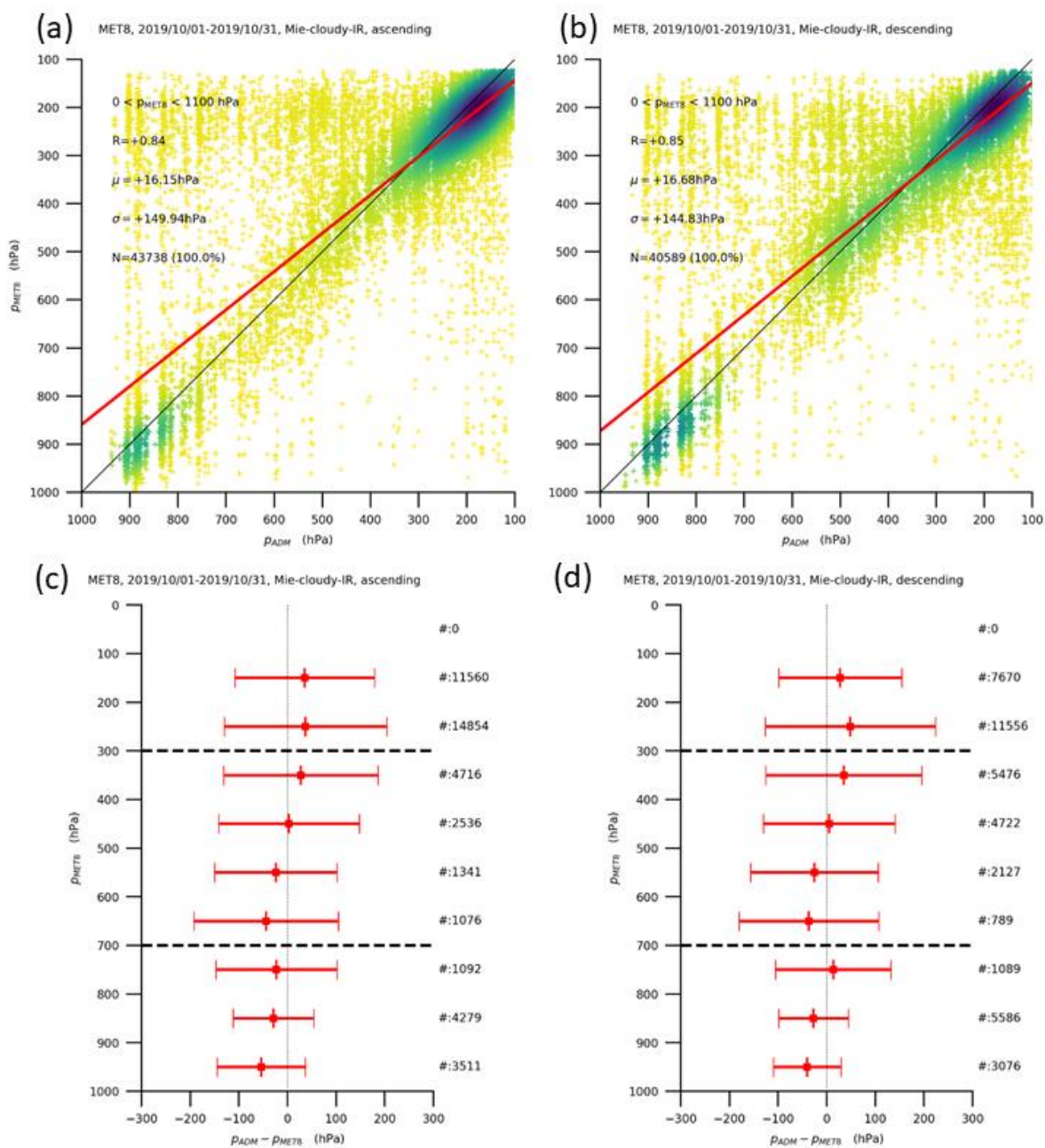


Figure 7.11 : Mie/cloudy ADM-Aeolus pressure against Meteosat-8 IR AMV pressure (Upper panel). Meteosat-8 pressure against ADM-Aeolus for (a) ascending and (b) descending orbit. R denotes Pearson's correlation coefficient, μ the mean differences between ADM-Aeolus and Meteosat-8 and σ the standard deviation of the pressure differences. N denotes the sample size used to calculate σ , μ and R . (Lower panel) Mean pressure differences and corresponding standard deviation of 100 hPa thick layers.

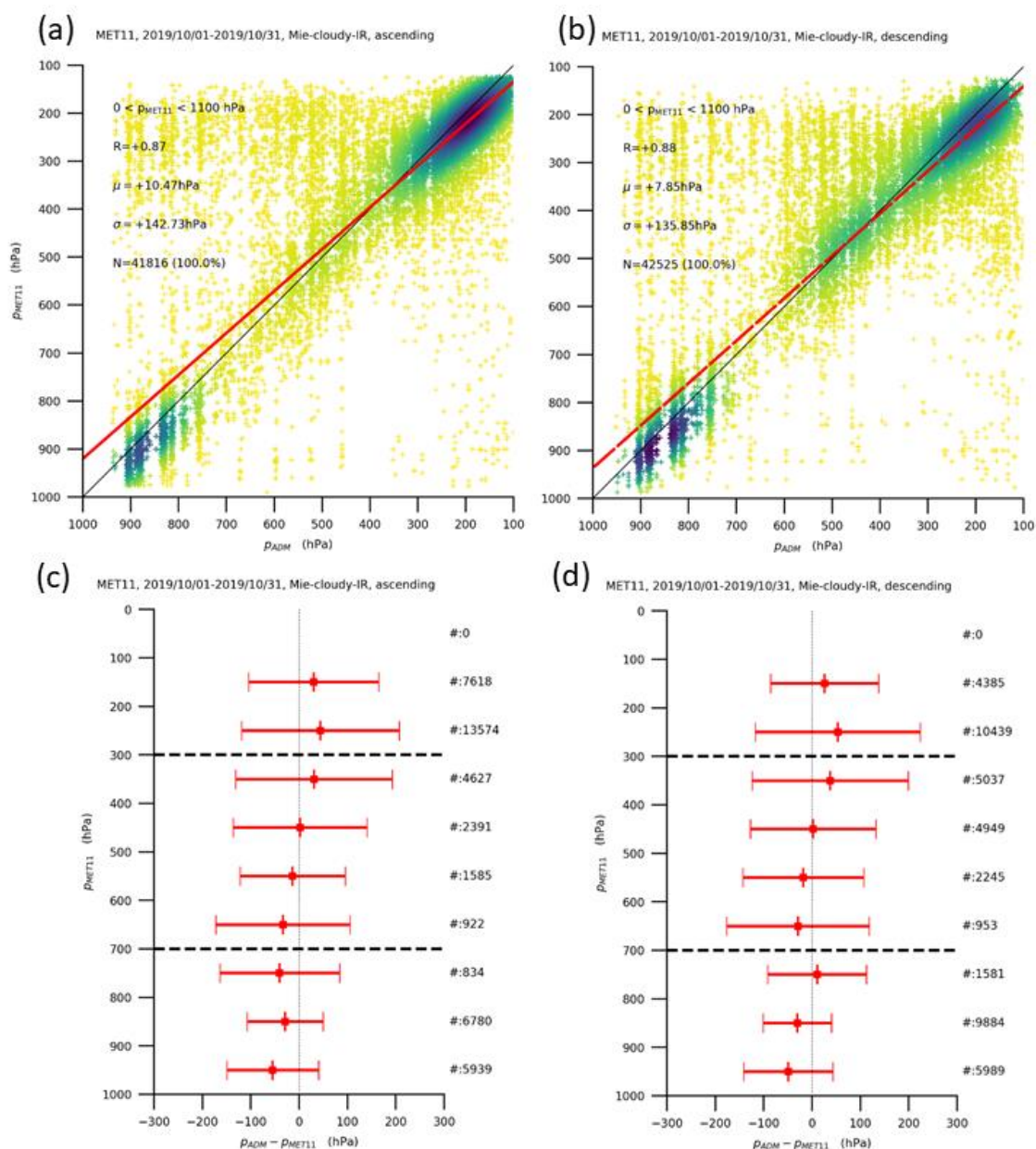



Figure 7.12 : As Figure 7.11 but pressures assigned to Meteosat-11 IR AMVs are compared to ADM-Aeolus Mie/cloudy HLOS winds.

	<p align="center">Study of AMV speed biases in the tropics</p> <p align="center">Final Report</p>	
Reference: AMV-TN-0008-TS_Ed1_Rev3	Date : 18/06/2020	Page : 103/118

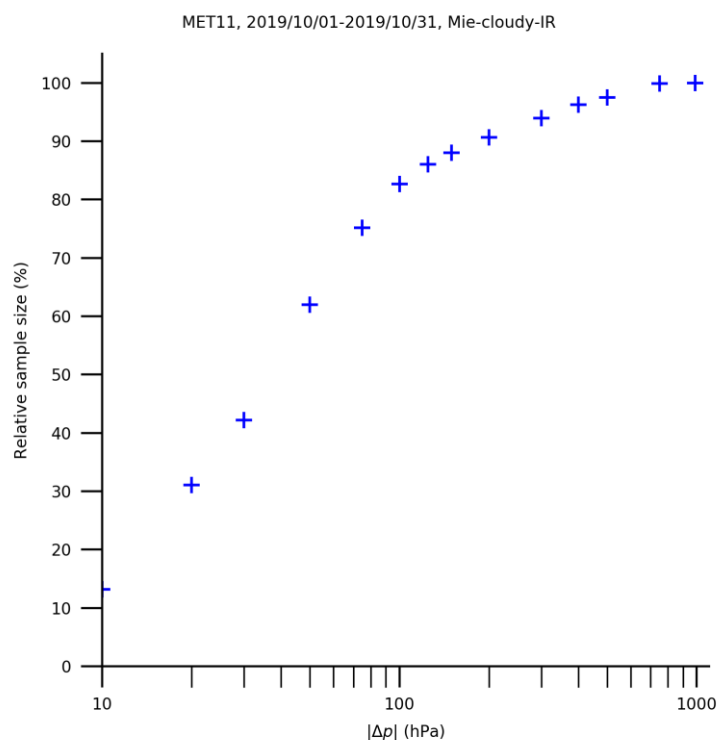



Figure 7.13 : As Figure 7.10 but the relative sample size of Mie ADM-Aeolus – Meteosat-11 IR AMV collocations is plotted against $|\Delta p|$.

7.3 CASE STUDIES

7.3.1 Case 1 - Winds over Arabian Peninsula in October 2019

We have seen in Sections 5.3 and 6.1 that AMVs derived over the Saharan desert and during jet situations are frequently assigned to erroneous (too low) altitudes, leading to monthly speed bias against ECMW winds of up to 3 ms⁻¹. Figure 7.14 show fast speeds (mean wind speed > 35 ms⁻¹) prevail in the last week of October over the Arabian Peninsula, here defined as region extending from 20°N to 35°N and from 20°E to 65°E. Visual comparison of AMVs projected onto the Aeolus line-of-sight and ADM-Aeolus HLOS winds indicate a reasonable agreement of both wind datasets in such a situation (see Figure 7.2). As this geographical area is covered by both Meteosat-8 and Meteosat-11, we compare both datasets against ADM-Aeolus.

	<p align="center">Study of AMV speed biases in the tropics</p> <p align="center">Final Report</p>	
Reference: AMV-TN-0008-TS_Ed1_Rev3	Date : 18/06/2020	Page : 104/118

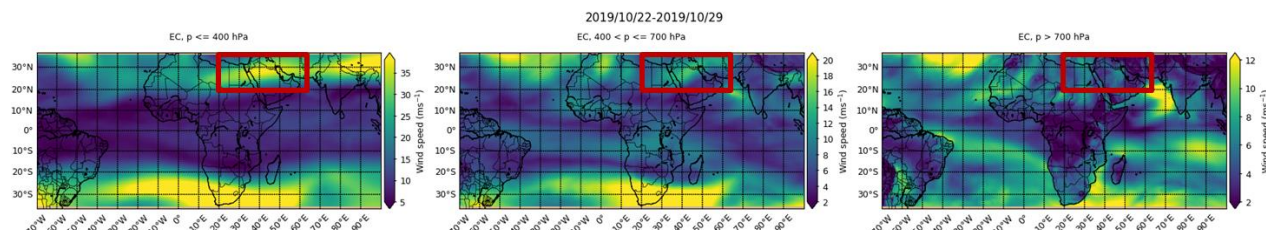



Figure 7.14 : High-, mid-, and low-level winds from ECMWF, averaged over the period 22 October 2019 to 29 October 2019. The red box indicates the region for which AMVs and ADM-Aeolus HLOS winds are compared.

Scatterplots of Mie/cloudy ADM-Aeolus against HLOS winds obtained by IR AMVs from Meteosat-8, Meteosat-11 and by ECMWF are shown in Figure 7.15a, b and Figure 7.16a, respectively. We did not separate results for ascending and descending orbit due to the relatively small sample size of collocated AMVs. However, as mentioned above results for both orbiting phases are expected to be relatively similar for the Mie/cloudy channel. Results indicate an agreement of better than 1 ms^{-1} for all levels and data sets; with the only notable exceptions being the low-levels from ECMWF that agree within $-1.55 \pm 4.58 \text{ ms}^{-1}$ with ADM-Aeolus (Figure 7.16a).

Scatter plots of Mie/cloudy ADM-Aeolus pressure against Meteosat-8 and Meteosat-11 IR AMV pressure are shown in Figure 7.17a, b. Here, for each AMV we search for a collocated wind profile of ADM-Aeolus and selected the element of this wind profile that minimizes the HLOS difference to the AMV irrespective of the pressure difference; that is, the 15-hPa vertical collocation constraint was relaxed. The scatter plots indicate that for most of the data, pressure difference is smaller than 100 hPa. Some outliers exist, where pressure difference exceed 200 or 300 hPa, indicating that different wind profiles are observed. Figure 7.18 confirms that for most collocations (about 55-60%) best-fit pressure differences are smaller than 50 hPa, while for about 80% of the collocations best-fit pressure differences are smaller than 100 hPa. Mean pressure difference profiles are shown in Figure 7.17c, d. The obtained difference profiles are relatively similar for both Meteosat satellites. On average, for $p < 500 \text{ hPa}$, pressure assigned to AMVs are 20 to 50 hPa lower than ADM-Aeolus, that is, there is a tendency that high-level AMVs are assigned to too high altitudes ($p_{\text{ADM}} > p_{\text{AMV}}$). Conversely, for mid- to low-levels, AMVs tend to have assigned too low altitudes ($p_{\text{AMV}} > p_{\text{ADM}}$). The obtained results thus do not fully confirm the results from the comparison of AMVs to cloud top pressure obtained by CALIOP/CALIPSO over the Saharan desert, where results indicate that $p_{\text{AMV}} > p_{\text{CALIPSO}}$ almost throughout the entire profile, which may be explained by the different period and region covered by the comparison studies.

	<p align="center">Study of AMV speed biases in the tropics</p> <p align="center">Final Report</p>	
Reference: AMV-TN-0008-TS_Ed1_Rev3	Date : 18/06/2020	Page : 105/118

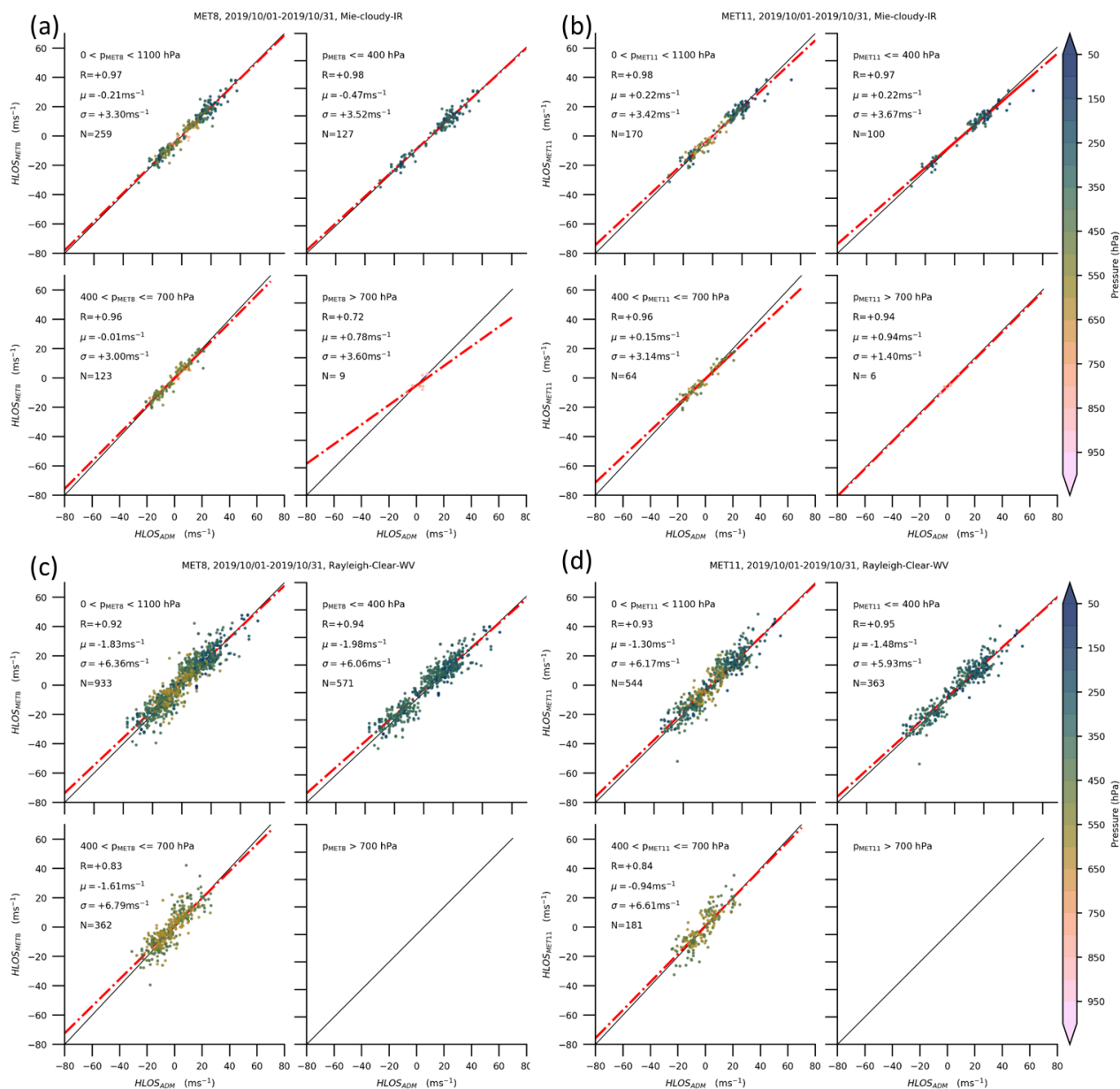



Figure 7.15 : Scatterplots of HLOS winds from ADM-Aeolus data ($HLOS_{ADM}$) against HLOS winds derived from (a, b) IR AMVs and (c, d) WV AMVs over the Arabian peninsula in October 2019. (Left column) Results for Meteosat-8. (Right column) Results for Meteosat-11.

	<p align="center">Study of AMV speed biases in the tropics</p> <p align="center">Final Report</p>	
Reference: AMV-TN-0008-TS_Ed1_Rev3	Date : 18/06/2020	Page : 106/118

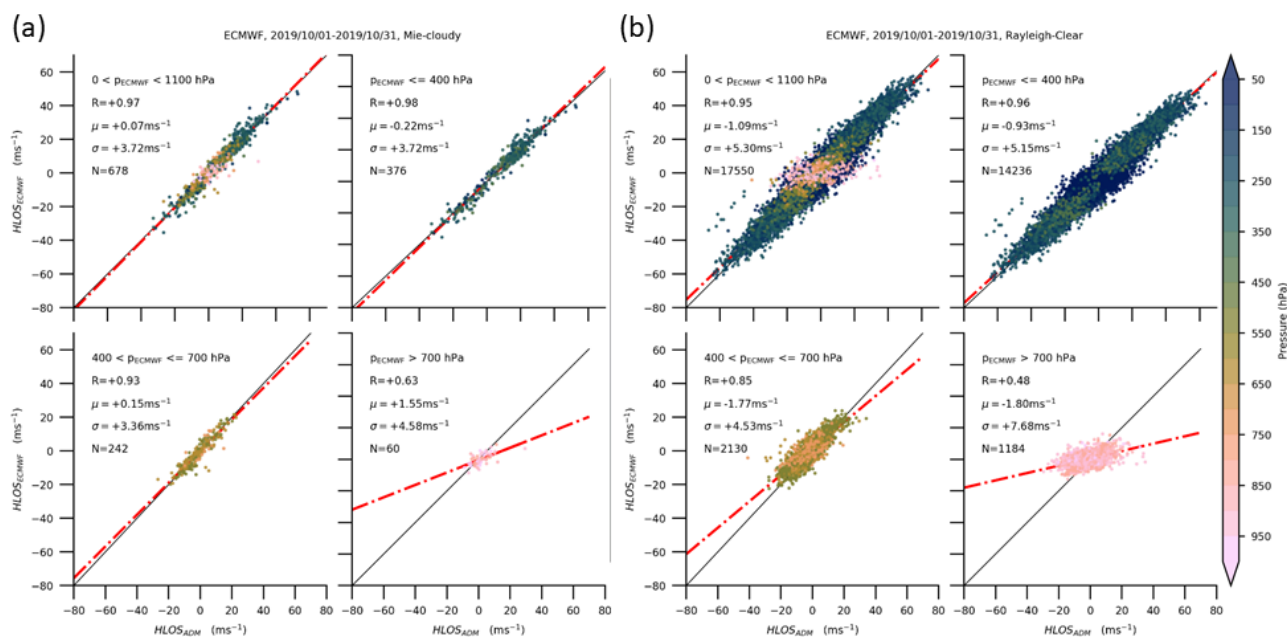


Figure 7.16 : Scatterplots of HLOS winds from ADM-Aeolus data ($HLOS_{ADM}$) against HLOS winds derived from ECMWF over the Arabian Peninsula in October 2019. (a) Results for Mie/cloudy HLOS winds. (b) Results for Rayleigh/clear HLOS winds.

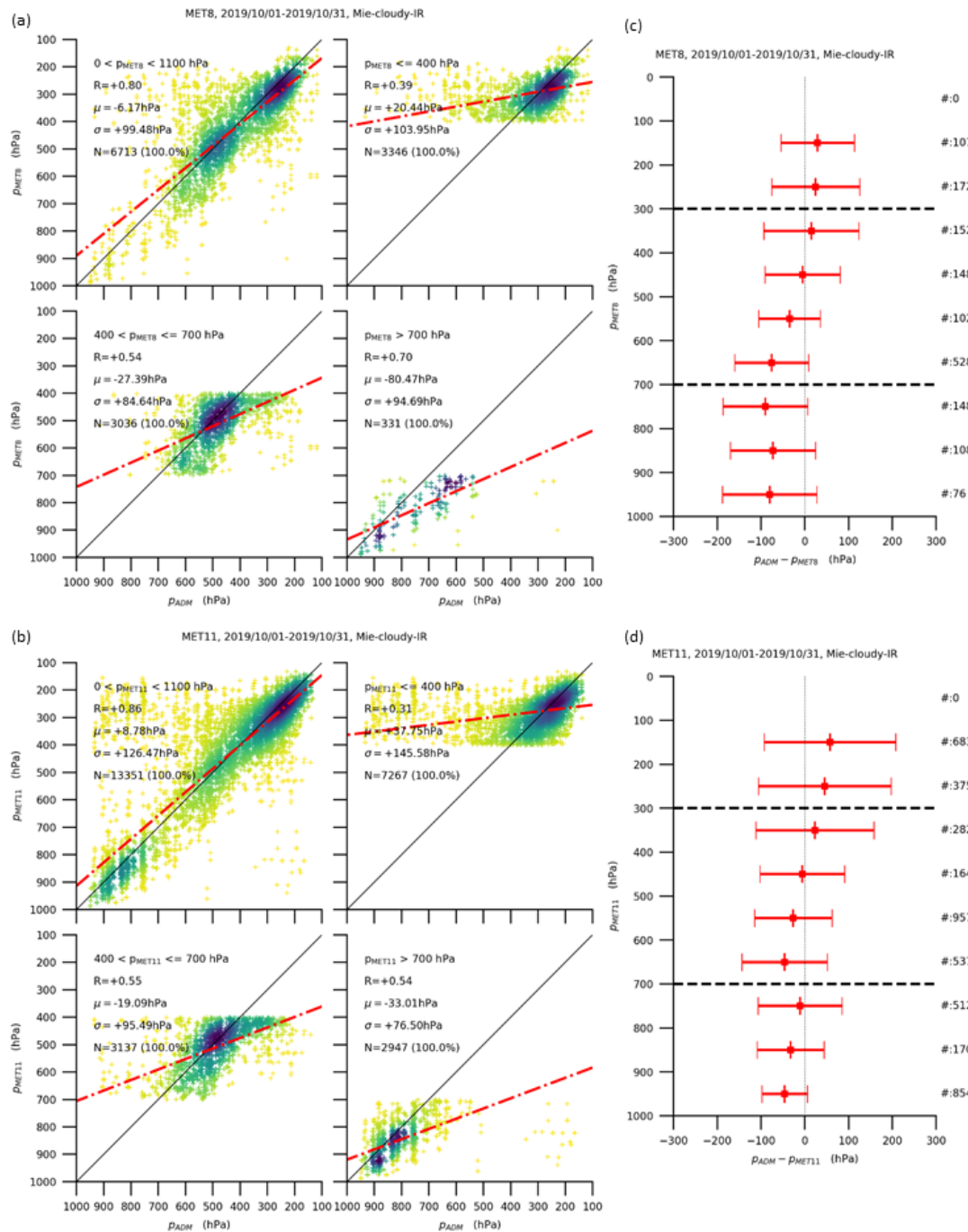



Figure 7.17 : Mie/cloudy ADM-Aeolus pressure against Meteosat-8 and Meteosat-11 IR AMV pressure. (Left column) Scatter plots of ADM-Aeolus pressure against (a) Meteosat-8 and (b) Meteosat-11 pressure over the Arabian Peninsula in October 2019. (Right column) Mean pressure differences and corresponding standard deviation of 100 hPa thick layers for (c) Meteosat-8 and (d) Meteosat-11.

	Study of AMV speed biases in the tropics Final Report	
Reference: AMV-TN-0008-TS_Ed1_Rev3	Date : 18/06/2020	Page : 108/118

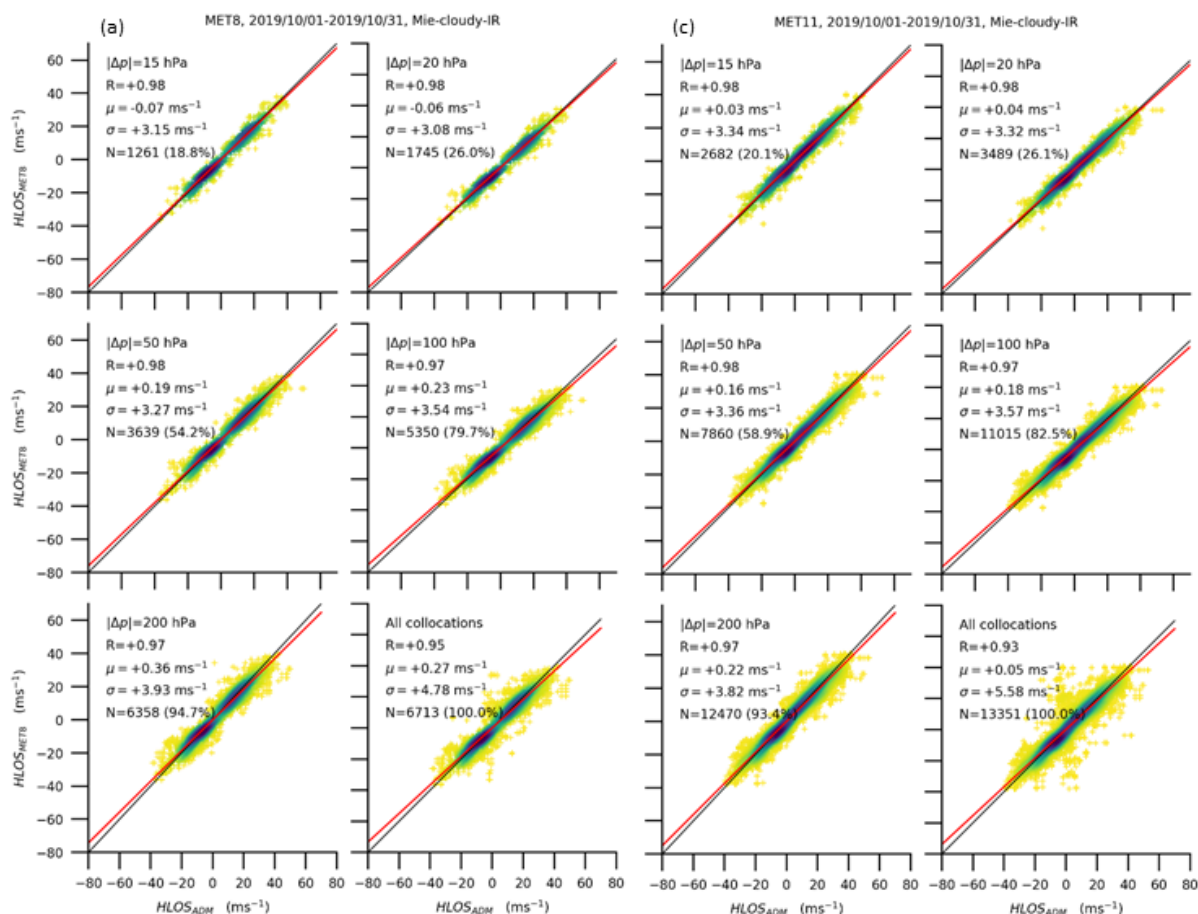


Figure 7.18 : HLOS winds from Mie/cloudy ADM-Aeolus against HLOS winds derived from (a) Meteosat-8 and (b) Meteosat-11 IR AMV over the Arabian Peninsula in October 2019. AMVs were searched for a collocated wind profile of ADM-Aeolus and the element of this wind profile that minimizes the HLOS difference to the AMV within an allowed pressure difference Δp is plotted against the HLOS AMV. R denotes Pearson's correlation coefficient, μ the mean wind speed difference between ADM-Aeolus and AMV, σ the corresponding standard deviations. N denotes the sample used to compute the speed differences, while the number in bracket sets N in relation to the sample size where no Δp criterion is imposed ("all collocations").

Scatter plots of Rayleigh/clear ADM-Aeolus wind pressure against Meteosat-8, Meteosat-11 WV winds and ECMWF winds are shown in Figure 7.15c, d and Figure 7.16b. For high- and mid-levels, the three reference winds shows similar mean statistics (mean, standard deviation of differences, Pearson's correlation coefficient) and distribution of data points. Interestingly, ECMWF low levels indicate higher standard deviation and a weaker correlation coefficient of 0.48 (Figure 7.16), which is substantially lower than the standard deviation and correlation obtained for mid- or high-level winds ($R > 0.80$).

Scatter plots of best-fit pressure are given Figure 7.19a, b in conjunction with profiles of best-fit pressure differences (Figure 7.19c, d). Results indicate that the AMV algorithm assigns too low altitudes ($p_{ADM-AMV} < 0$), whereby differences are larger at mid- than at high-level.

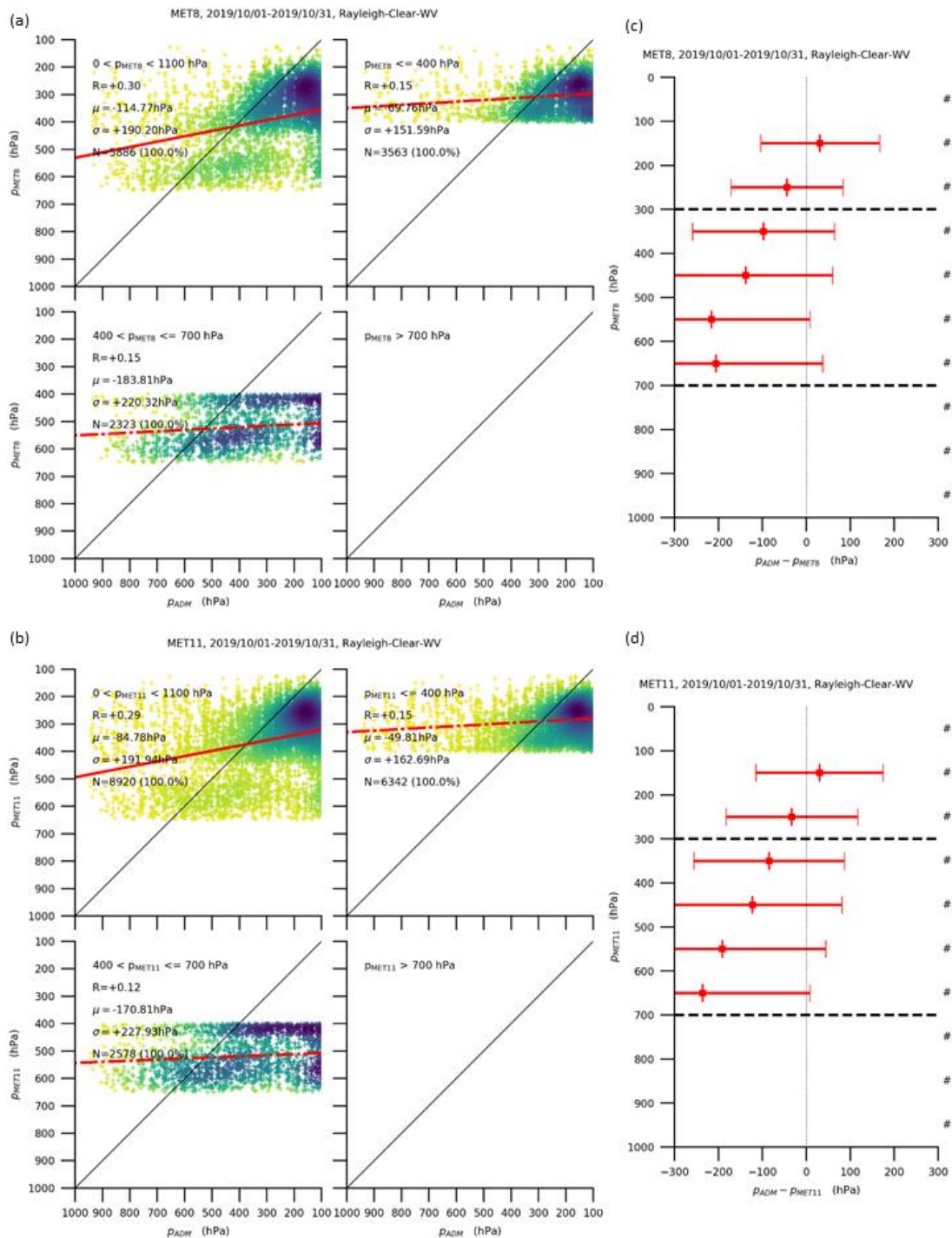



Figure 7.19 : As Figure 7.17 but Rayleigh/clear HLOS winds from ADM-Aelous are compared against Meteosat-8 and Meteosat-11 WV winds.

	Study of AMV speed biases in the tropics Final Report	
Reference: AMV-TN-0008-TS_Ed1_Rev3	Date : 18/06/2020	Page : 110/118

7.3.2 Case 2 - Winds over Indian Ocean October-November 2019

Case 2 aims at analysing the agreement ADM-Aeolus against ECMWF and AMVs over the Indian Ocean, here defined as a region that extends from 10°N to 20°N and from 65°E to 75°E. As Meteosat-11 does not cover this region, only results from Meteosat-8 could be presented.

Scatter plots of HLOS difference obtained from the Mie channel against HLOS from IR AMVs and against ECMWF winds is given in Figure 7.20. Few IR AMVs could be compared to ADM-Aeolus and the overwhelming majority are high-level AMVs. Results for these high-level winds indicate similar agreement as we have already obtained for case 1 and Mie-cloudy-IR data (see Figure 7.15a, b). As for Meteosat-8, the overwhelming majority of ECMWF winds compared to ADM-Aeolus are high-level winds.

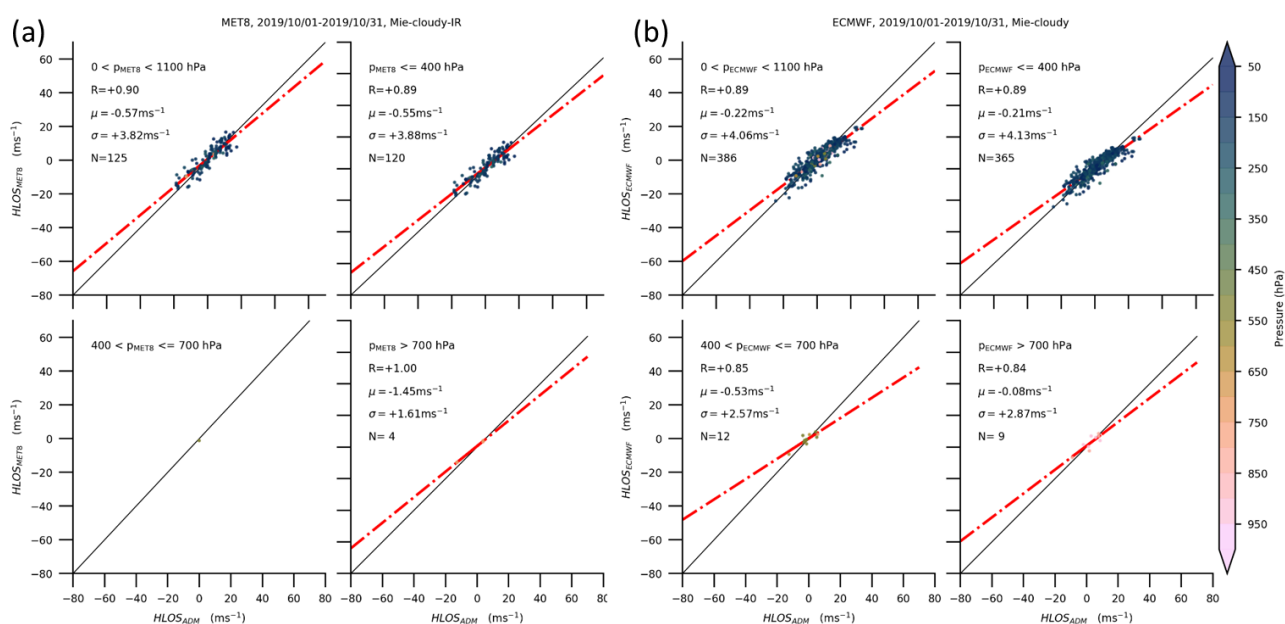



Figure 7.20 : Scatterplots of HLOS winds from Mie-channel ADM-Aeolus data ($HLOS_{ADM}$) against HLOS winds derived from (a) Meteosat-8 IR AMVs and (b) ECMWF winds over the Indian Ocean.

Scatter plots of HLOS difference obtained from the Rayleigh channel against HLOS derived from WV AMVs and from ECMWF winds is given in Figure 7.21a, b for October 2019. The sample size of comparable AMVs is relatively small for this case and practically limited to high-level winds. Obtained statistics for these high-level winds is similar to that obtained for IR AMVs. For ECMWF winds, apparent is the low correlation of model winds to ADM-models at low levels. While at high-levels R ranges from 0.77 to 0.70, it drops to 0.53 at low-levels, where, however, only few collocations are reported. At low-levels, the HLOS winds modelled by ECMWF are relatively slow, with most HLOS wind speeds found between 0 and -10 ms⁻¹. By contrast, collocated HLOS winds from ADM-Aeolus cover a much larger range of HLOS wind speeds, ranging from -20 to 20 ms⁻¹. This indicates that different wind patterns are obtained by both data sets. Note the similar statistics obtained for November (Figure 7.21c, d), which may points to a rather systematic disagreement between ADM-Aeolus and ECMWF low-level winds in this region.

	<p align="center">Study of AMV speed biases in the tropics</p> <p align="center">Final Report</p>	
Reference: AMV-TN-0008-TS_Ed1_Rev3	Date : 18/06/2020	Page : 111/118

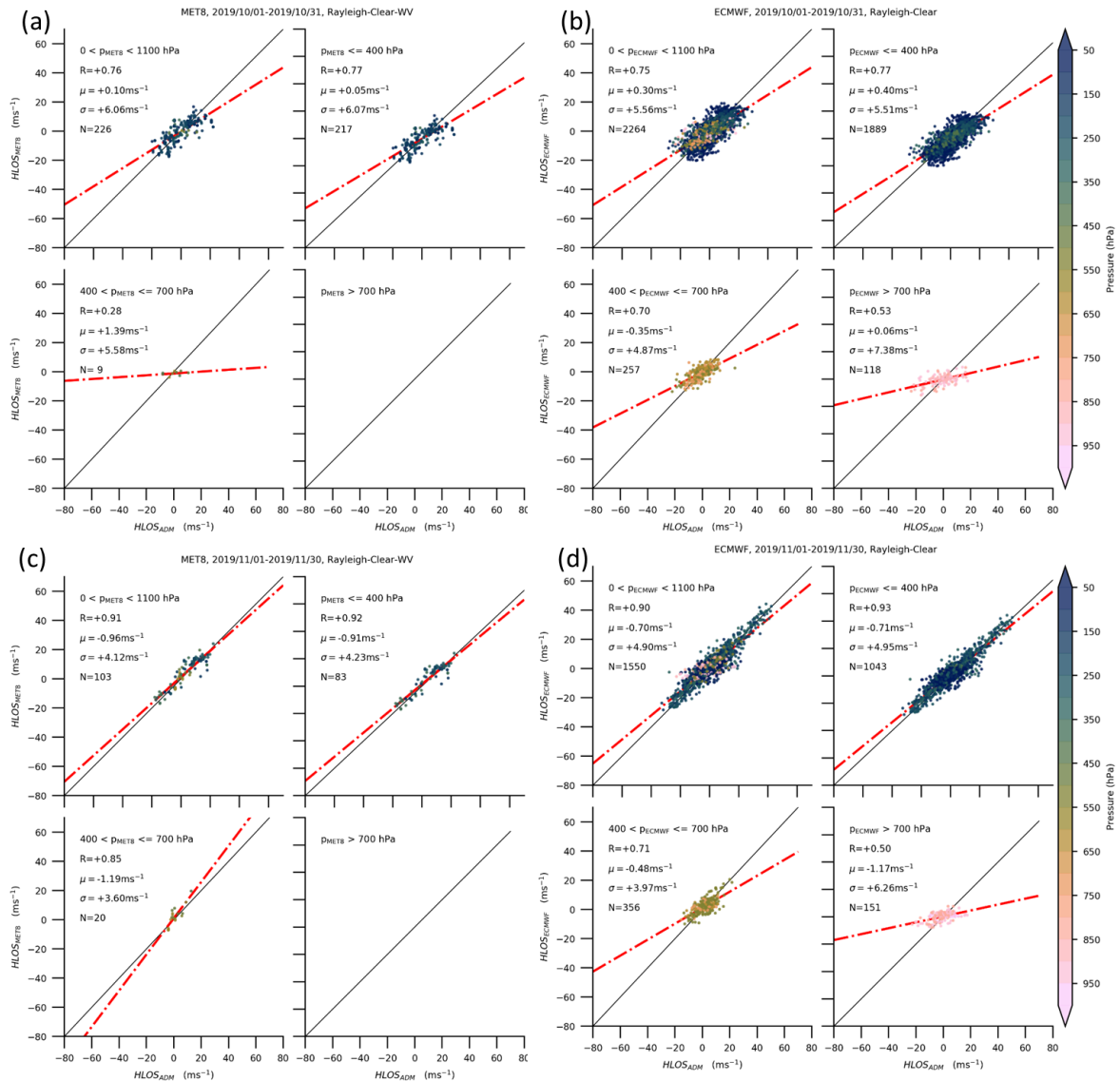



Figure 7.21 : Scatterplots of HLOS winds from Rayleigh-channel ADM-Aeolus ($HLOS_{ADM}$) against HLOS winds derived from (a, b) Meteosat-8 WV AMVs and (c, d) ECMWF winds over the Indian Ocean. (Upper panel) Results for October 2019. (Lower panel) Results for November 2019.

	<p align="center">Study of AMV speed biases in the tropics</p> <p align="center">Final Report</p>	
Reference: AMV-TN-0008-TS_Ed1_Rev3	Date : 18/06/2020	Page : 112/118

8 SUMMARY AND RECOMMENDATIONS

8.1 MEAN STATISTICS


Comprehensive statistics of (non-normalised) mean wind speed differences between AMVs from different satellite-channel combinations and gridded ECMWF forecast winds for the tropical region (between -30°N and 30°N) were established. For AMVs derived by EUMETSAT from IR imagery, we conclude

1. For high-level clouds, the pattern of O-B speed bias obtained for Met10EUM AMV and Metop-A/B AMV differs. For AMVs derived from the geostationary Meteosat-10 satellite, areas of positive O-B speed biases $> 3 \text{ ms}^{-1}$ commonly coincide with the location of the subtropical jet that migrates with the changing position of the thermal equator. Other areas of large wind speed discrepancies ($> 3 \text{ ms}^{-1}$) are found over desert sites and oceans, potentially attributable to the lack of observational data to constrain appropriately the NWP model or incorrect height assignment. For AMVs obtained from Metop, a different spatial pattern at this level was obtained: O-B speed bias was negative for regions exhibiting mean wind speeds greater than 30 ms^{-1} , while positive O-B speed biases were obtained for low wind speed regions around the equator.
2. For mid-level clouds, large differences of $> 6 \text{ ms}^{-1}$ were found over the Sahara desert in northern hemisphere winter for Met10EUM, likely due to AMV altitudes set too low in the atmosphere. For Metop, observed pattern of mean wind speed differences resemble that observed at high levels. However, observed amplitude of wind speed differences is smaller, coinciding with smaller wind speeds at these altitudes. At low-levels, Met10EUM agrees with ECMWF within 1 ms^{-1} , except for certain arid locations in Northern Africa. For Metop, the observed O-B speed biases are typically of similar magnitude as for Met10EUM.
3. Comparing observed O-B speed biases to parameters describing strength and type of convection such as GDI, OLR, to CLOUDSAT cloud type as well as to the diurnal cycle of convection revealed no clear dependency of the O-B speed bias to these parameters. However, it is interesting to note that Metop tends to sense in stronger convective regimes than Met10EUM, which may be explained by the fact that Metop also senses over Monsoon regions of South East Asia and its temporal sampling. In contrast to Met10EUM, it overpasses tropical locations once in the morning and once in the evening.

8.2 CASE STUDIES

AMV speed biases were investigated more thoroughly for two cases: (1) Met10EUM AMV mid- and high-level speed bias over Saharan desert in March 2016 during westerly jet; (2) Metop AMV mid- and high-level speed bias over the Boiler-Box region in August 2016. From these two case studies we conclude that:

1. Met10EUM and model winds agree well over the considered region at levels above 250 hPa ($p \leq 250 \text{ hPa}$). This is revealed by comparing visually AMVs to model winds along approximately $\pm 0.25^\circ \text{E}$ broad north-south transects. A mean statistic based on two-weeks of data indicates that the O-B speed bias at these levels is about -1 to 1 ms^{-1} at these levels.

	<p align="center">Study of AMV speed biases in the tropics</p> <p align="center">Final Report</p>	
Reference: AMV-TN-0008-TS_Ed1_Rev3	Date : 18/06/2020	Page : 113/118


2. Visual comparison between Met10EUM AMV and model winds along north-south transects as well as CPR and CALIOP cloud top heights reveal that speed differences greater than 4 ms⁻¹ can be explained by having assigned too low altitudes to AMVs. This means that, due to contributions from the below the cloud (e.g. too warm desert surface temperature, errors in the emissivity of the sandy, deserts and often mountainous surfaces), the cloud top height ingested by the AMV extraction algorithm retrieves a too warm (and therefore a too low) cloud top.
3. High-level AMVs are derived for clouds classified by CLOUDSAT as cirrus or altostratus. Our results indicate no dependency of fast wind speed biases on cloud type. Furthermore, while certain fast wind speed biases coincide with the presence of multilayer clouds, a clear dependency of the fast wind speed biases could not be deduced as in most cases the presence of multilayer clouds did not adversely affect the agreement between model winds and AMV.
4. Height assignment errors unlikely explain why Metop AMVs are faster than model winds over the Boiler-Box region and there seem to be hardly any difference in observed speed difference between morning and evening Metop overpasses.
5. Metop- AVHRR IR radiances and corresponding TB fields indicate that due to the large temporal gap of 50 min between two images and due to the strong convection that may alter the shape of clouds, the feature to be tracked is difficult to relate between two AVHRR image pairs. Furthermore, the differences in brightness temperatures between two images indicate a relatively low correlation between the pixels.

8.3 COMPARISON TO ADM-AEOLUS

AMVs derived from Meteosat-8 and Meteosat-11 imagery were compared to wind profiles measured by the ALADIN instrument aboard ADM-Aeolus (L2B v3.20) during October to November 2019. Using collocation criteria of $\Delta x < 100$ km, $\Delta t < 30$ min and $\Delta p < 15$ hPa, mean HLOS speed differences between AMVs and ADM-Aeolus of 0.2 ± 3.4 ms⁻¹ were typically obtained, depending on altitude, region and on channel. Comparison of altitudes assigned to AMV IR winds (relaxation of the 15-hPa criterion), did not fully confirm previous findings of having too low altitudes assigned to AMVs over desertic areas.

8.4 RECOMMENDATIONS

For Met10EUM AMVs, the origin of the fast wind speed biases over the Saharan desert that mostly occurred around 300-500 hPa could be traced back to incorrect height assignments. That is, AMVs were set too low in the atmosphere and in conjunction with vertical wind shear and generally fast winds ("jets") lead to punctual difference greater than 6 ms⁻¹. Recently, Kealy et al. (2017) compared UK Met Office's suite of cloud products, including SEVIRI, to lidar derived CTHs and found substantial difference. They also noted a general issue in CTH retrievals over the Sahara, that is, that often a large portion of clouds have a horizontal extent smaller than the 3 km wide SEVIRI pixels. Consequently, in such cases the contribution from the warm desert surface lead to too warm cloud tops. In this sense, it will be interesting to see if the use of OCA cloud top heights instead of the current operational CLA-CTH (cloud type and cloud-top height) product can improve the quality of AMV data under such conditions (desert, fast wind speeds and high wind shear). Lastly, in view of AMVs being derived from MTG satellites, it will be interesting to see if the better horizontal resolution of the FCI instrument (pixel size of 1-2 km instead of 3 km of SEVIRI) can further alleviate the problem of having too low altitudes assigned to AMVs in such conditions.

	<p align="center">Study of AMV speed biases in the tropics</p> <p align="center">Final Report</p>	
Reference: AMV-TN-0008-TS_Ed1_Rev3	Date : 18/06/2020	Page : 114/118

The presented analysis indicates that AMVs are regularly faster than model winds over the Boiler-Box region. However, the reasons for this behaviour could not fully be deduced, in particular as the lack of independent reference data in the tropics renders evaluating Dual-Metop AMVs difficult. It is interesting to see that AMVs derived by CIMSS from the geostationary Meteosat-7 satellite agree with ECMWF winds within $\pm 2 \text{ ms}^{-1}$ on average at high levels over this area (Figure 65). CIMSS uses a smaller target box of 12×12 pixels than Metop (30×30 pixels) and the temporal gap is approximately 20 min smaller compared to AVHRR images (50 min). As noted by Garcia-Pereda and Borde (2014), there is a subtle relationship between the size of the tracer box, the temporal gap between consecutive images, the size and lifetime of the feature tracked and the quality of the tracking. This relationship between those parameters may is not ideal for deriving operationally AMVs from the Metop over the highly convective Boiler-Box region.

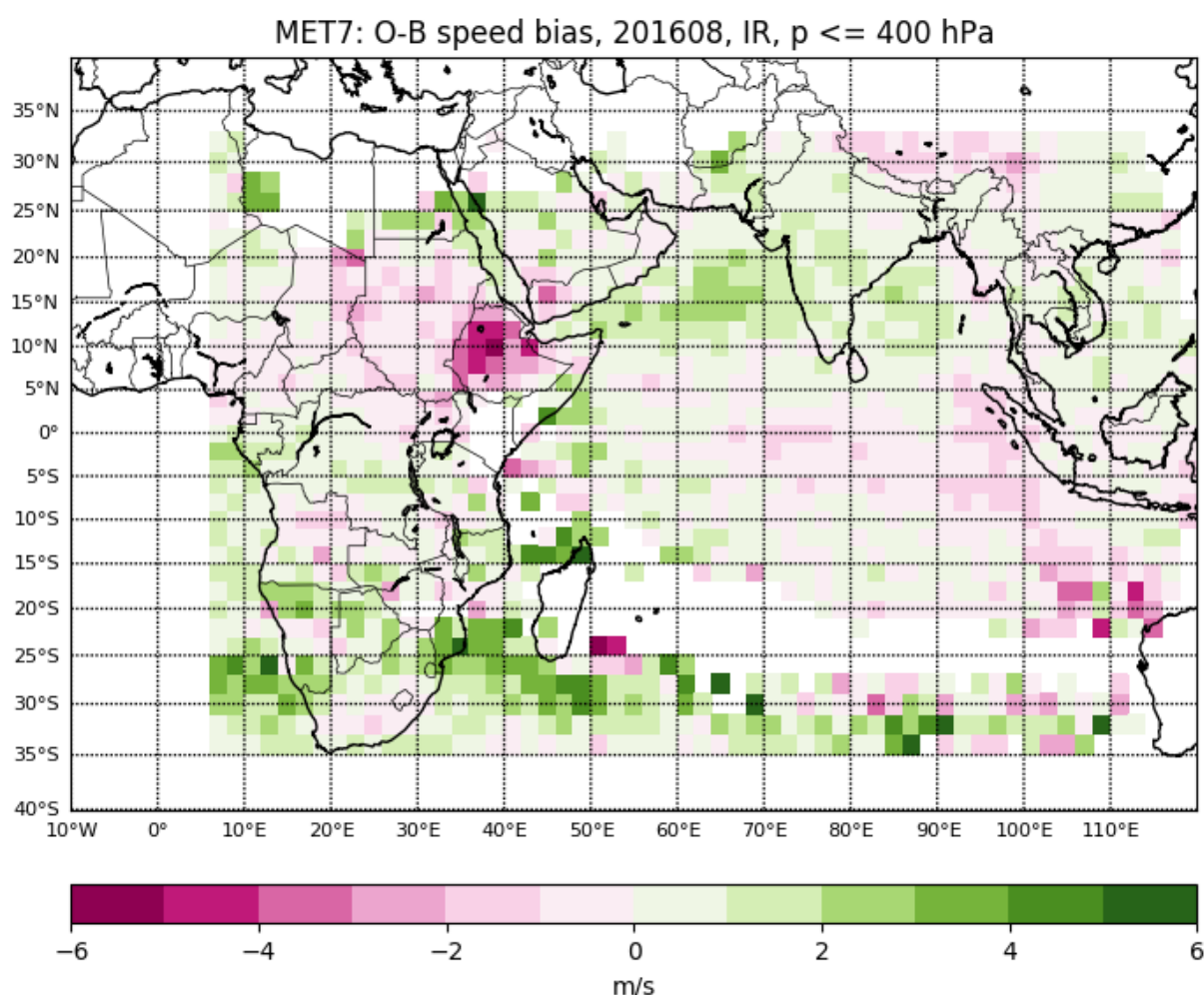




Figure 8.1 : Geographic distribution of tropical MET7 wind speeds against collocated ECMWF winds. O-B speed bias is averaged for high levels ($p \leq 400 \text{ hPa}$) and over a $2^\circ \times 2^\circ$ latitude x longitude grid. MET7 AMVs are extracted by CIMSS from Meteosat-7 IR imagery.

The strong convection over the Boiler box alters significantly the shape of clouds within ~ 50 min as indicated by the relatively weak correlation of pixels (see e.g. Figure 6.25, Figure 6.27 and Figure 6.28). The AMV extraction scheme uses the standard cross-correlation method that compares the individual


	<p align="center">Study of AMV speed biases in the tropics</p> <p align="center">Final Report</p>	
Reference: AMV-TN-0008-TS_Ed1_Rev3	Date : 18/06/2020	Page : 115/118

pixel counts of the target box with all possible location of the target box in the search area to find the best match. The best pixel-accurate target match is the target that maximizes the two-dimensional cross-correlation coefficient (Border et al., 2014). The extraction algorithm thus looks for maximum correlation between the pixels of the target box in both images but it does not take into account that the spatial correlation can actually be relatively low. A preliminary analysis of the correlation surface of two AVHRR images indicate that low correlation of pixels is frequently present (M. Carranza, personal communication). In this sense, it is recommended to derive such correlation surfaces of two AVHRR images and flag relevant AMV data if the correlation in relevant area is low. That is, AMV data should be kept but a variable makes the end users aware that the winds are computed using pixels of low correlation.

	Study of AMV speed biases in the tropics Final Report	
Reference: AMV-TN-0008-TS_Ed1_Rev3	Date : 18/06/2020	Page : 116/118

9 REFERENCES

- Borde, R., M. Doutriaux-Boucher, G. Dew, M. Carranza, 2014: A Direct Link between Feature Tracking and Height Assignment of Operational EUMETSAT Atmospheric Motion Vectors. J. Atmos. Oceanic Technol., 31, 33–46. doi: <http://dx.doi.org/10.1175/JTECH-D-13-00126.1>
- Borde, R., O. Hautecoeur, and M. Carranza, 2015: EUMETSAT Global AVHRR Wind Product. J. Atmos. Oceanic Technol., 33, 429-438. doi: <http://dx.doi.org/10.1175/JTECH-D-15-0155.1>
- Bormann, N., Salonen, K., Peubey, C., McNally, T., and Lupu, C., 2012: An overview of the status of the operational assimilation of AMVs at ECMWF. Assimilation of scatterometer winds at ECMWF, IWW11, Auckland, February 2012.
- Folger, K., and M. Weissmann, 2014: Height correction of atmospheric motion vectors using satellite lidar observations from CALIPSO. J. Appl. Meteor. Climatol., 53, 1809-1819.
- Forsythe, M., Peubey, C., Lupu, C., and Cotton, J., 2014: Assimilation of wind information from radiances: AMVs and 4D-Var tracing. ECMWF Annual Seminar, September 2014.
- Gálvez, J.M. and Davison, M., 2016: The Gálvez-Davison Index for Tropical Convection. National Oceanic and Atmospheric Administration (NOAA). 23 pp.
- García-Pereda, J., and R. Borde, 2014: The impact of the tracer size and the temporal gap between images in the extraction of atmospheric motion vectors. J. Atmos. Oceanic Technol., 31, 1761–1770, doi:10.1175/JTECH-D-13-00235.1.
- Hautecoeur, O., and R. Borde, 2017: Derivation of Wind Vectors from AVHRR/MetOp at EUMETSAT. J. Atmos. Oceanic Technol., 34, 1645–1659. doi: <http://dx.doi.org/10.1175/JTECH-D-16-0087.1>
- Hogan, 2014: Radiation Quantities in the ECMWF model and MARS. ECMWF report. Available from <https://www.ecmwf.int/file/272938/download?token=B1pe0yCl>
- Horvath, Á. and R. Davies, 2001: Feasibility and error analysis of cloud motion wind extraction from near simultaneous multiangle MISR measurements, J. Atmos. Oceanic Tech., 18, 591-608.
- Horváth, Á., O. Hautecoeur, R. Borde, H. Deneke, and S.A. Buehler, 2017: Evaluation of the EUMETSAT Global AVHRR Wind Product. J. Appl. Meteor. Climatol., 56, 2353–2376. doi: <https://doi.org/10.1175/JAMC-D-17-0059.1>
- Kealy, J. C., Marenco, F., Marsham, J. H., Garcia-Carreras, L., Francis, P. N., Cooke, M. C., and Hocking, J.: Clouds over the summertime Sahara: an evaluation of Met Office retrievals from Meteosat Second Generation using airborne remote sensing, Atmos. Chem. Phys., 17, 5789–5807, <https://doi.org/10.5194/acp-17-5789-2017>, 2017.
- Nieman, S.J., Schmetz, J. and Menzel, P.W., 1993: A comparison of Several Techniques to Assign Heights to Cloud Tracers. J. Appl. Meteor., 32, 1559–1568.
- Salonen, K., Cotton, J., Bormann, N., & Forsythe, M., 2015: Characterizing AMV Height-Assignment Error by Comparing Best-Fit Pressure Statistics from the Met Office and ECMWF Data Assimilation Systems. Journal of Applied Meteorology and Climatology, 54(1), 225-242.
- Sassen, K., and Z. Wang, 2008: Classifying clouds around the globe with the CloudSat radar: 1-year of results, Geophys. Res. Lett., 35, L04805, doi:10.1029/2007GL032591.


	<p align="center">Study of AMV speed biases in the tropics</p> <p align="center">Final Report</p>	
Reference: AMV-TN-0008-TS_Ed1_Rev3	Date : 18/06/2020	Page : 117/118

Smith, R.K., 2015: Lectures on tropical meteorology. Ludwig-Maximilians University of Munich. Available from https://www.meteo.physik.uni-muenchen.de/~roger/Lectures/TropicalMetweb/Tropical_meteorology.pdf. Last access: 29/08/2019.

Warrick, F., 2016: NWP SAF AMV monitoring: The 7th analysis report (AR7). NWP SAF Tech. Doc. NWPSAF-MO-TR-032, 35 pp.

Weissmann, M., K. Folger and H. Lange, 2013: Height correction of atmospheric motion vectors using airborne lidar observations. J. Appl. Meteor. Climatol., 52, 1868–1877.

Yang, G.Y. and J. Slingo, 2000: The Diurnal Cycle in the Tropics. Monthly Weather Review, 129, 784-801.

	<p align="center">Study of AMV speed biases in the tropics</p> <p align="center">Final Report</p>	
Reference: AMV-TN-0008-TS_Ed1_Rev3	Date : 18/06/2020	Page : 118/118

Annexe A : Comparison of AMVs from Meteosat-7, GOES-13 and -15, FYE/G to ECMWF forecast winds

The geographical distribution of monthly O-B speed biases for EUMETSAT Meteosat-7 IR imagery and Meteosat-10 WV imagery as well as for CIMSS GOES-13 IR and WV imagery, CIMSS GOES-15 IR and WV imagery, CIMSS EUMETSAT Meteosat-7 IR and WV imagery, CIMSS Meteosat-10 IR and WV imagery and FY2E and FY2G are given in document AMV-TN-0008-TS_Ed1_Rev1_Final_draft_appendix.pdf. These monthly mean wind speed differences between AMV and ECMWF forecast winds are separated for high-, mid- and low-level clouds. The method detailed in Section 4.1 is applied.